THERMAL AND STRESS ANALYSIS OF AN ATTACHED INFLATABLE DECELERATOR (AID) DEPLOYED IN THE MARS AND EARTH ATMOSPHERES

By G. L. Faurote and J. L. Burgess

Prepared under Contract NAS1-9726, Modification 2,

GOODYEAR AEROSPACE CORPORATION

Akron, Ohio

for

Langley Research Center

NATIONAL AERONAUTICS AND SPACE ADMINISTRATION

FOREWORD

Work described in this document was performed by Goodyear Aerospace Corporation, Akron, Ohio under NASA Contract NAS1-9726, Modification 2. The contractor's number for this report is GER-14939.

CONTENTS

ILLUSTRATIONS

TABLES

THERMAL AND STRESS ANALYSIS OF AN ATTACHED INFLATABLE DECELERATOR (AID) DEPLOYED IN THE MARS AND EARTH ATMOSPHERES

By G. L. Faurote and J. L. Burgess

SUMMARY

Parametric thermal and stress analysis of a 20-ft-diameter Attached Inflatable Decelerator (AID) deployed in the most severe of the postulated Mars atmospheres were conducted. An AID is a low mass, ram-air inflatable fabric canopy configured to the payload to be decelerated.

A posigrade equatorial ballistic entry was considered from an altitude of 800,000 ft, at an inertial velocity of 15,000 fps, and a flight path angle of -18 deg. AID deployment was considered over a Mach number range of 3.0 to 8.0 for ballistic entry coefficients of 0.4, 0.5, 0.6, and 0.7 slugs/ sq. ft.

Deployment of the AID was shown feasible using existing technology over the entire range of parameters considered. Furthermore, the minimum coating weight (1.0 oz/sq. yd.) needed to provide an air tight fabric structure was shown to provide thermal protection for the fabric over the entire range of entry ballistic coefficients considered for deployment Mach numbers up to 6.7.

In addition to the Mars entry study, a thermal and stress analysis of an AID deployed in the Earth atmosphere was conducted to determine a limiting state-of-the-art design point. For the Nomex fabric and range of coating weights considered during the Mars entry study, deployment in Earth atmosphere was found to be limited to a Mach number of 5.8 at a dynamic pressure of 60 psf for vehicle ballistic coefficients up to 0.6 slugs/sq. ft.

I - INTRODUCTION

Numerous analyses (e.g. Reference 1) conducted during the past several years have shown the feasibility of employing inflatable decelerators for planetary entry missions when sufficient atmosphere exists. Mars entry mission studies (see Reference 2, 3, and 4) have shown the need for efficient deceleration at supersonic and hypersonic (Mach 5+) speeds. These studies have considered the use of an Attached Inflatable Decelerator (AID) for accomplishing the needed deceleration.

To date mission studies considering the use of an AID for Mars entry application have imposed deployment Mach number constraints to insure acceptable decelerator fabric temperatures. Thus, these studies have not been performance limited, rather they have been limited by the undetermined effects of entry heating on the AID structure. Accordingly, the primary purpose of the current investigation was to examine, in detail, the combined effects of entry heating and pressure loading on the AID operating over a rather wide range of parameters of current and future interest.

Recognizing, that prior to the application of an AID in a planetary entry mission its performance under closely simulated mission conditions must be demonstrated, an analysis was undertaken to establish a limiting state-of-the-art design point in the earth atmosphere.

SYMBOLS

A	total projected area of AID, surface area
B	ballistic parameter
c	specific heat of material
c_p	specific heat of gas
C_D	drag coefficient based on total projected area
$(C_DA)_D$	deployed drag area
$(C_DA)_E$	entry drag area
C_1, C_2	constants for Sutherland's viscosity equations
d_f	unit mass of fabric
d_m	unit mass of meridian
D_o	nominal diameter
E_θ	circumferential unit elongation
E_ϕ	meridional unit elongation
$\bar{f}$	nondimensional fabric stress resultant
f_s	stress in meridional thread set

F(s)	shape factor for laminar boundary layer
F(o)	stagnation point shape factor
g_o	gravitational constant
Gr	Grashof number
G(s)	shape factor for turbulent boundary layer
h	enthalpy
h_{c_i}	internal surface heat transfer coefficient
h_{c_o}	external surface heat transfer coefficient
H	total enthalpy
J	Joules constant
k	thermal conductivity
k_c	strength-weight ratio of fabric
k_f	strength-weight ratio of meridians
K_c	construction factor
K_D	design factor
l_m	length of a meridian
l_t	tow line length
L	length
m	molecular weight
M	Mach number
M_D	deployment Mach number
n	number of meridians
Nu	Nusselt number

N_θ	principal circumferential membrane stress
N_ϕ	principal meridional membrane stress
p	$p_i - p_b$, pressure
p_e	local surface static pressure
Pr	Prandtl number
q	dynamic pressure
$\dot{q}$	heat flux rate
Q	heat energy
r	radius of cross section of body
r_e	recovery factor
R	gas constant, maximum radius of AID, radius
R'	radius of AID (excluding fence)
R_n	nose radius
Re_s	local length Reynolds number
$Re_{s_{tr}}$	transition Reynolds number based on length
s	distance along surface from stagnation point
s_{tr}	distance along surface to boundary layer transition measured from stagnation point
T	temperature
$\bar{T}$	nondimensional meridian cord load
T_m	meridian cord load
u	velocity
w	weight
X	thickness of material
x	radial coordinate to AID surface, distance from aeroshell apex
y	distance measured normal to surface
z	altitude

β	bias angle, coefficient of thermal expansion
γ	ratio of specific heats, flight path angle
Δ	incremental time or distance, differential
η	ratio of burble fence diameter to canopy diameter
μ	viscosity
ξ	ratio of aeroshell radius to total decelerator radius
ρ	density
f	stress in one thread
ω	μ/RT
τ	time
ν	μ/ρ

Subscripts

a	aeroshell base
aw	adiabatic wall
b	burble fence
c	coating
e	edge of boundary layer
E	entry
f	forward surface of AID
i	inside wall, internal
L	laminar boundary layer
o	stagnation point
r	rear surface of AID
s	structural weight, local value
T	turbulent boundary layer, total
t	total conditions
w	wall or surface
∞	free stream

II - STUDY BACKGROUND

In establishing the feasibility of employing inflatable decelerators for planetary entry missions, studies such as Reference 1 have also shown that a system utilizing drag augmentation at supersonic speeds in conjunction with a terminal descent propulsion system is the most efficient and effective means of effecting soft landings on the planetary surface. Such a system (see Reference 6) is currently under development for the 1975 Viking Mars Lander mission. The operational mode to be used for the 1975 Viking Mars Lander decelerator system is mortar ejection of a 53 foot nominal diameter disk-gap-band parachute following lifting entry. Current plans call for mortar ejection at a maximum Mach number of 2.2 and a dynamic pressure of 10.5 psf. The parachute drag decelerates the lander to conditions suitable for terminal descent engine ignition for final descent and landing.

Recent studies of advanced (beyond Viking) planetary-missions (see References 2 and 3) concerning entry into the low density atmosphere of Mars, have shown the need for efficient deceleration at supersonic and hypersonic (Mach 5+) speeds. These studies considered the use of an AID, for accomplishing the desired supersonic deceleration, as either the initial stage of a two-stage decelerator system or as a single stage device in conjunction with a terminal descent propulsion system. The AID, which is constructed by overlaying a coated fabric with many load carrying meridional tapes (See Figure 1), is basically a uniform-stress (isotensoid) structure as described in Reference 7. The canopy shape is maintained by pressure recovered from ram-air (atmosphere) inlets aligned with the local airflow. Coating is required to reduce the basic fabric permeability to the extent that the pressure recovered by the ram-air inlets can maintain the isotensoid shape. Additional coating can be applied to provide thermal protection to the basic fabric structure. For subsonic speeds, a burble fence, located at the maximum canopy diameter, is necessary to provide stable operation.

Reference 2, which considers the AID as an initial stage of a two stage decelerator system, indicates that, as a result of the efficient supersonic deceleration characteristics of the AID, significant increases in landed payload mass (see Figure 2) can be realized without increasing the size of the basic entry aeroshell. Additionally, Reference 2 shows that the AID will relax stringent deployment conditions on the terminal stage decelerator.

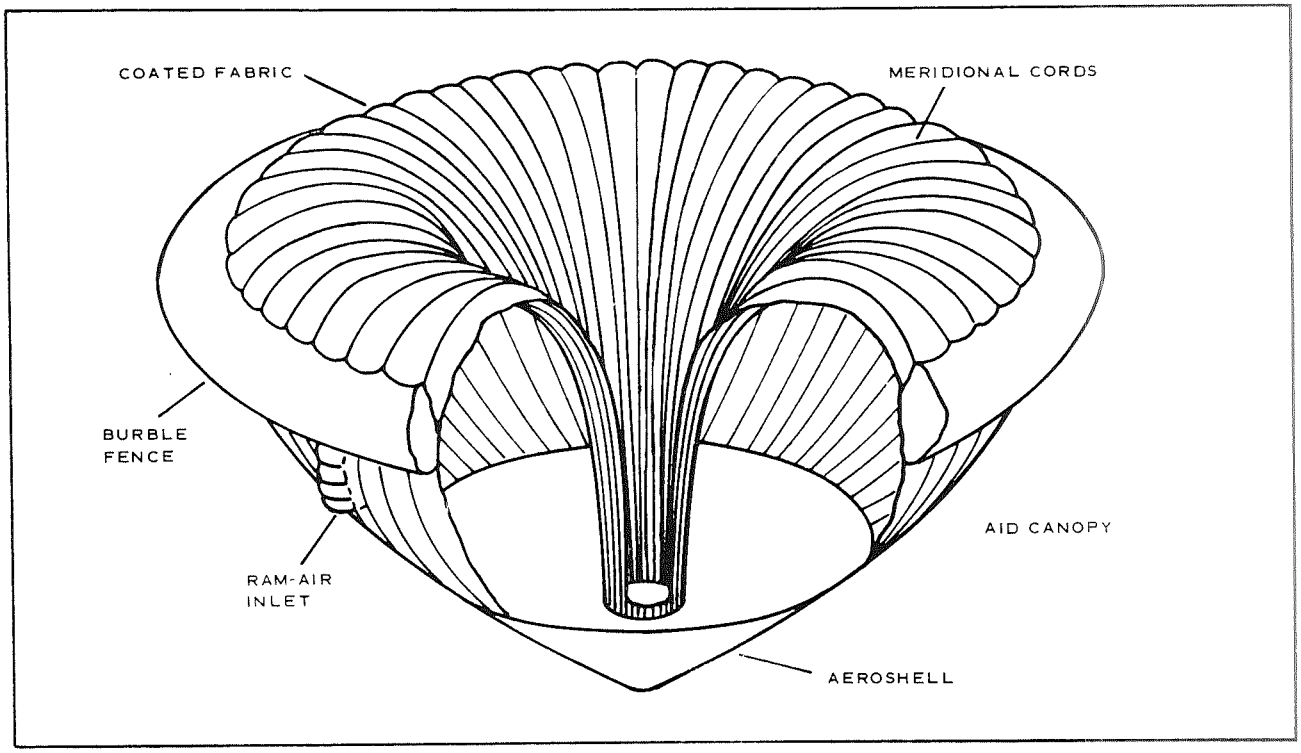

Figure 1 - Cutaway Drawing of an AID

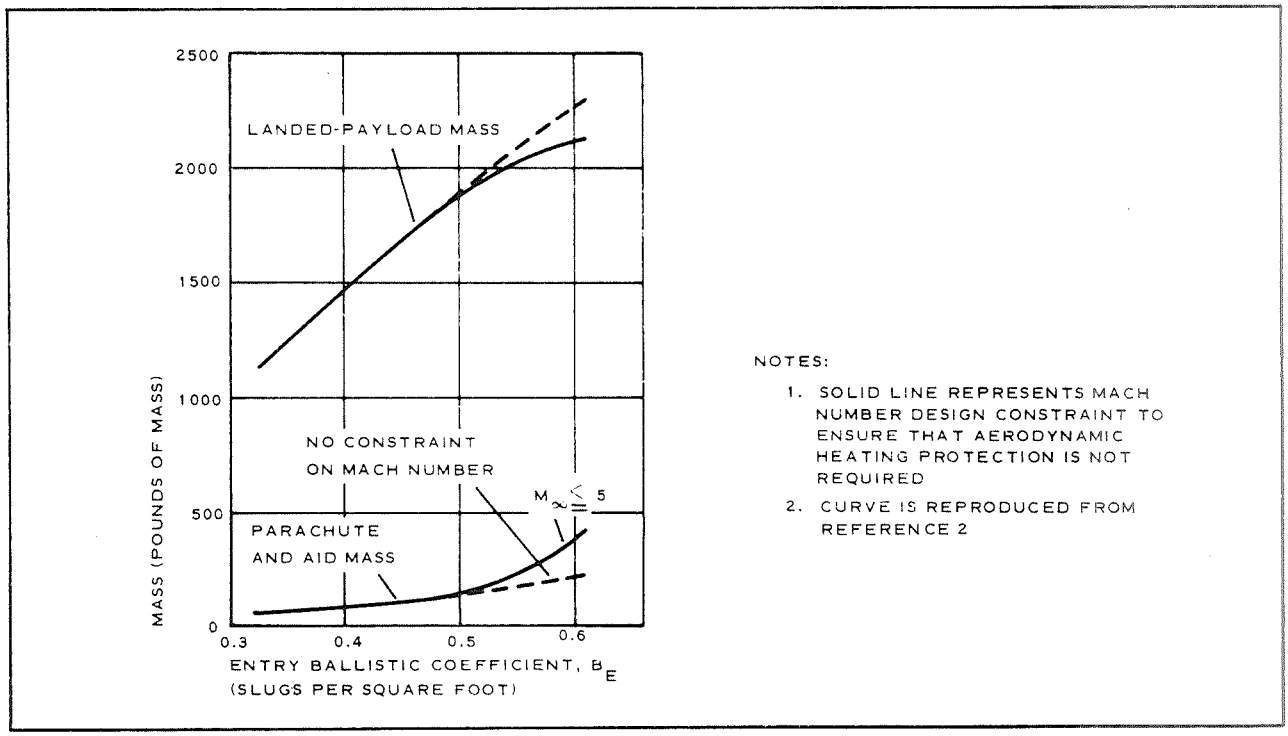

Figure 2. - Variations in Decelerator Mass and Landed-Payload Mass with Ballistic Coefficient

Basically, the two-stage approach takes advantage of the high supersonic drag of the AID and the high subsonic and transonic drag of a terminal stage parachute such as the disk-gap-band (see Figure 3). Conditions chosen in Reference 2 for staging from AID operation to the terminal stage parachute operation were M = 1.5 at an altitude of 12,000 ft. It should be noted that these staging conditions yield a low dynamic pressure and as a result the parachute will nearly always be fabricated of minimum gage materials.

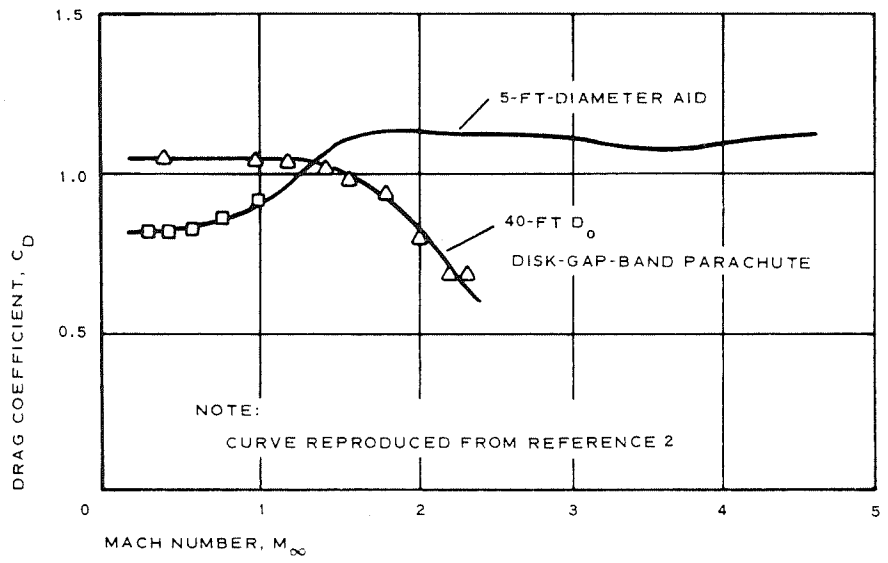

Figure 3 - Drag Performance of AID and Disk-Gap-Band Parachute

III - PARAMETRIC ANALYSIS

The range of parameters investigated during the parametric thermal and stress study (see Table I) are essentially those considered in the Mars mission application study of Reference 2. The AID was considered to be the initial stage of a two-stage decelerator system with similar staging conditions (i.e., M = 1.5 at 12,000 ft. altitude).

TABLE I - Range of Study Parameters

Condition	Parameter	Range
Entry	B_E	$0.3 \leq B_E \leq 0.7$ slugs/sq. ft.
	h_E	800,000 ft.
	Z_E	15,000 fps
	γ_E	-18 deg
AID Deployed*	M_D	$3.0 \leq M_D \leq 8.0$

*$(C_DA)_D/(C_DA)_E = 4.5$

An AID configuration, with a deployed drag area to entry drag area ratio of 4.5, was considered during the current investigation because the majority of performance data generated to date have been for this configuration (see References 2 and 8 through 14). A detailed description of the configuration is given in the thermal analysis discussion.

The overall analytical approach used during the study is presented in Figure 4. As indicated in Figure 4, the parametric study was initiated by computing entry trajectories for a series of vehicle ballistic coefficients. From each entry trajectory, AID deployed trajectories were computed for a range of deployment Mach numbers. Boundary layer and internal heat transfer relations were developed and evaluated for each of the AID deployed trajectories.

The resulting heat transfer rates were combined with a one dimensional transient heat conduction analysis to yield AID temperatures for each deployed trajectory. A stress analysis was also conducted during which relations were developed expressing the AID weight as a function of dynamic pressure and the AID temperature. The parametric analysis was concluded by calculating AID weights for each deployment case considered.

In view of the extent and complexity of the analysis undertaken, a digital computer solution was developed to determine the AID time - dependent temperature profiles. This program coupled the following for simultaneous solution:

Deployed AID equations of motion
Boundary layer heat transfer equations
One-dimensional heat conduction equations

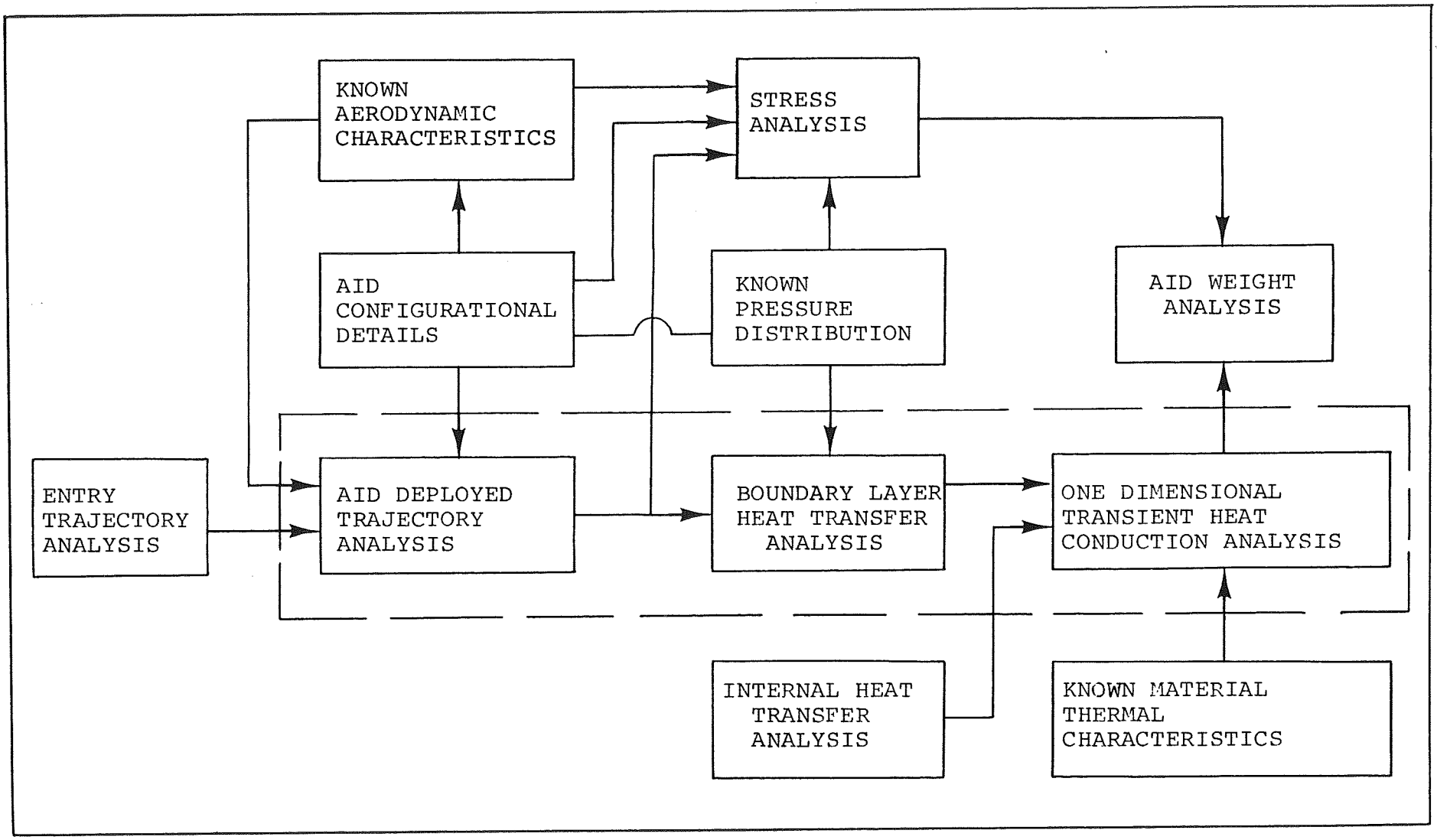

Figure 4 - Analytical Approach to Parametric Study

This time dependent program is encompassed by dashed lines in Figure 4.

A similar analytical approach to that outlined in Figure 4, for the parametric study, was used in the design point analysis of the AID operating in the Earth atmosphere.

Trajectory Analysis

Entry Trajectories - A posigrade equatorial entry of the vehicle along a ballistic trajectory was considered from an altitude of 800,000 ft. at an inertial velocity of 15,000 fps and a flight path angle of -18 deg. Entry trajectories were established (see Figure 5), in the 1970 Mars min $H_{\rho,s}$ atmosphere, for the ballistic coefficients presented in Table I. The detailed properties of the atmosphere used are presented in Appendix A of this report. Of the five currently postulated Martian atmospheres, the min $H_{\rho,s}$ imposes the maximum Mach number and dynamic pressure conditions which lead to maximum aerodynamic heating and pressure loading.

Aid Trajectories - AID deployment conditions for each entry trajectory of Figure 5 were determined (see Figure 6) that resulted in the AID altering the entry trajectory for $(C_DA)_D/(C_DA)_E = 4.5$, to the decelerator staging conditions. These trajectories passing through the staging conditions are hereafter referred to as "nominal" trajectories. A nominal trajectory is not presented for $B_E = 0.3$ because the entry vehicle alone essentially achieves the condition of M = 1.5 at 12,000 ft. altitude. Figure 7 presents a summary plot of entry ballistic coefficient versus deployment Mach number and dynamic pressure, for $(C_DA)_D/(C_DA)_E = 4.5$, that yield trajectories passing through the decelerator staging conditions.

In addition to establishing the "nominal" trajectories, AID deployed trajectories (See Figures 8 through 12) were initiated at Mach numbers 3, 5, and 8 from each entry trajectory, except where such a starting point yielded a trajectory resulting in M = 1.5 at an altitude below 12,000 ft. The appropriate "nominal" trajectories have also been included in Figure 8 through 12.

The individual AID deployment conditions considered in the parametric study are summarized in Table II.

Thermal Analysis

Thermal and Flow Model - Figure 13 presents the thermal and flow model defining the heat transfer modes and flow regimes considered subsequently in the development of the heat transfer relations. From Figure 13 it is noted that both external and internal heating were considered in arriving at the fabric temperature. Boundary layer heat transfer equations were developed to define the external heating. A heat transfer relation was developed to describe the

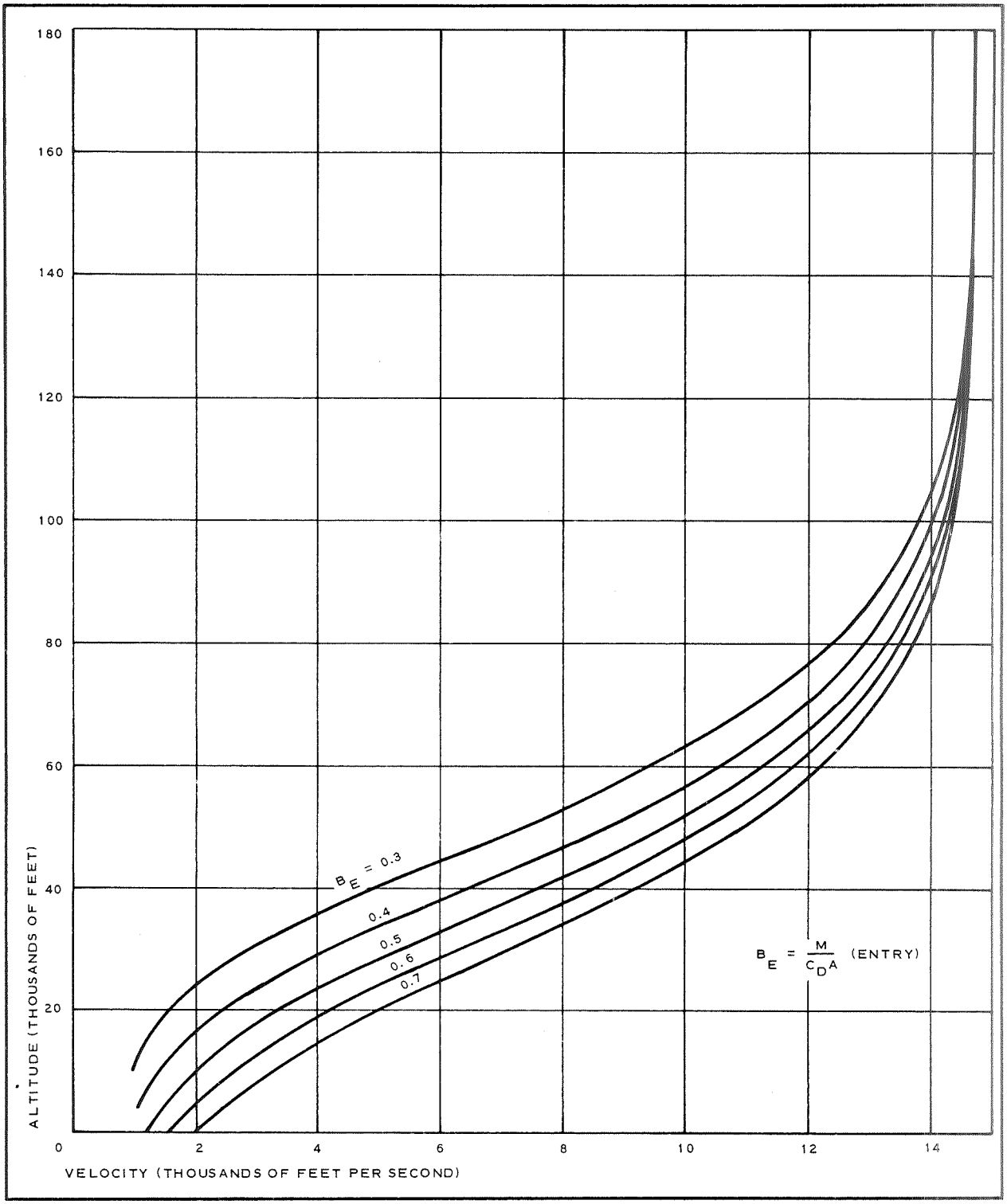

Figure 5 - Entry Trajectories - Mars Atmospheres

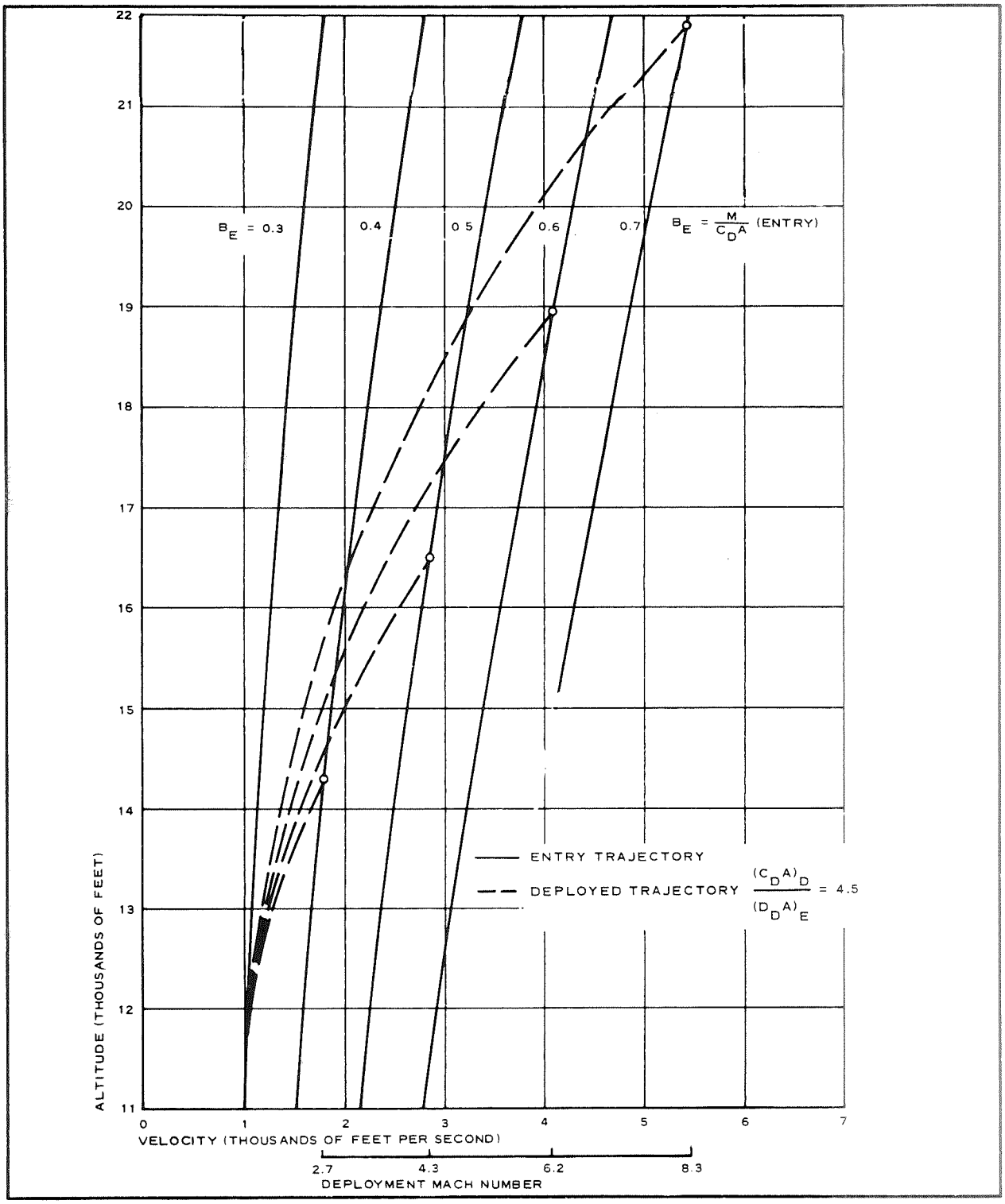

Figure 6 - Deployed AID Nominal Trajectories - Mars Atmospheres

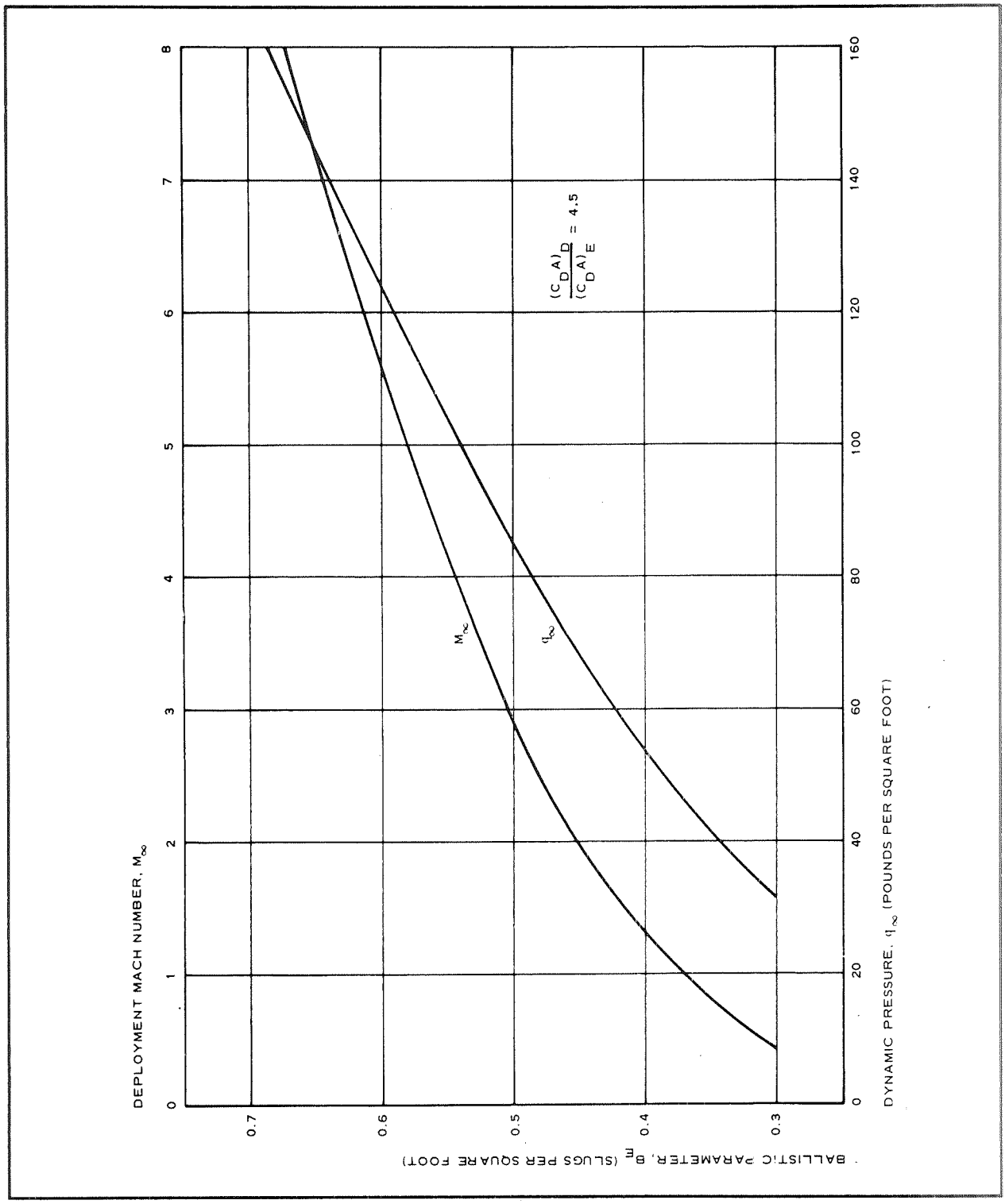

Figure 7 - AID Deployment Mach Number and Dynamic Pressure Required to Attain 12,000 ft. Attitude at M = 1.5 - Mars Atmosphere

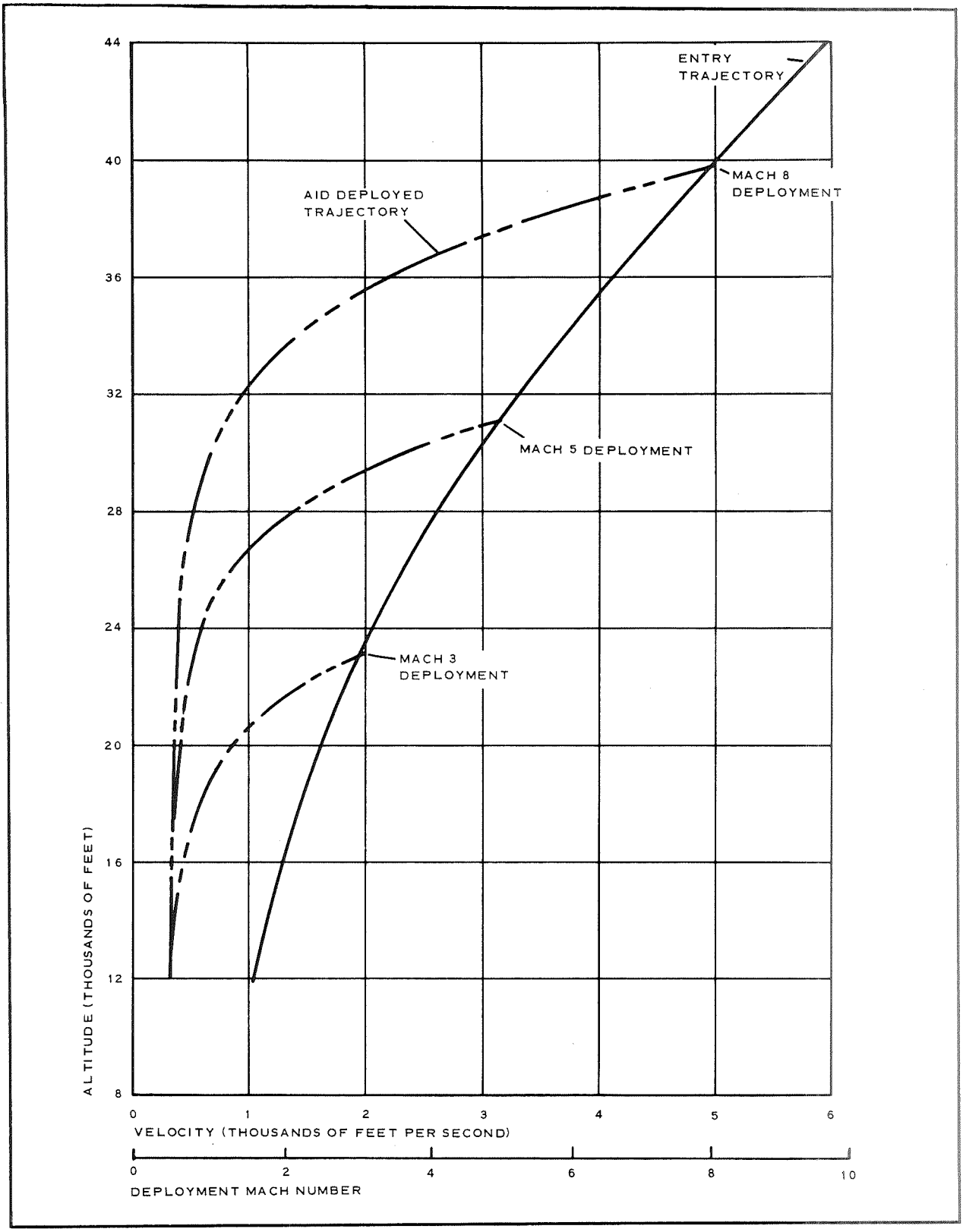

Figure 8 - Deployed AID Trajectories (B_E = 0.3)

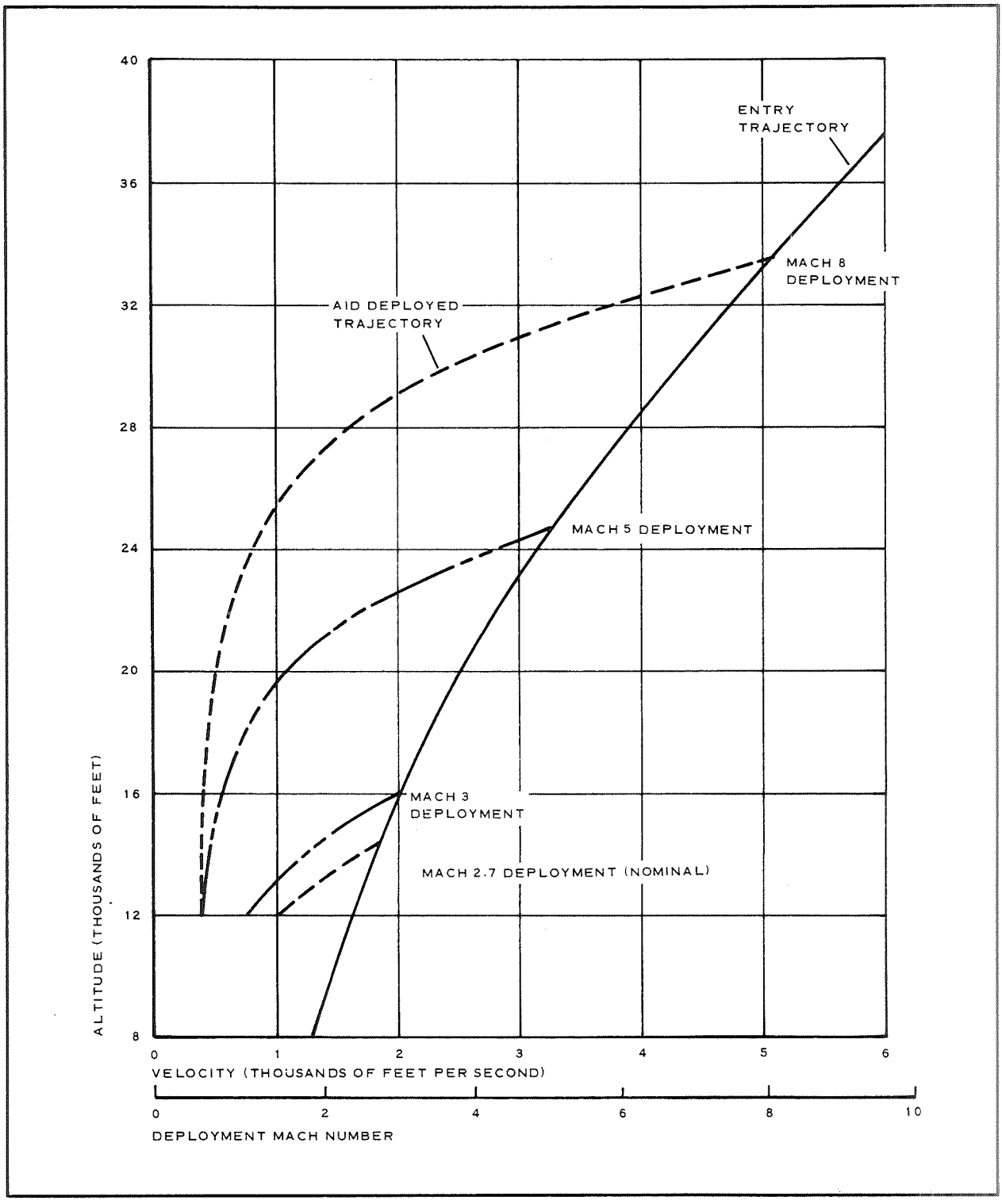

Figure 9 - Deployed AID Trajectories ($B_E = 0.4$)

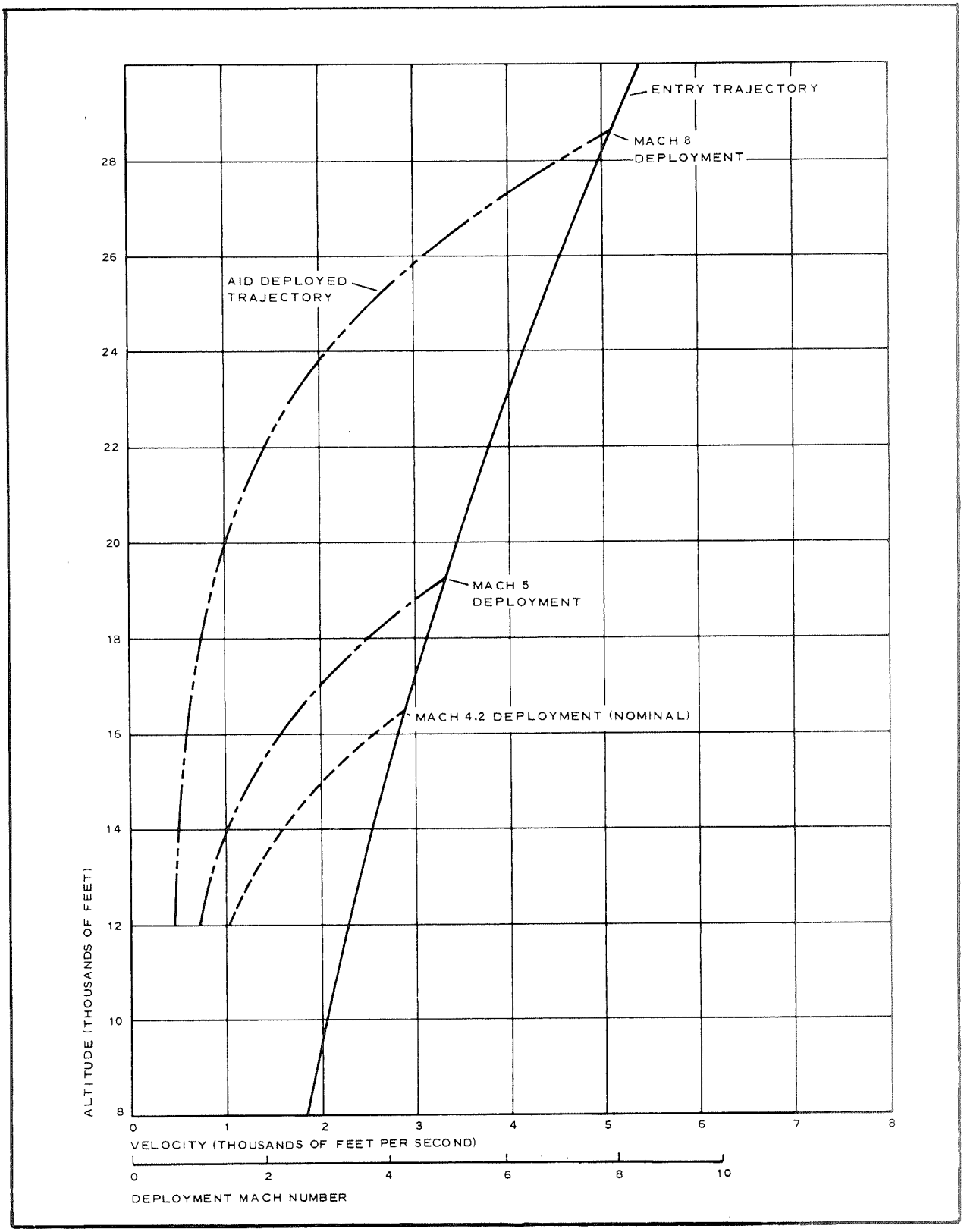

Figure 10 - Deployed AID Trajectories (B_E = 0.5)

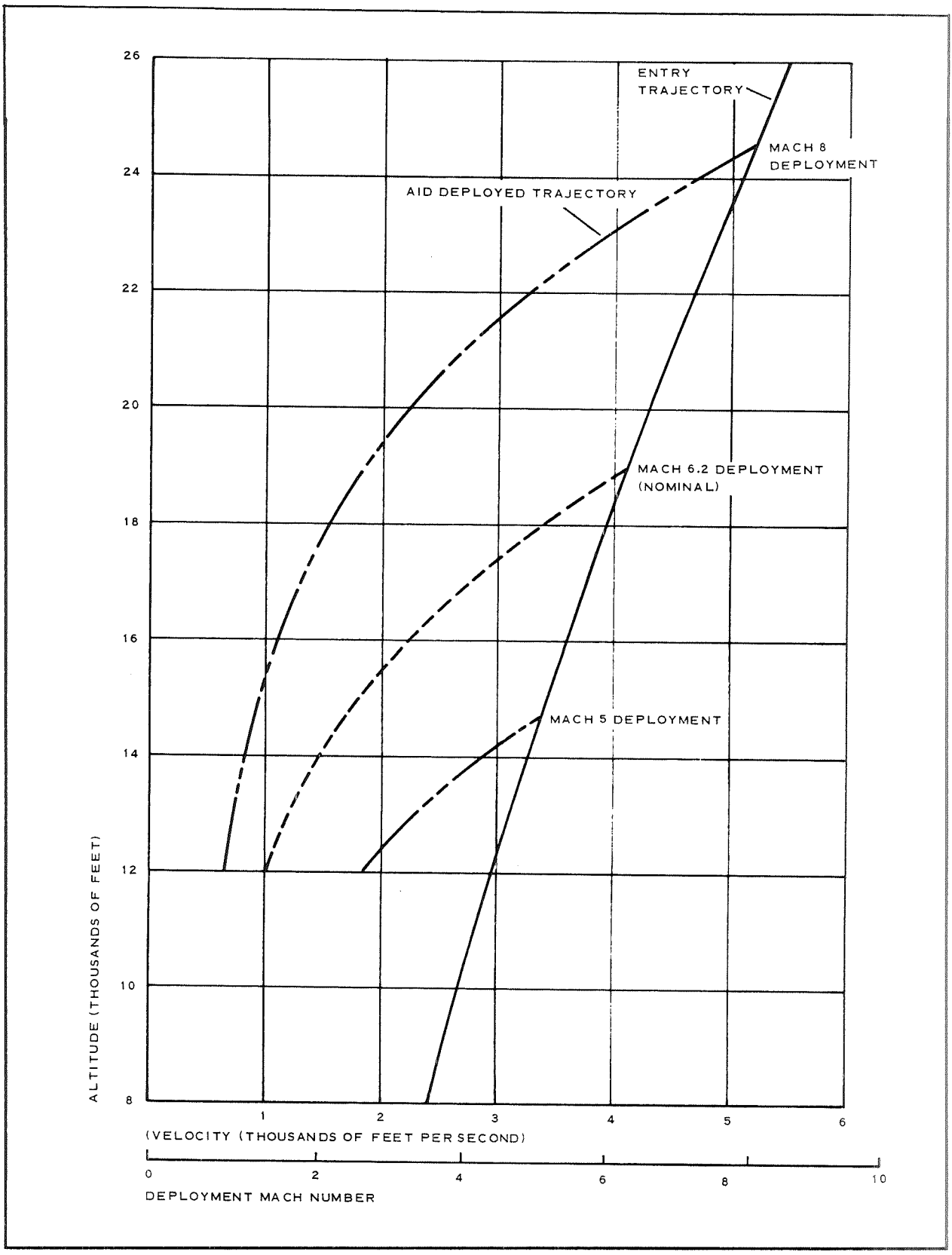

Figure 11- Deployed AID Trajectories (B_E = 0.6)

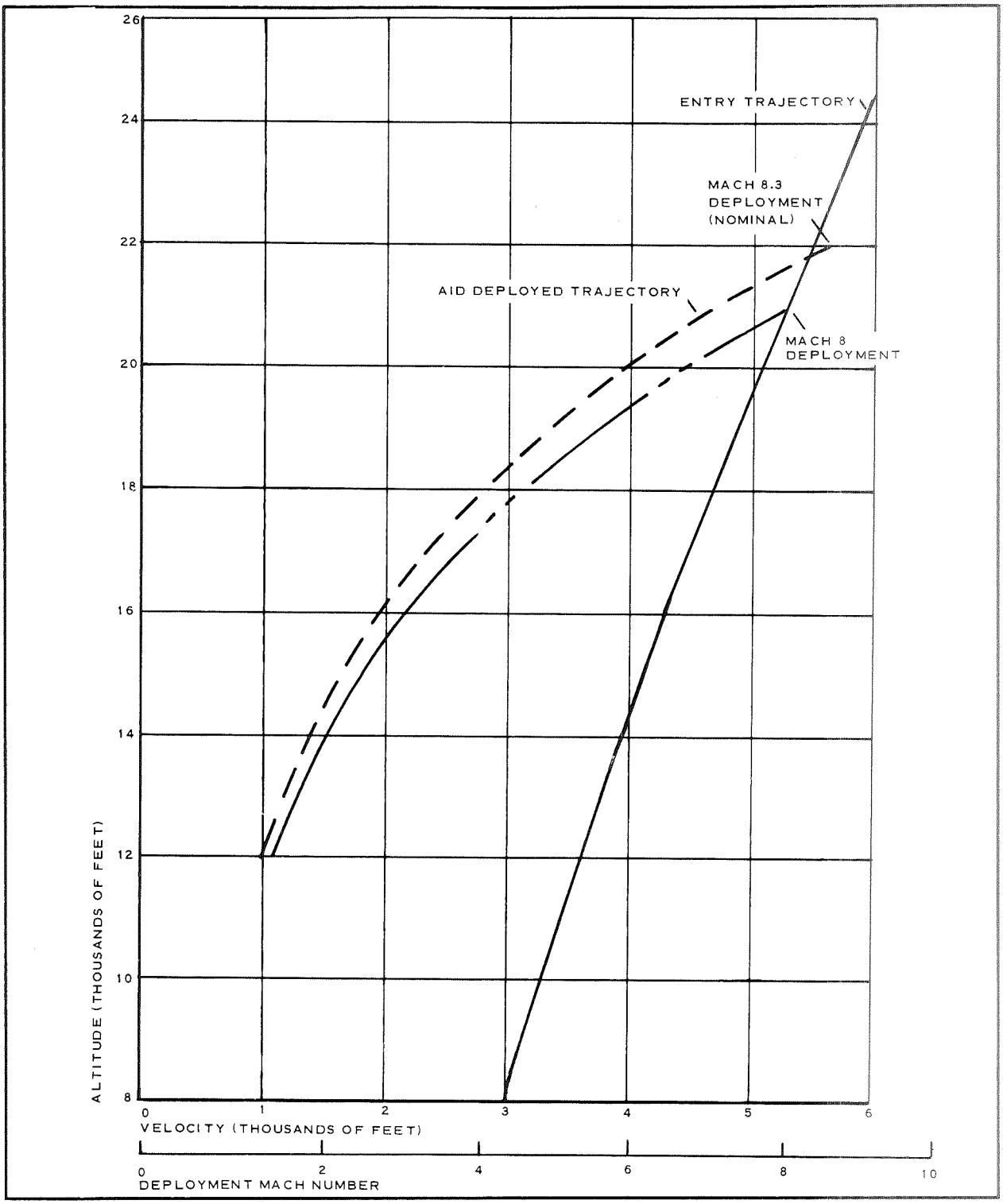

Figure 12 - Deployed AID Trajectories (B_E = 0.7)

TABLE II - AID DEPLOYMENT POINTS IN MARS ATMOSPHERE

Ballistic Coefficient B_E (slugs/ sq. ft.)	Mach Number, M_D	Altitude, Z (ft)	Dynamic pressure, q_∞ (psf)	Vehicle Velocity, V_∞ (fps)
0.3*	1.5	12,000	9.0	1000
0.3	3.0	23,100	22.3	1950
0.3	5.0	31,100	45.3	3150
0.3	8.0	39,700	80.3	4950
0.4*	2.7	14,200	25.6	1850
0.4	3.0	16,000	29.3	2000
0.4	5.0	24,700	58.9	3300
0.4	8.0	34,500	105.2	5070
0.5	3.0	. . .	. . .	. . .
0.5*	4.3	16,500	58.7	2870
0.5	5.0	19,200	72.1	3300
0.5	8.0	28,600	128.5	5100
0.6	3.0	. . .	. . .	. . .
0.6	5.0	14,700	85.4	3350
0.6*	6.2	19,000	111.6	4100
0.6	8.0	24,500	151.4	5200
0.7	3.0	. . .	. . .	. . .
0.7	5.0	. . .	. . .	. . .
0.7	8.0	21,000	172.9	5250
0.7*	8.3	21,800	180.2	5450

*Nominal Deployment

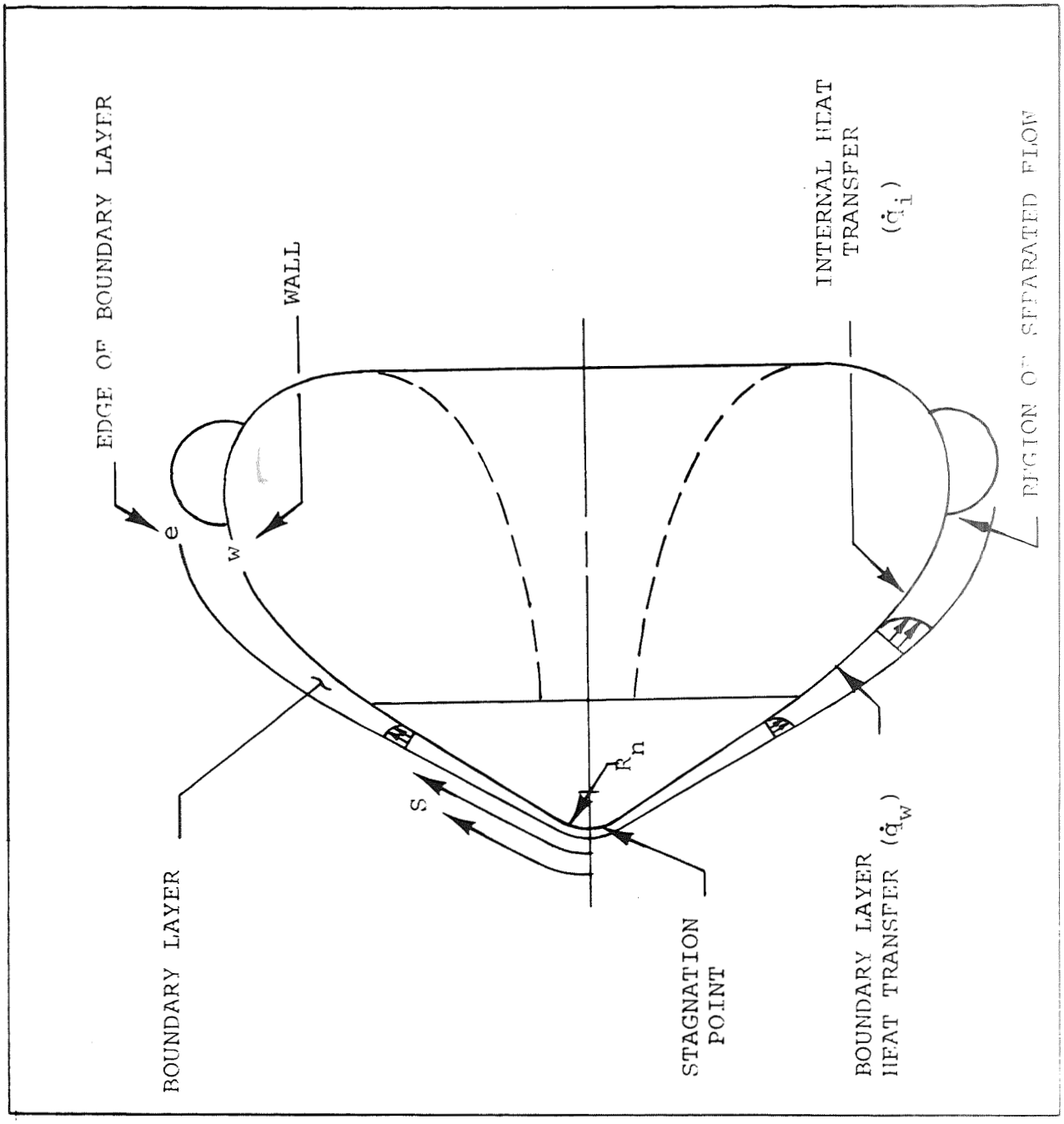

Figure 13 - Thermal and Viscous Flow Model

internal heating which results from the atmosphere entering the canopy and coming to rest at a temperature approaching the total temperature of the stream. The heat flux rates were then combined with the fabric thermal characteristics to define the resulting canopy temperatures.

The vehicle-AID profile selected for the current analysis, which was initially developed in Reference 14, is presented in Figure 14.

As shown in Figure 14, three stations were selected for the thermal evaluation, thus permitting a temperature profile to be constructed over the AID surface forward of the burble fence. Station S_1 was selected just aft of the vehicle-AID interface. Station S_3 was located just forward of the intersection of a line, tangent to both the canopy and the burble fence, with the canopy as shown in Figure 14. This point was selected on the basis of avoiding the region of separated flow in the proximity of the burble fence. Experimental data presented in Reference 12 verify that S_3 is just forward of the separated region. Station S_2 is the midpoint of S_1 and S_3.

As will be shown subsequently, the pressures over the rear surface of the AID are much reduced compared to those of the forward surface and as a result the heat transfer rates and resulting temperature levels are expected to be insignificant. Thus, coating on the rear surface, other than that required to reduce the fabric permeability to an acceptable level, will not be required.

Several combinations of fabric and coating were considered for protecting the forward surface from entry heating effects. The basic fabric selected for evaluation was a 2.3 oz/sq.yd. Nomex fabric designated as HT-189-47. While, lighter weight Nomex fabrics have been woven previously, HT-189-47 is the lightest Nomex fabric currently available. Nomex was selected over the more common decelerator materials, such as nylon and dacron, because of its increased temperature capabilities. Nomex also was the material considered for the meridians. Nomex retains half of its room temperature strength at 500F and has essentially zero strength at 750F.

A Viton fluoroelastmer coating was selected for consideration because it has a proven history (see Reference 15 and 16) of high temperature application as a decelerator coating. Viton retains its room temperature characteristics at a soak condition of 500F. It can provide thermal protection for short periods at significantly higher temperatures.

The Viton-Nomex combination has been extensively evaluated in both flight and wind tunnel tests. Trailing Ballutes fabricated of this combination have been successfully tested up to a Mach number of 4.2 (see References 15 and 16). Temperature predictions for these tests were in the range of 500 to 600F.

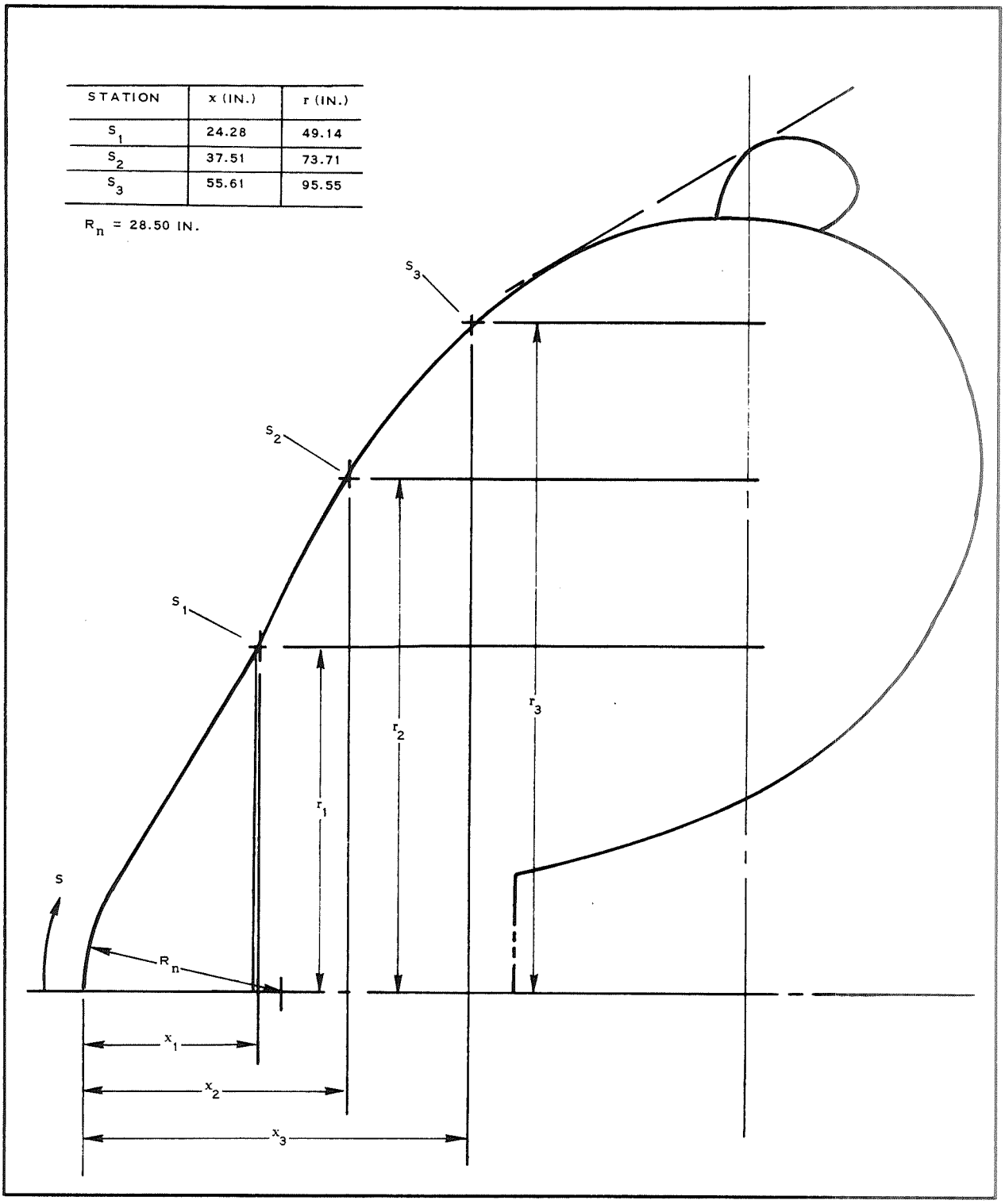

Figure 14 - Coordinates of Canopy Station Selected for Analysis

As will be shown subsequently, for the lower values of B_E and M_D of Table II, which result in minimal heat transfer rates, only the coating required to reduce the fabric permeability is needed to maintain acceptable temperature levels. The amount of coating regarded as being needed to reduce the fabric permeability was 1/2 oz sq. yd. applied to each surface of the fabric. This is the approximate quanity applied to 5.0 foot diameter Nomex models evaluated supersonically in the wind tunnel (see Reference 14).

As the value of M_D is increased, additional amounts of coating must be applied to the 2.3 oz/sq. yd. Nomex to maintain its temperature at an acceptable level. Therefore three coating weights, 1.0, 3.0, and 6.0 oz/sq. yd., were considered during the investigation. Additionally, the effect of doubling the cloth thickness was examined.

Heat transfer rates to the ram-air inlets and burble fence were not examined during this analysis in view of the complex flow existing around them. Prior to defining, with any degree of accuracy, the anticipated heat transfer to these components additional experimental data is needed.

While it is recognized that the ram-air inlets and burble fence are potential hot spots, their protection does not offer a significant problem. For instance, the ram-air inlets can conveniently be fabricated of stainless steel fabric. The use of metal fabric in decelerator construction, although it is not a common practice, has been successfully demonstrated (see Reference 17). For instance, entire Ballute assemblies have been fabricated of Rene 41 metal fabric (See Appendix B for description of a Ballute decelerator). Protection of the burble fence of the AID can be accomplished by increasing the coating thickness on the forward surface of the fence. It is not expected that such steps would significantly increase the AID weight.

Laminar and Turbulent Heat Flux Equations - The analysis of entry heating has included both laminar and turbulent heat transfer and a suitable boundary layer transition criteria. For the case of laminar heat transfer, similar solutions to the laminar boundary layer equations have been used together with the local similarity concept. For a favorable pressure gradient boundary layer, predictions based on this approach have been shown experimentally to, if anything, over-predict the heating.

It should be noted that the validity of the local similarity approach was originally based on the limiting cold wall case. However, even for moderate cooling cases, e.g. $h_w/h_{aw} \approx 0.5$, examination of similar solutions indicates that local similarity is still a good approximation.

The main advantage of this approach is the ease with which pressure gradient and body shape effects can be accounted for.

Lees (Reference 18) was the first to discuss the use of the local similarity concept in the calculation of hypersonic laminar heat transfer, and he included in his considerations both the conductive and diffusive modes of energy transfer. However, for the present applications where Mach numbers are less than 10, no such chemistry-related effects are important, and the heat flux rate for a laminar boundary layer over an axi-symmetric configuration is given by

$$\left(\dot{q}_w\right)_L = \frac{k_w}{\mu_w c_{p_w}} \frac{\rho_w \mu_w u_e r \left(0.5\ Pr^{1/3}\right)\left(H_{aw}-H_w\right)}{\left(\int_o^s \rho_w \mu_w u_e r^2 ds\right)^{1/2} \sqrt{2}} \quad , \tag{1}$$

Here the effects of $Pr \neq 1$ have been included both in the $Pr^{1/3}$ scaling of the wall temperature gradient as well as in the use of the adiabatic wall enthalpy, H_{aw}. For a perfect gas,

$$H_{aw} = c_p T_e + r \frac{u_e^2}{2} \quad , \tag{2}$$

where r_e is the recovery factor and may be taken as $\sqrt{Pr}$. Equation 1 can be modified to the form

$$\left(\dot{q}_w\right)_L = 0.5 \frac{\sqrt{(\rho_e \mu_e)_o\, u_\infty}}{(Pr)^{2/3} (R_n)^{1/2}} F(s) \left(H_{aw}-h_w\right) , \tag{3}$$

where

$$F(s) = \frac{\frac{1}{\sqrt{2}} \left(\frac{p_e}{p_o}\right)\left(\frac{\omega_e}{\omega_{e_o}}\right)\left(\frac{u_e}{u_\infty}\right) \frac{r}{R_n}}{\left[\int_o^s \left(\frac{p_e}{p_o}\right)\left(\frac{u_e}{u_\infty}\right)\left(\frac{\omega_e}{\omega_{e_o}}\right)\left(\frac{r}{R_n}\right)^2 d\left(\frac{S}{R_n}\right)\right]^{1/2}} \tag{4}$$

Furthermore, at the forward stagnation point, Equation 3 becomes

$$\left(\dot{q}_{w_o}\right)_L = 0.5 \frac{\sqrt{(\rho_e \mu_e)_o\, u_\infty}}{(Pr)^{2/3} (R_n)^{1/2}} F(o) \left(H_{a\omega}-h_w\right) , \tag{5}$$

Where

where

$$F(o) = \sqrt{2}\left[\frac{d\left(\frac{u_e}{u_\infty}\right)}{d\left(\frac{s}{R_n}\right)}\right]^{1/2} \qquad (6)$$

and for a Newtonian pressure distribution

$$\left(\frac{d_{u_e}}{ds}\right)_{s=0} = \frac{1}{R_n}\sqrt{\frac{2\,(p_b - p_\infty)}{\rho_o}} \quad . \qquad (7)$$

In calculating turbulent boundary layer heat transfer as part of the present analysis, the method of Rose, Probstein, and Adams (Reference 19) has been used. This method has the advantage of including pressure gradient effects through the use of a generalized form factor, G(s), which is similar to laminar boundary layer parameter, F(s). This method conveniently accounts for the effect of body shape in turbulent heating calculations, just as the local similarity approach in the laminar boundary layer case.

For turbulent boundary layers, the surface heat transfer rate may be expressed using the equation

$$(\dot{q}_w)_T = \frac{Nu_s}{Re_s Pr}\,\rho_e u_e\,(H_{aw} - h_w) \quad , \qquad (8)$$

where H_{aw} is as in Equation 2, but with the recovery factor r_e given by $\sqrt[3]{Pr}$. Following Rose, Probstein, and Adams, Nu_s may be expressed in the form

$$Nu_s = 0.029(Re_s)^{0.8}\,Pr^{1/3}\,G(s) \quad , \qquad (9)$$

where G(s) is the generalized form factor for turbulent boundary layers. Thus

$$(\dot{q}_w)_T = 0.029(Re_s)^{-0.2}\,Pr^{-2/3}\,\rho_e u_e\,G(s)\,(H_{aw} - h_w) \quad . \qquad (10)$$

Using the momentum integral equation, a 1/7th power-law velocity profile, and assuming the Blasius turbulent flow result relating skin friction and boundary layer thickness to be correct, Rose, Probstein, and Adams arrived at the following expression for G(s) for an axisymmetric body:

$$G(s) = \left[\frac{\int_{s_{tr}}^{s} \left(\frac{\rho_e}{\rho_o}\right)\left(\frac{\mu_e}{\mu_o}\right)^{1/4}\left(\frac{u_e}{u_\infty}\right)^{9/4}\left(\frac{r}{R_n}\right)^{5/4} d\left(\frac{s}{R_n}\right)}{1.2\left(\frac{\rho_e}{\rho_o}\right)\left(\frac{\mu_e}{\mu_o}\right)^{1/4}\left(\frac{u_e}{u_\infty}\right)^{9/4}\left(\frac{r}{R_n}\right)^{5/4}\left(\frac{s}{R_n}\right)} \right]^{-1/5} \quad . \qquad (11)$$

Here s_{tr} is the value of s at the transition point. For the case where the vehicle boundary layer is turbulent everywhere, then $s_{tr} = 0$.

It should be noted that for a hemispherical cylinder body in a high-speed flow, then as $s \to \infty$, $dp/ds \to 0$, $G(s) \approx 1$, and Equation 10 takes on the form appropriate for a flat plate. Furthermore for a turbulent boundary layer in the nose region of such a body, G(s) is not a maximum at the stagnation point, as F(s) would be for laminar flow, but peaks in the neighborhood of about 30 deg from the stagnation point.

Boundary Layer Transition Criteria - The determination of whether laminar or turbulent heating exists at a location on the vehicle surfaces is prescribed by the use of a local length Reynolds number. For this study, a Reynolds number of 200,000 was used to define the point of transition to turbulent heating conditions. Thus, if

$$Re_s = \frac{\rho_e u_e s}{\mu_e} \leqq 200,000 \quad , \qquad (12)$$

Equation 3 is used to calculate the heat transfer rate. Once the Reynolds number exceeds a value of 200,000 at a location on the surface, Equation 10 is used to calculate the heat transfer rate to the surface. Selection of this somewhat conservative transition Reynolds number provides assurance the fabric and coating investigated will perform at least as well as predicted.

Internal Heating Considerations - The AID is inflated by ram-air entering through inlets located on the external surface of the inflatable canopy. Once the air enters the canopy, it is brought to rest and its temperature is increased to near total temperature conditions of the stream. A natural circulation of gas particles is assumed to be induced over the interior surface of the canopy, creating a flow from which heat is transferred to the inside surface of the canopy by free convection.

The internal heat transfer coefficient for a free convective environment can be estimated using the following relationship:

$$h_{c_i} = 0.13 \left(\frac{k}{s}\right) (Gr \cdot Pr)^{1/3} \quad . \tag{13}$$

The internal heat transfer coefficient is primarily a function of the Grashof number, which in turn is a function of the deceleration loading and the temperature differential surface of the canopy. The Grashof number is represented by the following grouping:

$$Gr = \frac{g\beta\Delta T L^3}{\nu^2} \tag{14}$$

Equation 13 was evaluated as a function of the parametric deployment envelope conditions. The internal heat transfer coefficient was found to vary from 0.01 Btu/hr-sq. ft-deg F for the low deployment Mach number conditions to about 0.1 Btu/hr-sq. ft-deg F for the high deployment Mach number conditions. The latter internal heat transfer coefficient was assumed for all subsequent heat transfer calculations along with the total temperature of the ram gas inside the canopy. The internal wall heating then can be written as

$$q_i = h_{c_i} (T_o - T_{w_i}). \tag{15}$$

Evaluation of Heat Flux Equations - To use equations 3 and 10 in carrying out calculations, the pressure distribution must be specified for the particular vehicle-decelerator configuration in question. The other inviscid flow properties can then be calculated assuming the flow expands isentropically from the stagnation conditions at the nose. The Rankine-Hugoniot normal shock relations determine the stagnation point properties and the isentropic flow equations are used to calculate the flow properties at the edge of the boundary layer. The pressure distribution (see Figure 15) used

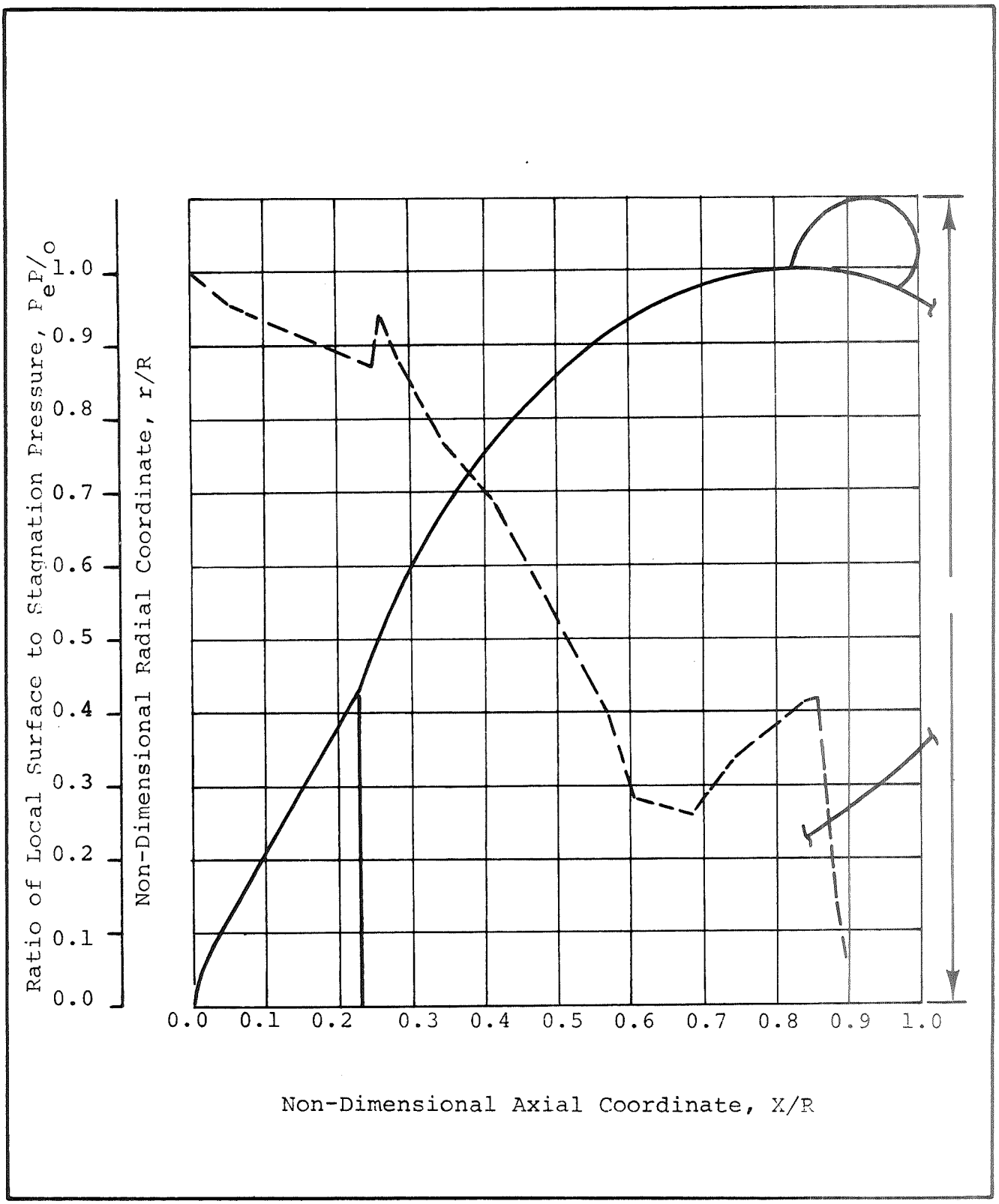

Figure 15 - AID Pressure Distribution

in evaluating the heat flux equations was obtained from Reference 20. The vehicle-decelerator profile from which the measured distribution was obtained is essentially the same profile considered for this study. While the referenced distribution was obtained at a Mach 3.0 condition it is believed the data, when plotted in the form of p_e/p_o, is equally valid over the Mach number range of interest here. An indication of this is provided by noting that the pressure distributions when presented in the form of P_e/p_o, presented in References 21 and 22 for a 120 and 140-deg cone, respectively, correlate independent of M_∞ for Mach numbers between 2.0 and 4.63.

The remaining quantities used to evaluate the boundary layer heat flux equations are summarized in Table III.

TABLE III - INPUT PROPERTIES TO HEAT FLUX EQUATIONS (PARAMETRIC STUDY)

Property	Symbol	Value
Specific heat	c_p	0.166 Btu/lb - F
Joules constant	J	778 ft-lb/Btu
Gravitational constant	g_o	32.2 ft/sec^2
Molecular weight	m	44.0 lb/lb - mole
Ratio of specific heats	γ	1.37
Constants for Sutherland's viscosity equation	C_1 C_2	2.43×10^{-8} 4.43

Transient Heat Conduction Equations - The temperature distribution within the canopy material was calculated on the basis of transient one-dimensional heat conduction within the multi-material canopy wall configuration with prescribed heating conditions at both the external and internal surfaces. A sketch of the heat balance model is shown in Figure 16. A heat balance is prescribed for each layer into which the multi-material canopy wall is divided on the basis of

$$Q_{in} - Q_{out} = Q_{stored}. \qquad (16)$$

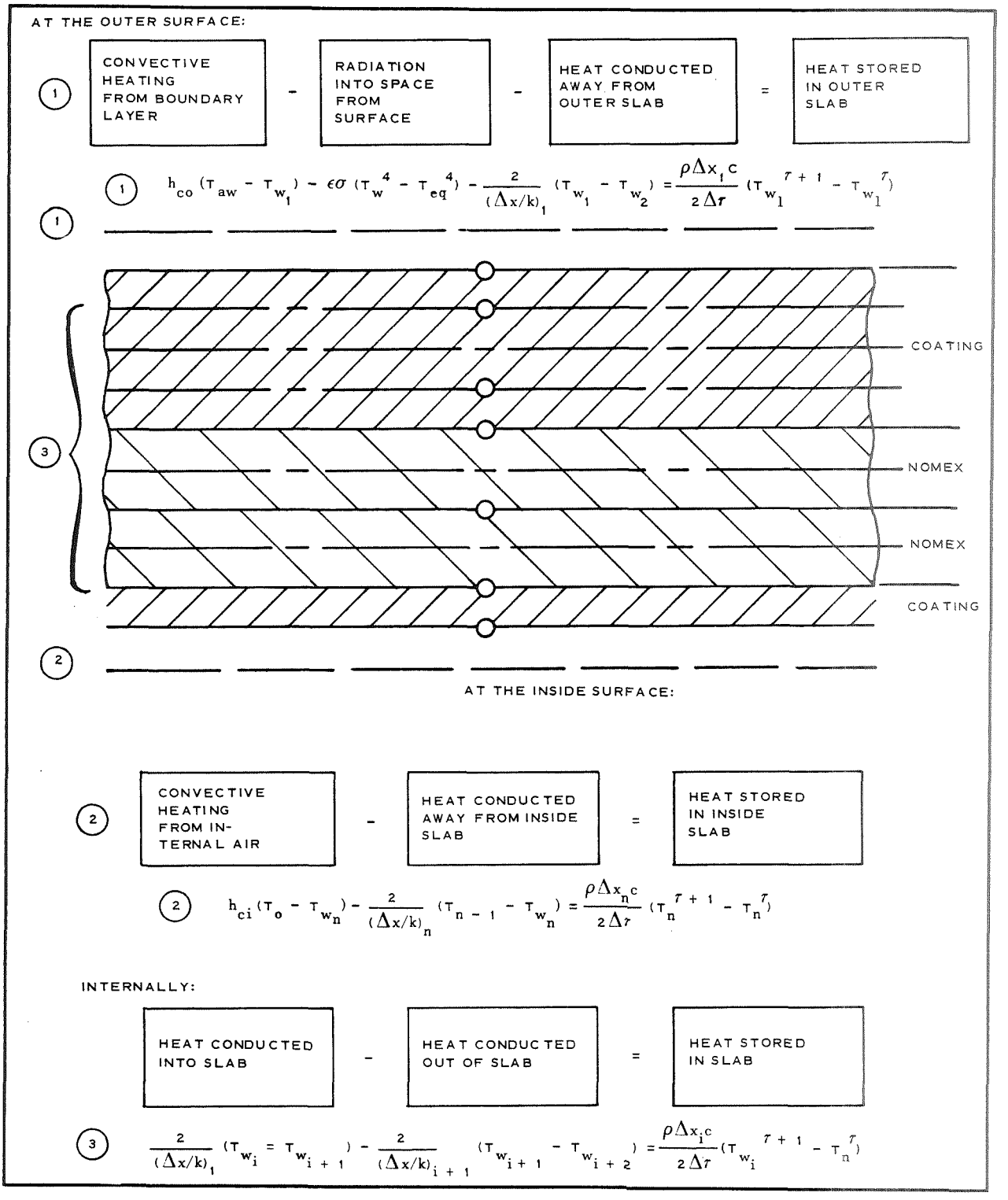

Figure 16 - Heat Balance Model

The exact equations defining this heat balance at each layer are shown in Figure 16. The equations are coupled to the aerodynamic heating from the boundary layer at the outside surface by the external heat transfer coefficient and adiabatic wall temperature; and to the internal heating at the inside surface, by the internal heat transfer coefficient and the total temperature of the gas within the inflated canopy.

Thermal Characteristics of Materials - The physical properties of the HT-189-47 Nomex fabric considered in this investigation are listed in Table IV. While the thermal properties of the material are not known, the properties of a similar Nomex fabric were available. The physical and thermal properties of this reference material and the Viton coating are also presented in Table IV.

TABLE IV - PROPERTIES OF MATERIALS

Item	Material		
	HT-1, Type 1* (REF)	HT-189-47	Viton
Weave	74 ends/in. 71 picks/in.	82 ends/in. 92 picks/in.	. . . . . .
Twist	6.3 warp 6.3 fill	No data available No data available	. . . . . .
W/A (oz/sq. yd.)	1.95	2.3	ρ = 115 lb/cu. ft.
Thickness (in.)	0.00675	0.008	. . .
Specific Heat (Btu/lb-F)	0.35	0.35	0.395
Thermal conductance (Btu/hr-ft-F)	See Figure 17	See Figure 17	0.117

*Data obtained from Reference 23

The thermal conductance of the reference Nomex cloth is shown in Figure 17. Test data for the reference Nomex fabric showed a value of thermal conductance ranging from a low value of 0.008 Btu/hr-ft-F at 400F with vacuum conditions to a high value of 0.028 Btu/hr-ft-F at 700F with ambient pressure conditions. A thermal conductance of 0.02 Btu/hr-ft-F was assumed for the study. This value of thermal conductance may be regarded as conservative since the application of the material takes place at a low pressure.

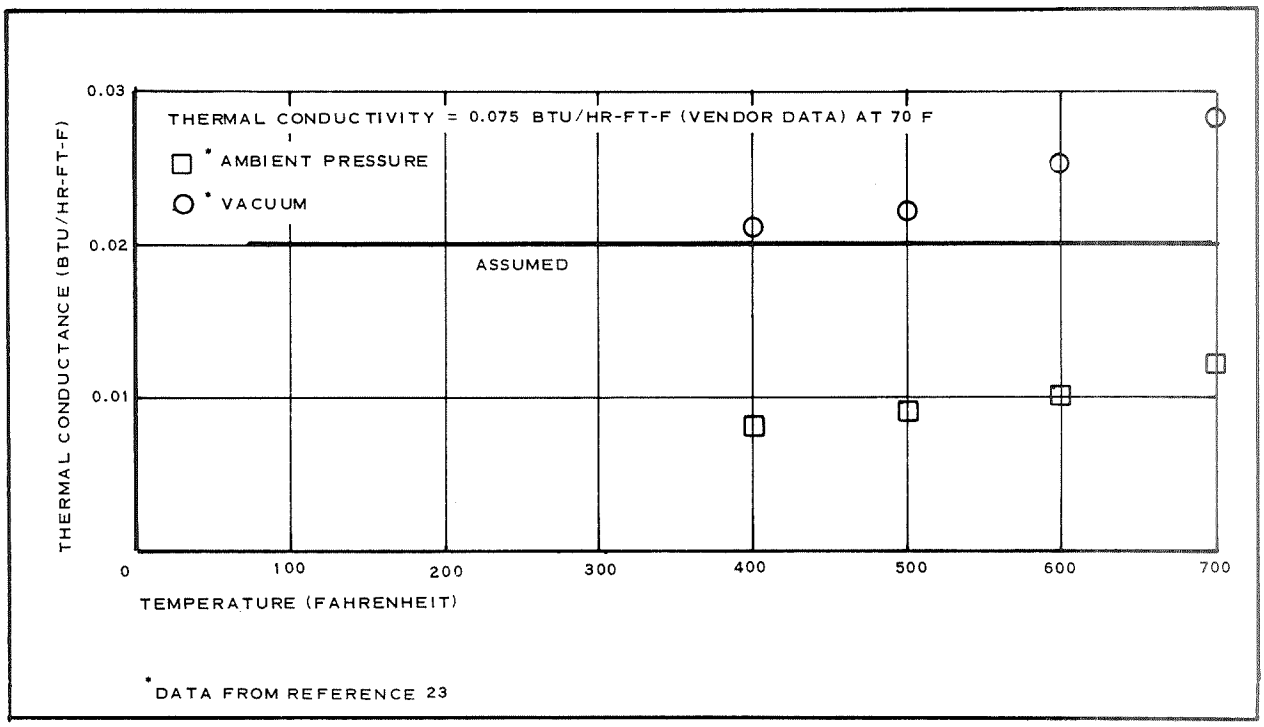

Figure 17 - Thermal Conductance of Nomex

Heat Flux Rates - Figures 18 through 22 present heat flux rates versus time from deployment for the deployed AID trajectories presented in Figures 8 through 12 excluding the nominal trajectories of those figures. Heat flux rates are presented for each of the three canopy stations and the stagnation point.

In general, the heat flux rates to the inflated canopy surface are higher than at the stagnation point of the vehicle and are the result of a turbulent boundary layer existing at the particular station. Deployment at a Mach number of 8 results in the largest heat flux inputs to the entry vehicle for all ballistic paremeters considered. The initial cold wall heat flux rate to the canopy surface varies from 5.0 Btu/sq. ft-sec to about 9.5 Btu/sq. ft-sec as the ballistic parameter is increased from 0.3 slugs/sq. ft. to 0.7 slugs/sq. ft. at a deployment Mach number of 8. These initial cold wall heat flux rates quickly decrease as the deployment Mach number is reduced for all ballistic coefficients considered. The heat flux is highest at Station 2 in all cases except for the B_E = 0.6 case where deployment at M_D = 8 results in the highest heat flux rate occurring at Station 1, which in most cases was found to be in a laminar boundary layer zone.

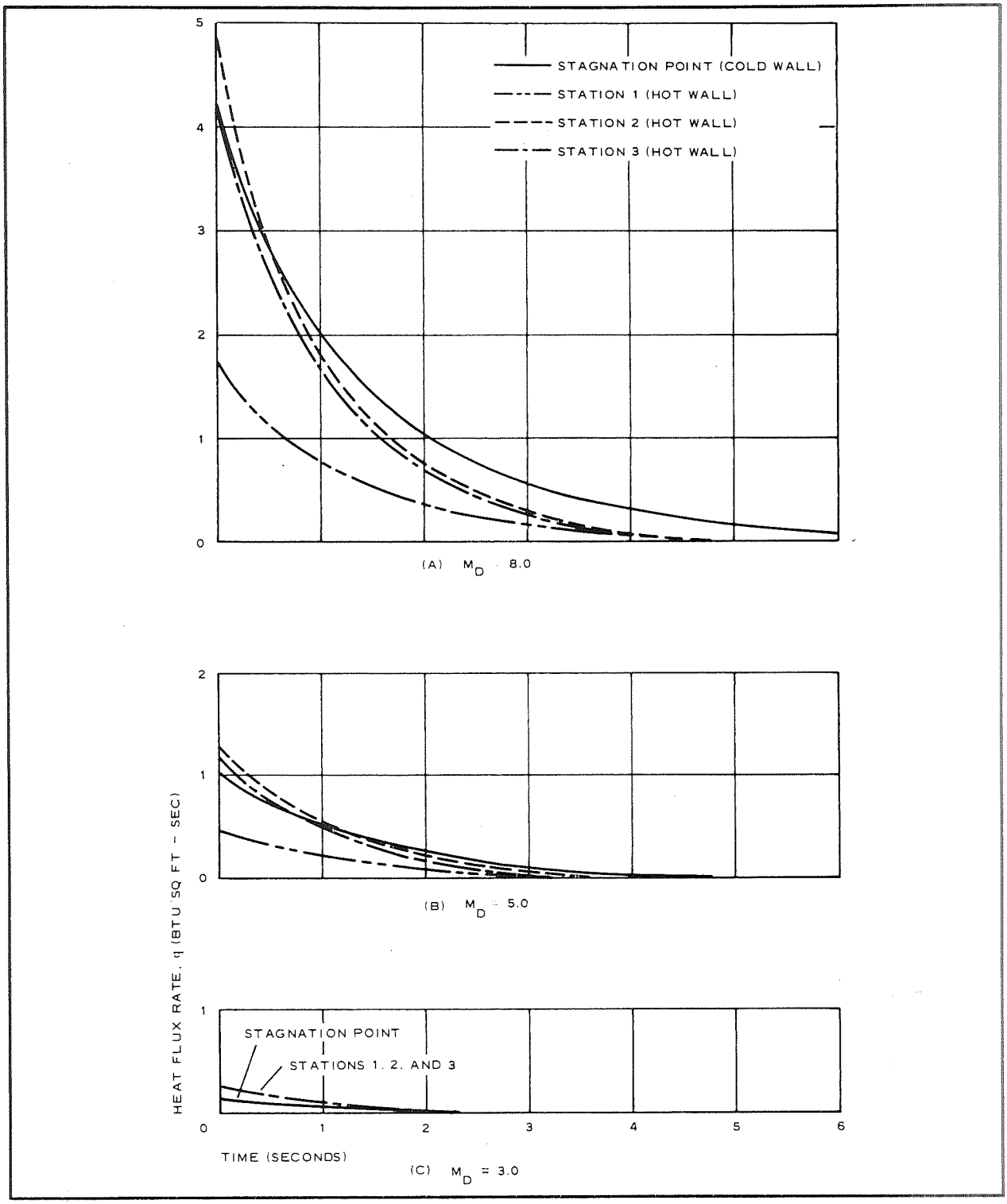

Figure 18 - Heat Flux Rate versus Time (B_E = 0.3)

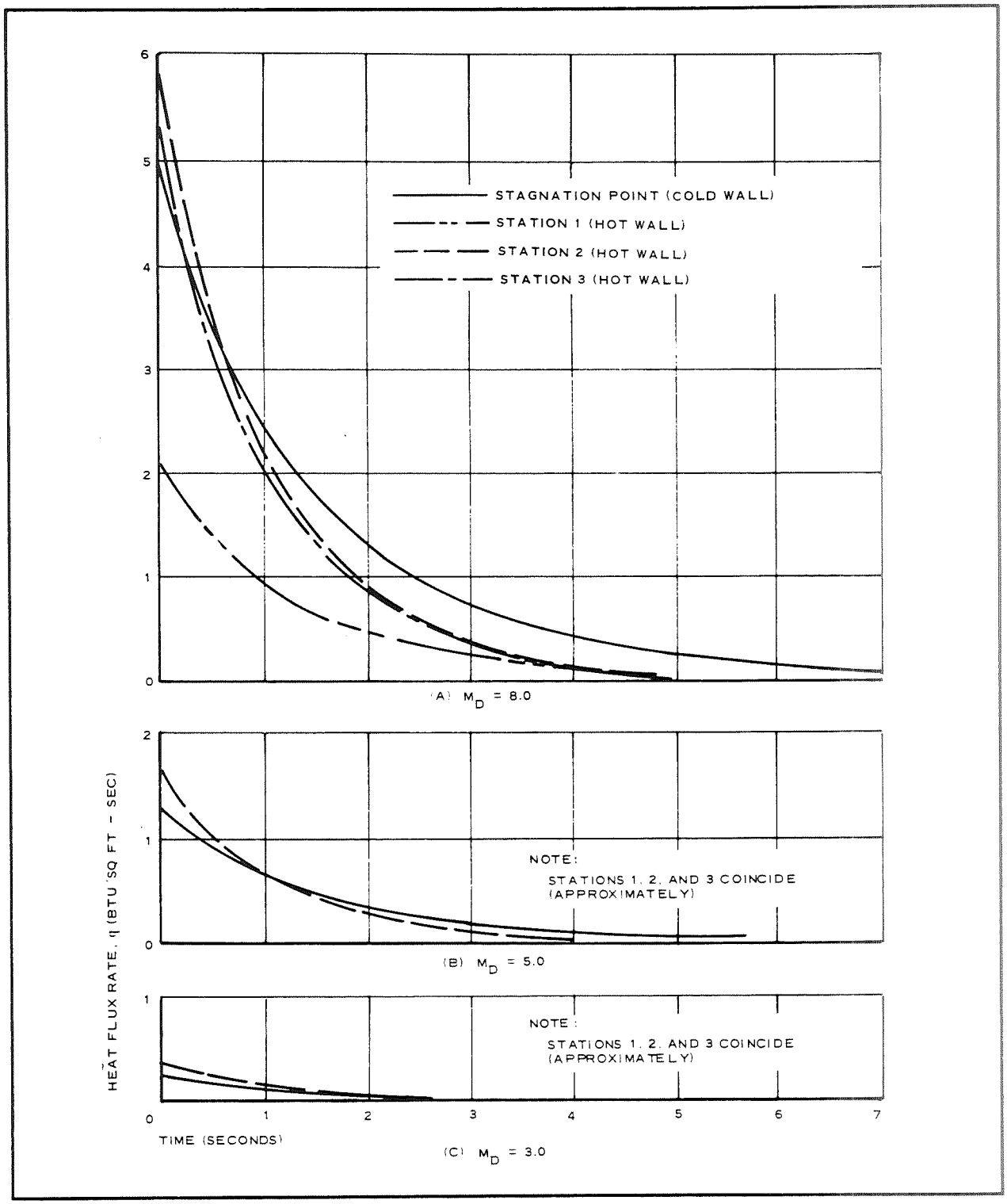

Figure 19 - Heat Flux Rate versus Time (B_E = 0.4)

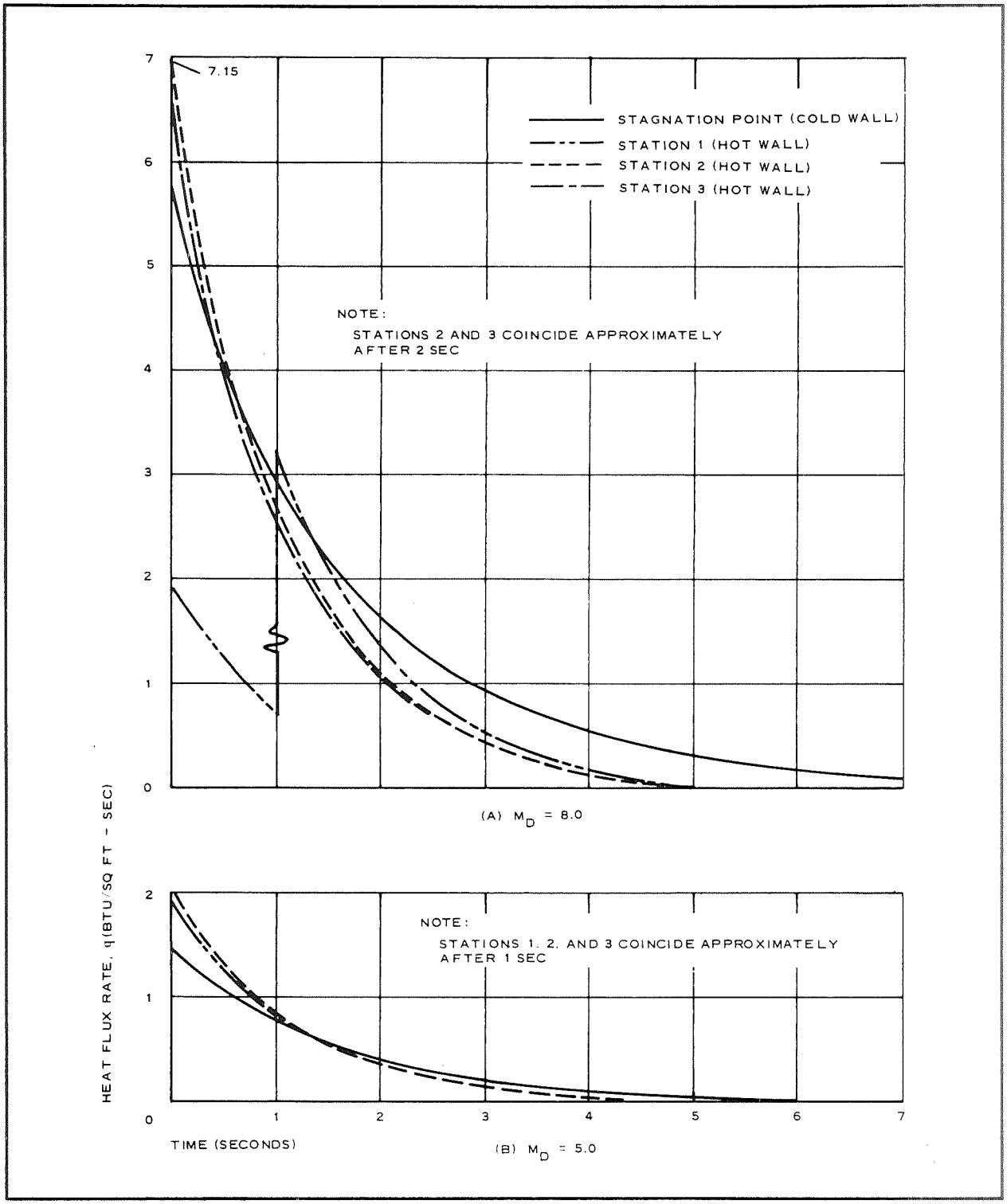

Figure 20 - Heat Flux Rate versus Time (B_E = 0.5)

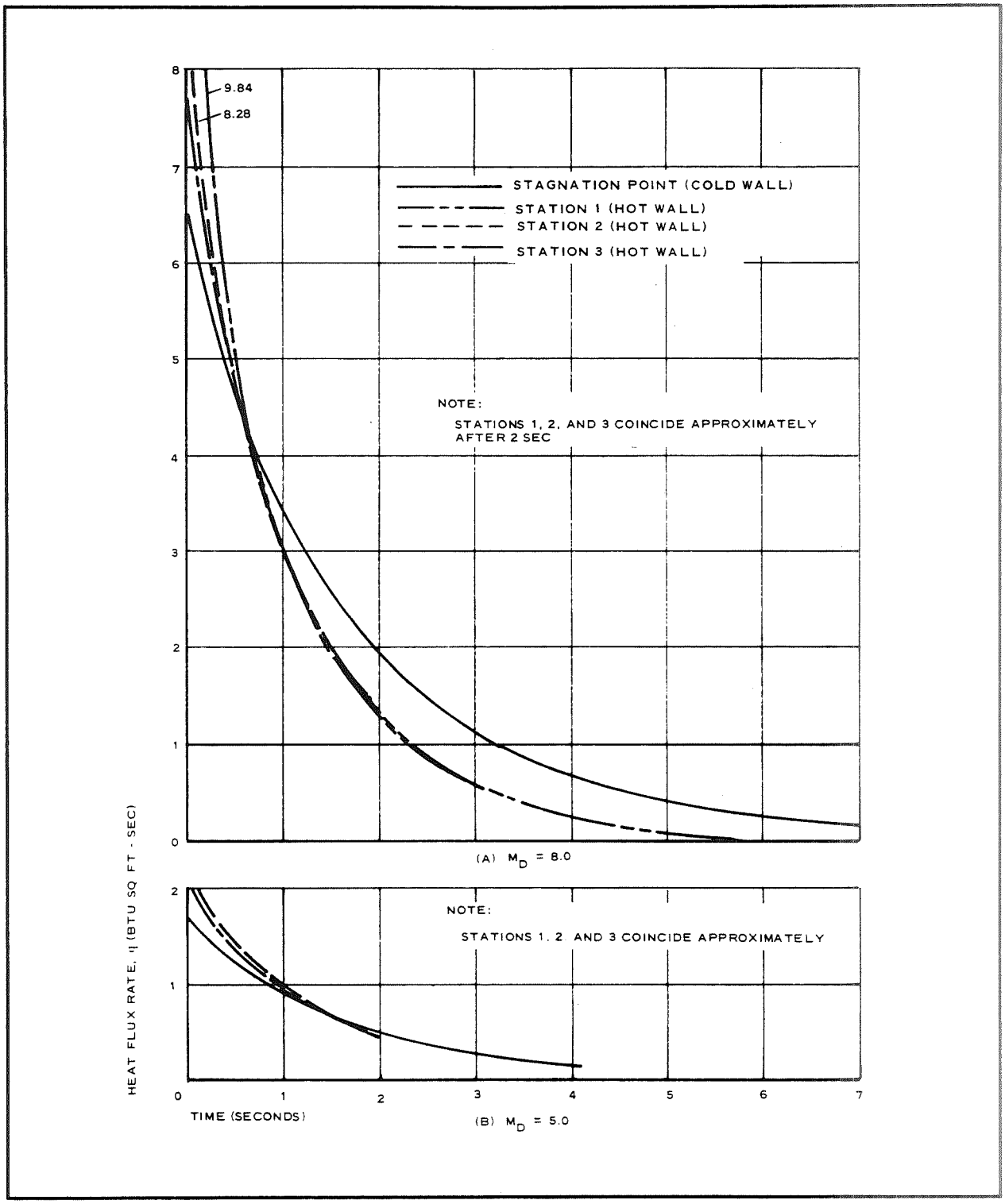

Figure 21 - Heat Flux Rate versus Time (B_E = 0.6)

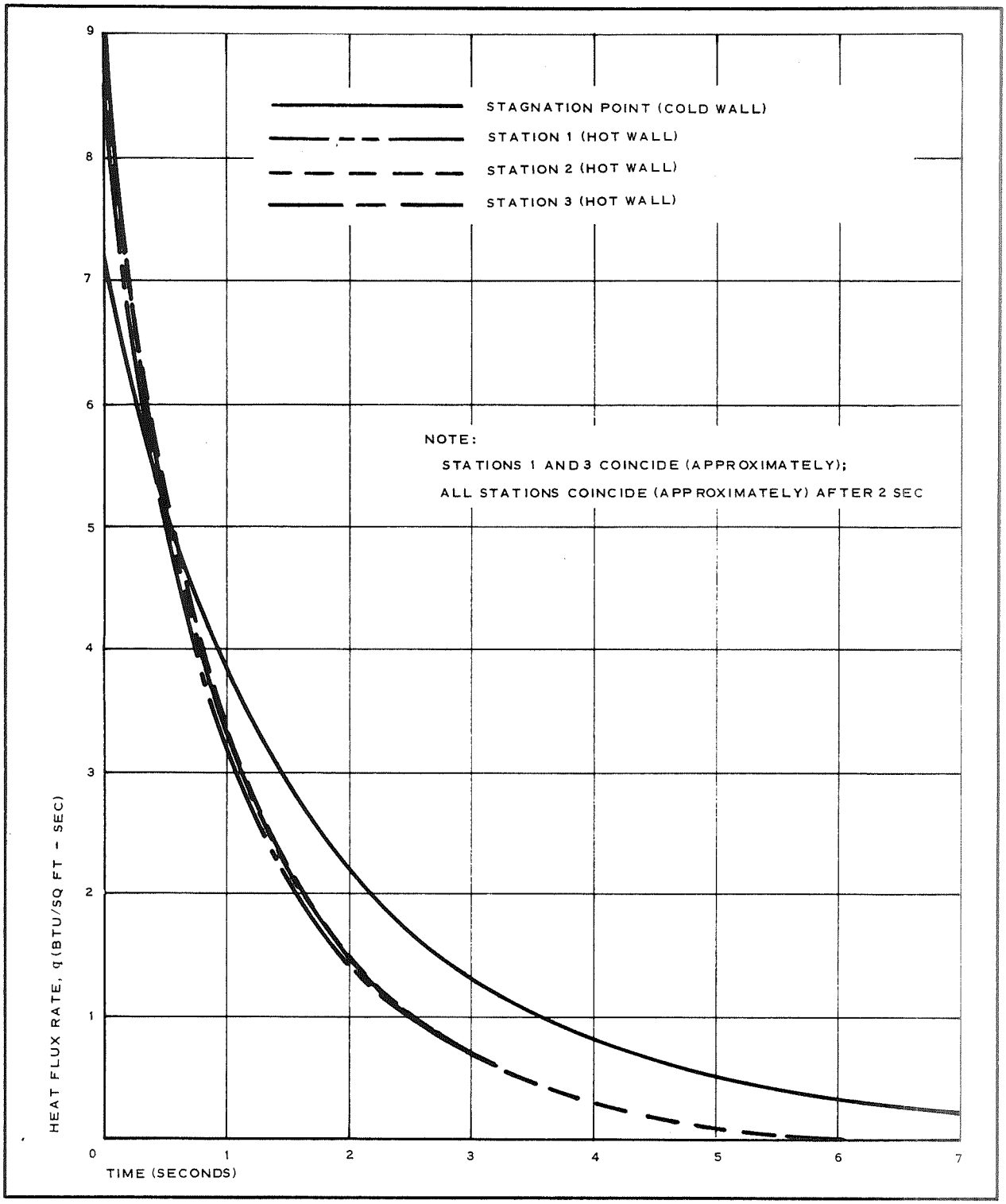

Figure 22- Heat Flux Rate versus Time (B_E = 0.7)

While the internal heat flux rates have been accounted for during the current analysis, their contribution in raising the canopy temperature is minor compared to the external rates.

Nomex Temperatures - The results of the thermal analysis have been summarized, as lines of maximum temperature superimposed on a Mach number - ballistic coefficient envelope for a given coating weight in Figures 23, 24, and 25. The Mach number-ballistic coefficient envelope was established by the deployment cases summarized in Table II. The nominal deployment conditions are also denoted in Figures 23, 24, and 25.

As indicated in Figures 23, 24, and 25, increasing the coating weight has the effect of increasing the Mach number at which deployment can take place without exceeding the fabric temperature limitations. While certain of the temperature cases presented in Figures 23, 24, and 25 are in excess of the "zero strength temperature," this does not imply such cases were considered in the subsequent stress and weight analysis. To insure that the fabric temperature limitations were not exceeded, a 600F working temperature limit was imposed on the Nomex during the weight analysis.

The Nomex meridional tapes which overlay the fabric, were assumed to experience the same temperatures which the fabric sees.

Figure 26 shows the effect that increasing the deployment Mach number has on the fabric temperature for a given B_E and coating weight. Station S_2 was selected, since for the case shown, S_2 resulted in the maximum fabric temperature. As noted previously, station S_2 results in the maximum heat flux rates and therefore maximum temperature in all cases except for B_E = 0.6 slugs/sq. ft.

Figure 27 shows the effect of station position on the fabric temperature for a given Mach number, B_E, and coating weight. The reason for the temperature at station S_1 being significantly lower than that at S_2 and S_3 is the existance of a laminar boundary layer at S_1. Also, the dynamic pressure decay after deployment is shown in Figure 27.

The relationship of the maximum temperature and dynamic pressure profiles must be considered when arriving at the "worst case" combination of the thermal and pressure loading on the canopy. The approach used to determine the point where the worst case occurs is discussed in detail in the stress analysis section.

Figure 28 shows a Mach number and ballistic coefficient, for a 1.0 oz/sq. yd. coating weight, which resulted in station S_3 experiencing the maximum temperature. Figure 29 shows the effect of coating thickness in reducing the fabric temperature for a given Mach number and B_E. In this case,

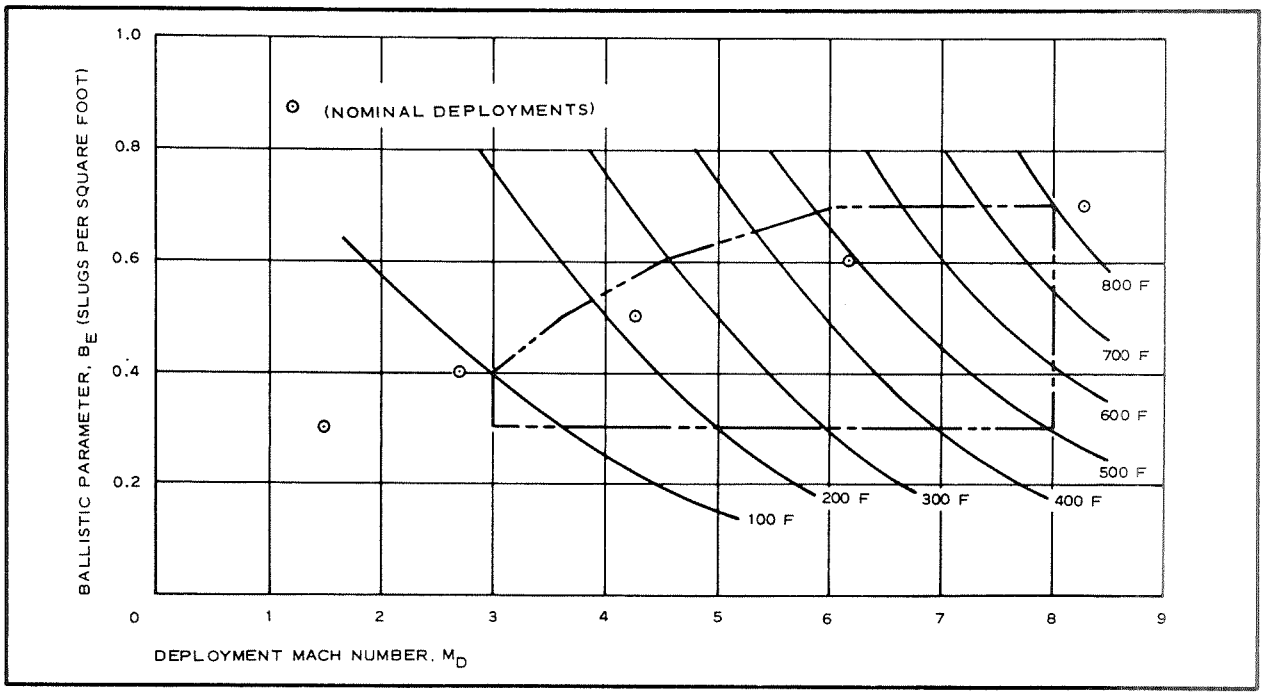

Figure 23 - Temperature Effects on Deployment Envelope
(Viton Coating = 1 Oz/Sq Yd)

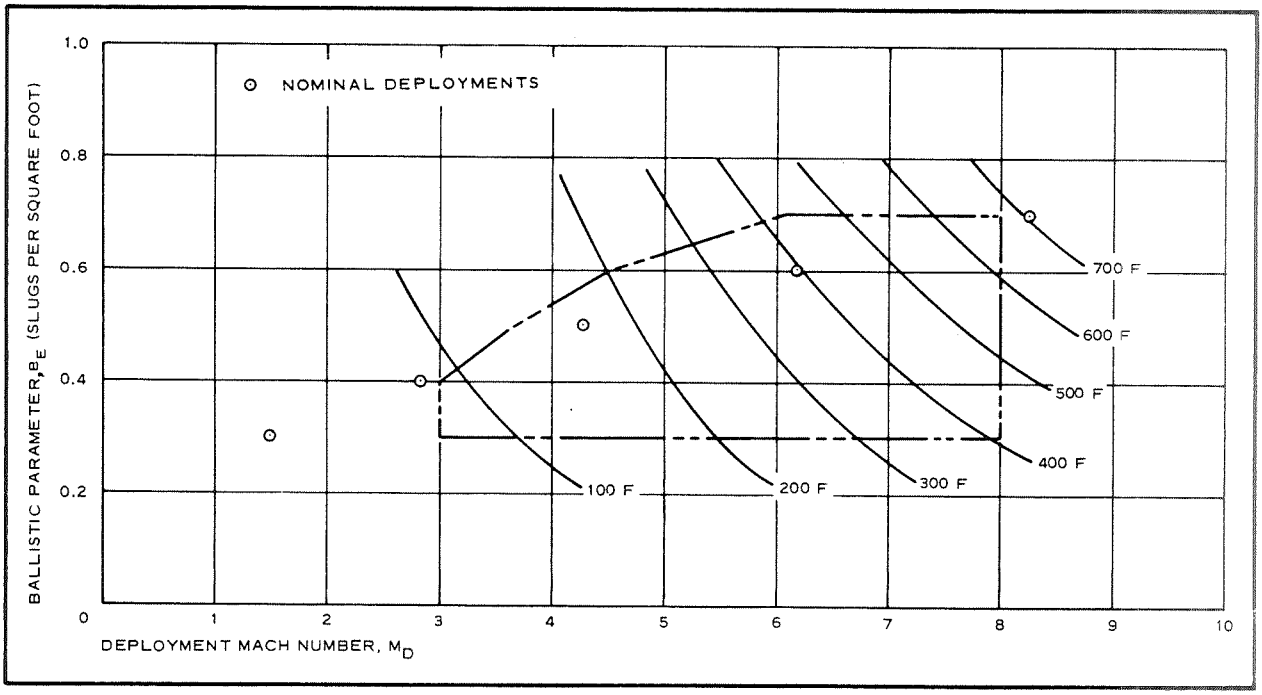

Figure 24 - Temperature Effects on Deployment Envelope
(Viton Coating = 3 Oz/Sq Yd)

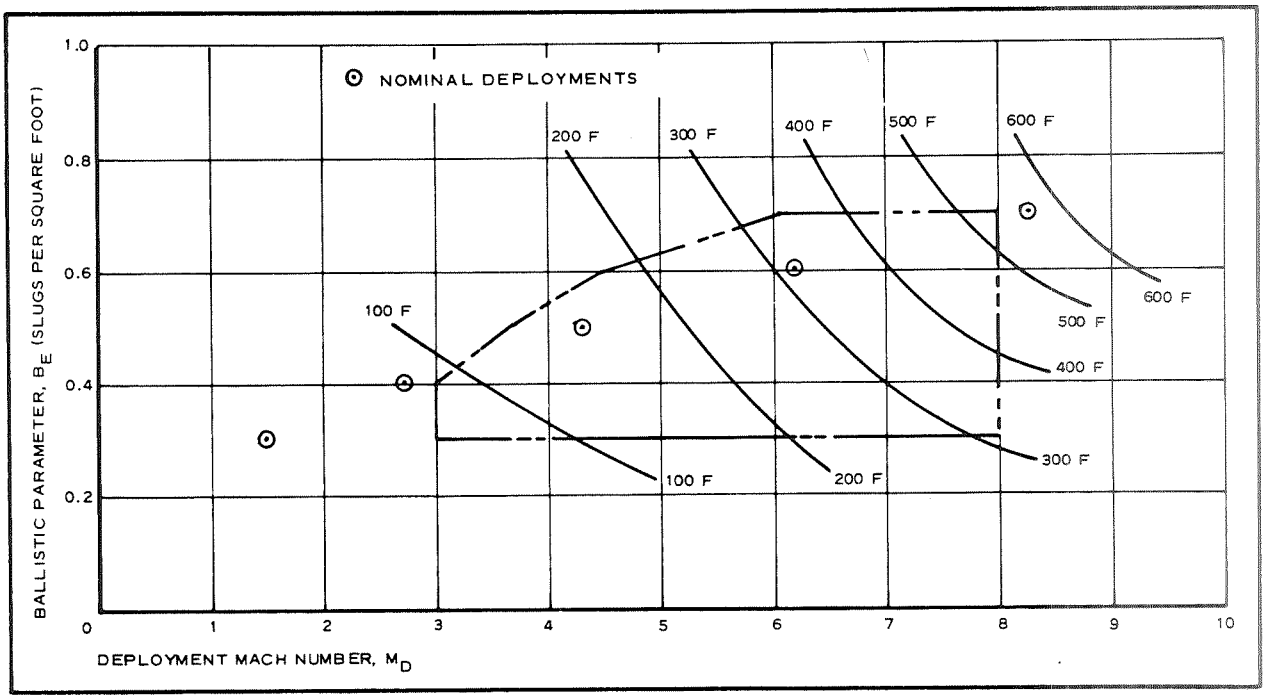

Figure 25 - Temperature Effects on Deployment Envelope (Viton Coating = 6 Oz/Sq Yd)

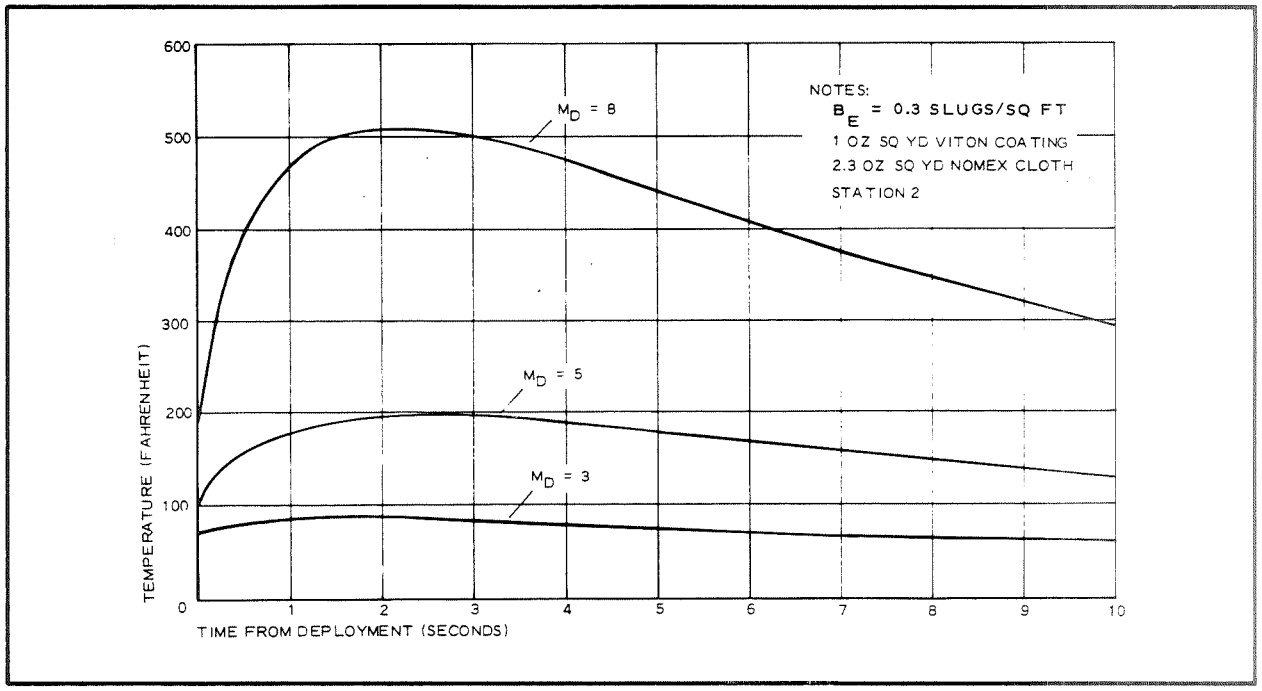

Figure 26 - Nomex Cloth Temperature versus Time (B_E = 0.3)

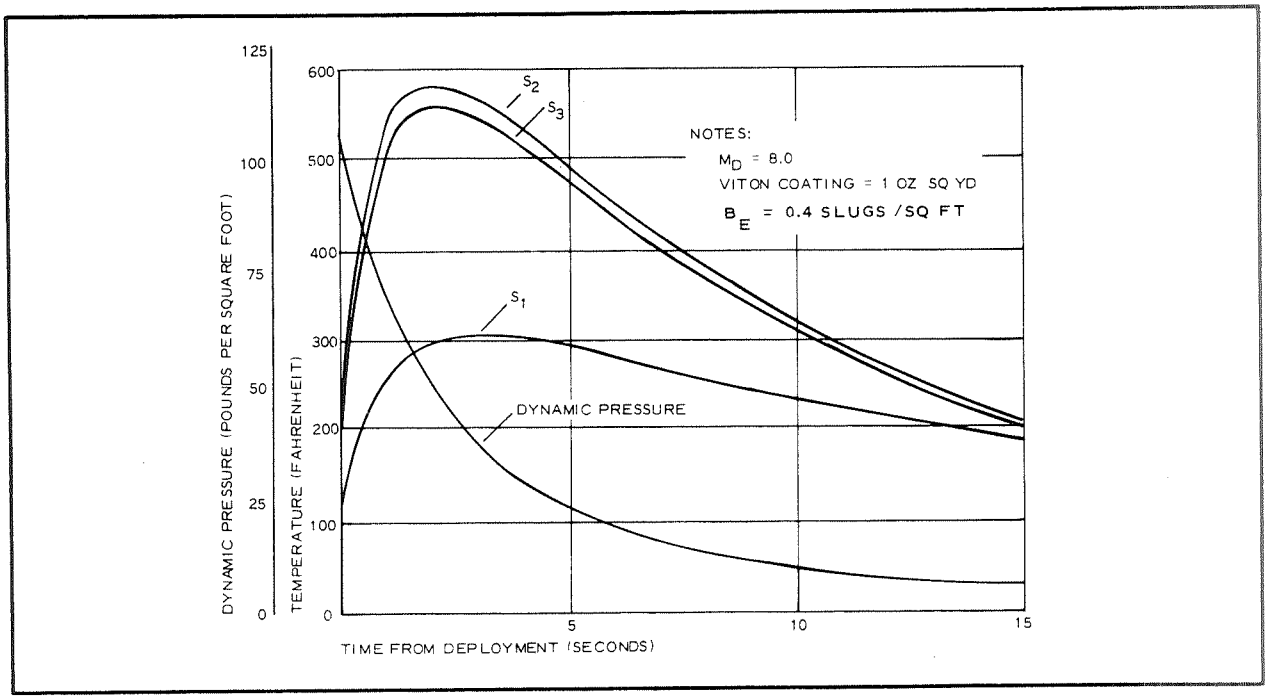

Figure 27 - Nomex Cloth Temperature versus Time (B_E = 0.4)

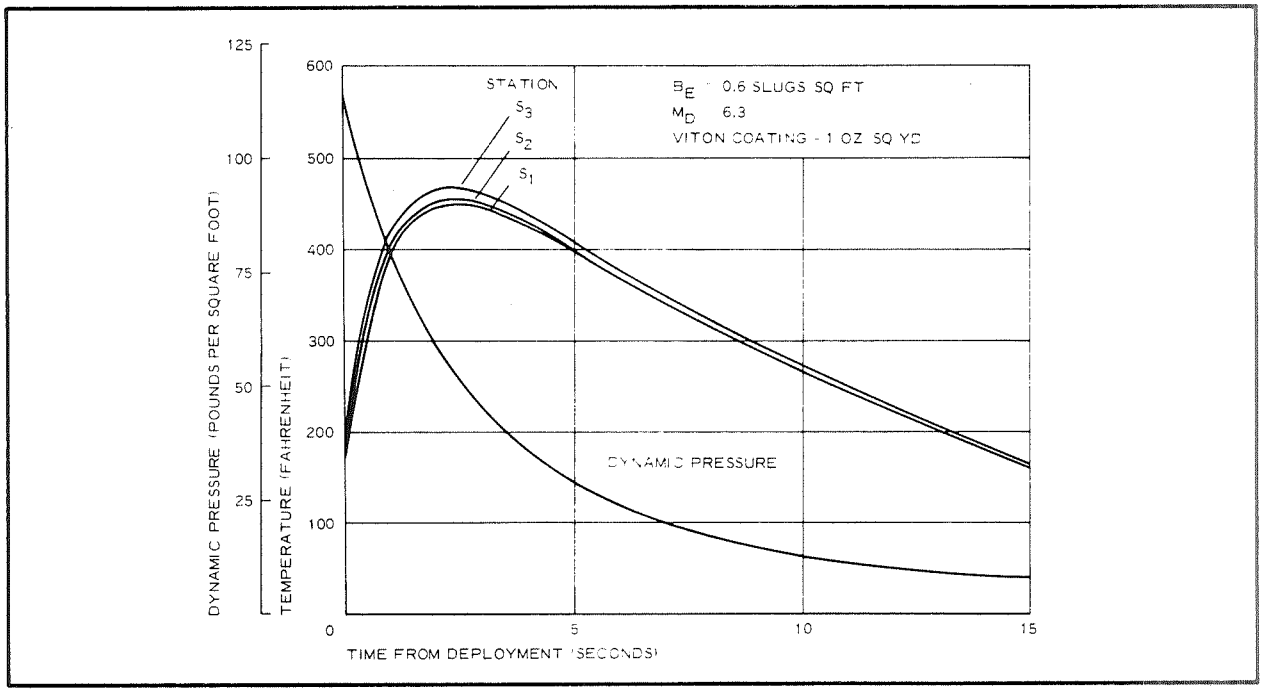

Figure 28 - Nomex Cloth Temperature versus Time (B_E = 0.6)

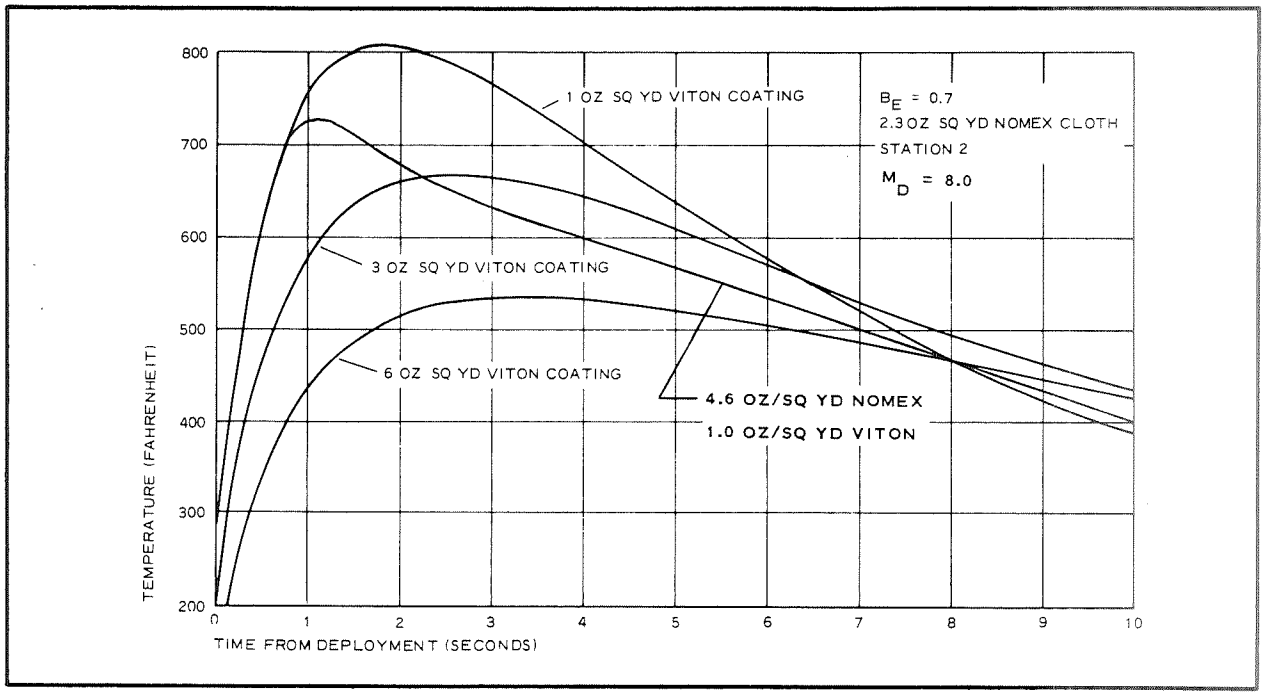

Figure 29 - Nomex Cloth Temperature versus Time (B_E = 0.7)

where M_D = 8.0 and B_E = 0.7 slugs/sq. ft., 6.0 oz/sq. yd. of coating are required to reduce the Nomex below the 600 F working temperature limit. The dashed curve on the figure shows the effect of increasing cloth weight to 4.6 oz/yd^2 with 1.0 oz/yd^2 Viton coating. Calculations indicate peak temperature is above the Nomex working temperature and is slightly higher than the temperature of the 2.3 oz/yd^2 fabric with 3 oz/yd^2 coating.

Stress Analysis

The AID is basically a uniform-stress (isotensoid) structure as described in Reference 7. The isotensoid theory requires uniform stresses throughout the fabric with both principal fabric stresses (meridional and circumferential) being equal. Hence the excess meridional forces are carried by many meridional tapes overlaying the fabric. Additionally, the theory requires a constant tension over the entire length of the meridian. A discussion and development of the basic isotensoid relationships, are presented in Appendix B. Additionally, Appendix B presents the derivation of a merit function which will be used in the following parametric weight analysis.

AID Parametric Weight Analysis - The merit function as derived in Appendix B is,

$$\frac{W_s}{C_D A} = \frac{K_D}{(C_D\pi)^{1/2} k_c (1-\xi^2)^{3/2}} \left[\frac{p/q}{C_D} \frac{l_m}{R'} \frac{\bar{T}}{(1+2\eta)^3}\right] q\sqrt{C_D A} \qquad (17)$$

$$+ \frac{K_c d_f}{C_D (1-\xi^2)(1+2\eta)^2} \left[\frac{A_f}{\pi R'^2} + 4\pi\eta(1+\eta)\right]$$

where

$$d_f = \left[\frac{K_D \beta \bar{f}}{2(1-\xi^2)^{1/2}(1+2\eta) k_f \sqrt{C_D\pi}}\right] \left(\frac{p}{q}\right) q \sqrt{C_D A} \quad . \qquad (18)$$

The first and second terms on the right-hand side of Equation 17 reflect the mass of the meridian cords and the mass of the fabric, respectively. Both of these terms and the coating required to provide thermal protection will be evaluated separately and later summed to determine the total AID weight for each of the deployment conditions of Table II. Certain of the quanities needed to evaluate the terms of Equation 17 are presented or derived in Appendix B. Letting W_m denote the total meridian weight and substituting the appropriate values presented in Appendix B into the first term of Equation 17, the following expression is obtained.

$$\frac{k_c W_m}{K_D q} (C_D A)^{-3/2} = \frac{\left(\frac{1.92}{1.07}\right)(2.479)\left(\frac{0.52}{1.33}\right)}{\sqrt{1.07\pi}(1-0.16)^{3/2}}$$

$$= 1.231 \quad . \qquad (19)$$

Letting W_f denote the total fabric weight, excluding any coating, and substituting the appropriate values presented in Appendix B into the second term of equation 17, the following expression is obtained

$$(C_D A)^{-1} \frac{W_f}{d_f} = \frac{1.4}{1.07(1.21)(1-0.16)} \left[2.904 + 4\pi(0.05)(1.05)\right]$$

$$= 4.588 \quad . \qquad (20)$$

Substituting the appropriate values from Appendix B into Equation 18 the following expression is obtained:

$$\frac{k_f d_f}{K_D q} (C_D A)^{-1/2} = \frac{(1.294)(0.1)(1.92)}{2(1.1)(1 - 0.16)^{1/2}\sqrt{1.07\pi}} \qquad (21)$$

$$= 0.0672 \ .$$

Further simplifing Equations 19, 20, and 21, respectively, the following relations are obtained:

$$\frac{k_c W_m}{K_D q R^3} = (1.231)(4.7449) = 5.811 \quad ; \qquad (22)$$

$$\frac{W_f}{d_f R^2} = (4.588)(2.8237) = 12.956 \quad ; \qquad (23)$$

$$\frac{k_f d_f}{K_D q R} = (0.0672)(1.6804) = 0.1129 \ . \qquad (24)$$

The above equations are for strength limited designs. For minimum gage designs the fabric weight becomes simply:

$$\frac{W_f}{R^2} = 12.956\ d_{min}$$

When the fabric is minimum gage the use of equation (22) for the meridians may be unconservative because it implies the meridians are loaded at a fully stressed condition while the fabric may be at a lower stress. Hence, a strain incompatibility would exist. A conservative assumption is to keep the ratio of meridian force to allowable meridian force the same as the ratio of fabric stress to allowable fabric stress. This implies strain compatibility between the fabric and meridian if both are assumed to have the same load-elongation characteristics. This ratio is equal to the ratio of d_f given by strength limited considerations (eg. 24) to d_{min}. Applying this ratio as a reduction in the allowable strength of the meridians the weight can be determined from equation (22) as

$$W_m = \frac{5.811}{0.1129} \frac{k_f}{k_c} R^2 d_{min} \quad \begin{matrix}\text{(strain compatibility} \\ \text{for minimum gage} \\ \text{fabric)}\end{matrix} \qquad (25)$$

where k_f/k_c is obtained from Figure 30

The thermal analysis has been conducted for a 20-ft-diameter AID constructed of Nomex cloth weighing 2.3 oz/sq. yd. with Viton coating weights of 1, 3, and 6 oz/sq. yd. From Equation 25, the minimum gage fabric plus coating weight for each of the coating weights considered in the thermal analysis are:

$$W_{mf_1} = 1295.2 \left(\frac{2.3 + 1}{144}\right) = 29.7 \text{ lb (for 1 oz/sq yd coating)}; \quad (26)$$

$$W_{mf_3} = 47.7 \text{ lb (for 3 oz/sq yd coating)} ; \quad (27)$$

and

$$W_{mf_6} = 74.7 \text{ lb (for 6 oz/sq yd coating)} ; \quad (28)$$

Heavier fabrics are required only when

$$\left(\frac{q}{k_f}\right) K_D \geqq 0.01415 \text{ lb/cu ft}, \quad (29)$$

which results by setting d_f = 2.3 oz/sq yd in Equation 24.

The left side of Equation 29 is time dependent since, after deployment, the dynamic pressure (q) is continually decreasing until a terminal descent condition is reached and the strength-to-weight ratio (k_f) decreases until the maximum fabric temperature is reached and then increases again as the fabric temperature decreases (see Figure 27). The point in time after deployment for which the parameter (q/k_f) K_D is a maximum represents the worst case or design condition for a particular deployment case. The maximum value of (q/k_f) for a particular deployment was determined by selecting, for several points in time between deployment and the maximum temperature, values of dynamic pressure and the corresponding temperatures. From these temperatures, strength-to-weight ratios were determined from Figure 30 and the parameter (q/k_f) evaluated, assuming a 600°F working limit for Nomex, for the maximum design factor (K_D = 3.0) of interest during this study (see Appendix B). This evaluation indicated that minimum gage fabric provides sufficient strength in all cases. (See eq. 29). Therefore, the fabric weights for the 1.0, 3.0, and 6.0 oz/sq yd coating weights are specified by Equations 26, 27, and 28 respectively.

The meridian weights for each deployment case, which must be added to the fabric weights in order to determine the total structural weight, can be determined by evaluating Equation 22 (strength limited) and equation 26 (strain limited) for R = 10 ft., the values of (q/k_c) max presented in Figure 31 and the range of design factors of interest. Figure 32 through 36 present the results of the meridian weight calculations. Results are not presented for cases in which the 600F working limit temperature was exceeded (see Figures 23, 24, and 25).

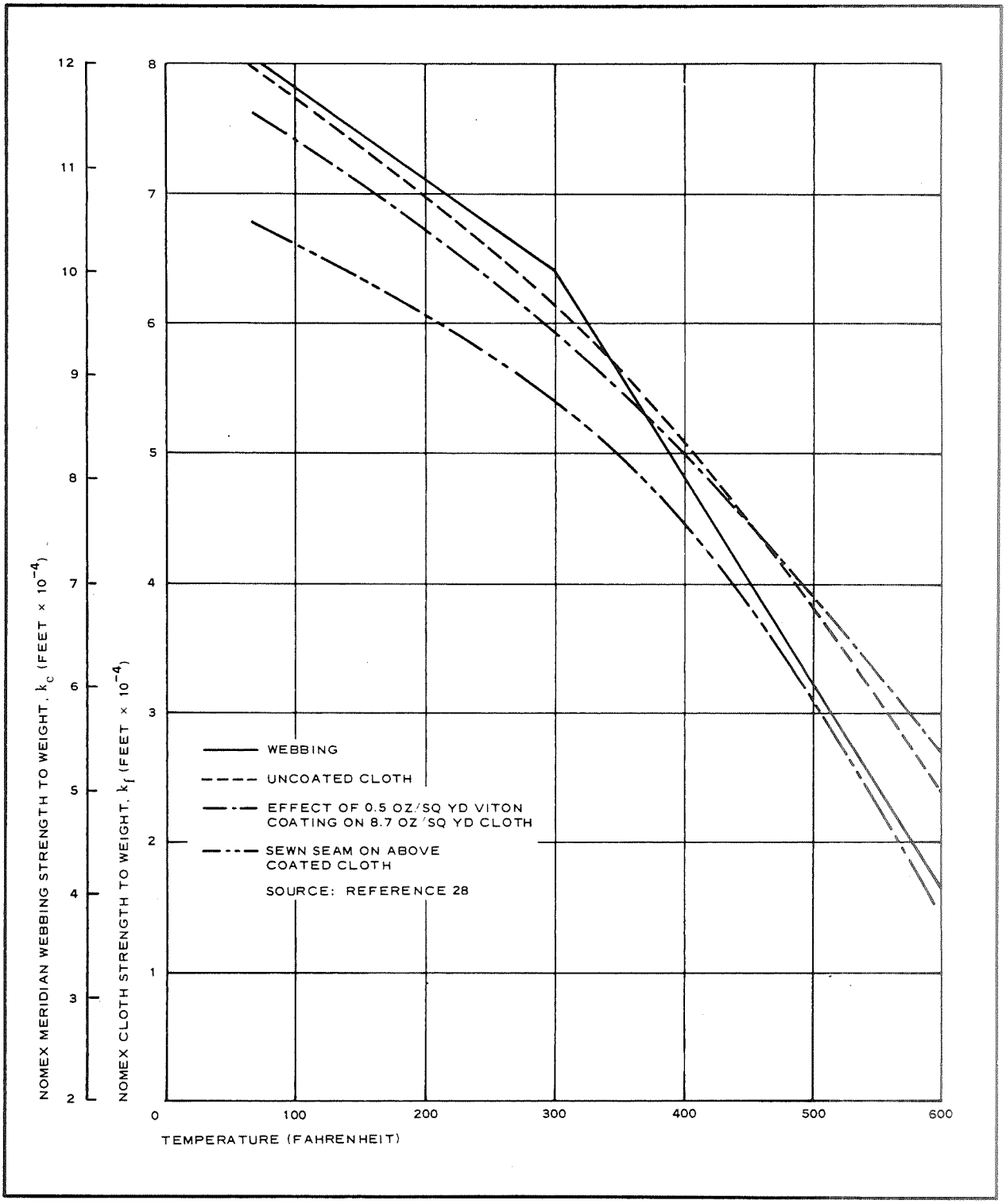

Figure 30 - Strength-to-Weight Ratio versus Temperature for Nomex Webbing and Cloth

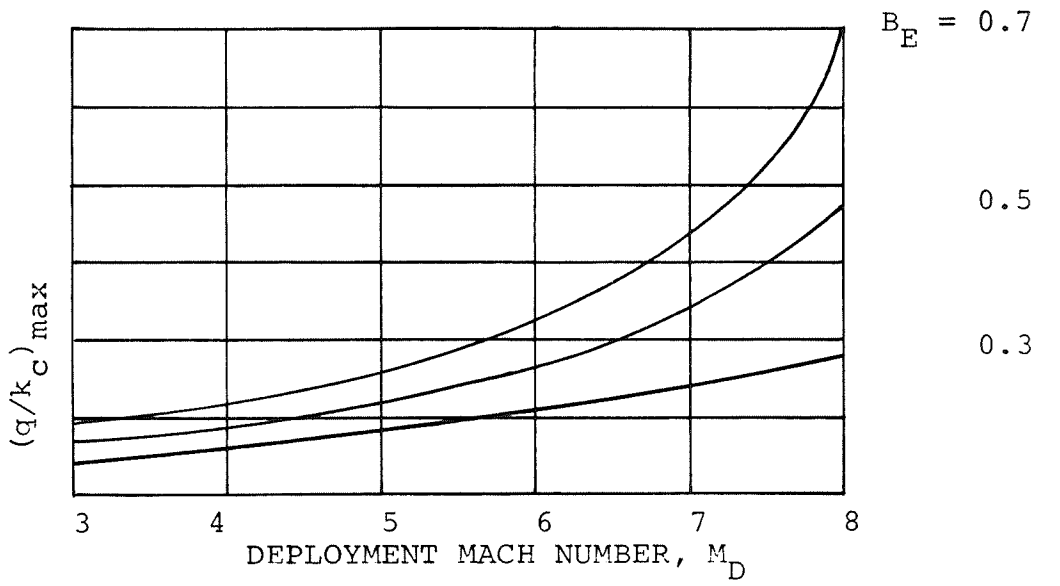

a) 1.0 Oz/Sq Yd COATING WEIGHT

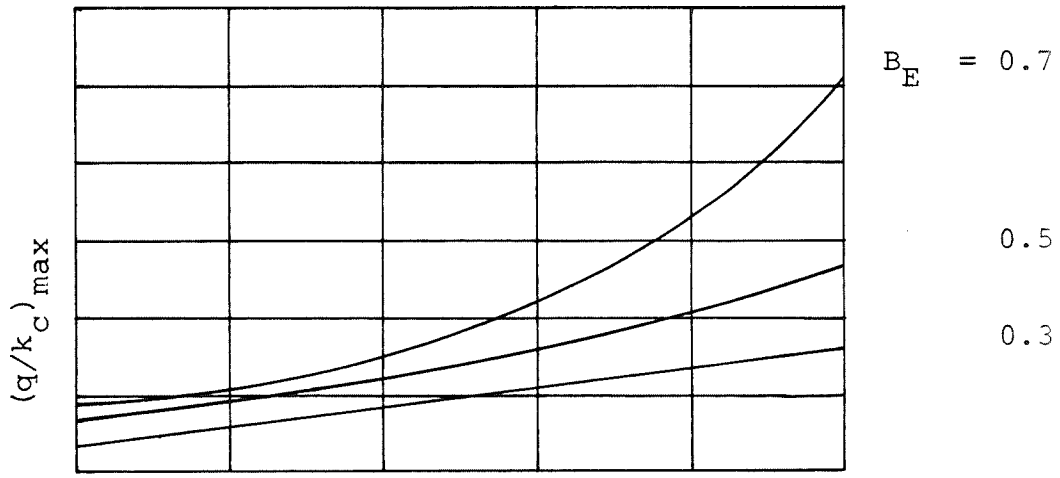

b) 3.0 oz/Sq Yd COATING WEIGHT

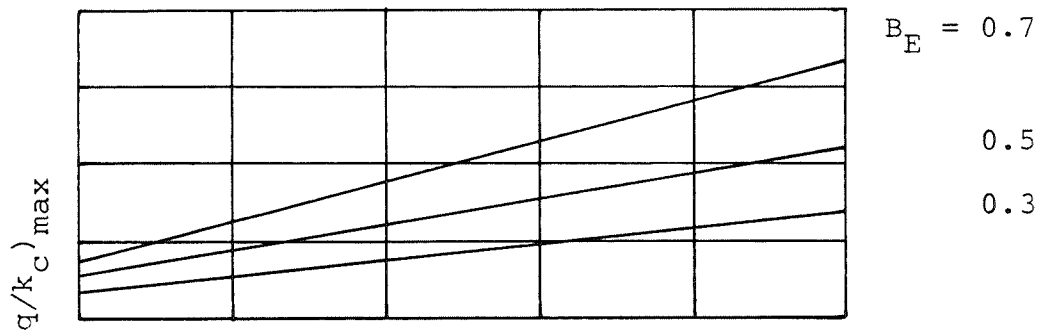

c) 6.0 oz/Sq Yd COATING WEIGHT

Figure 31 - $(q/k_c)_{max}$ Versus Deployment Mach Number

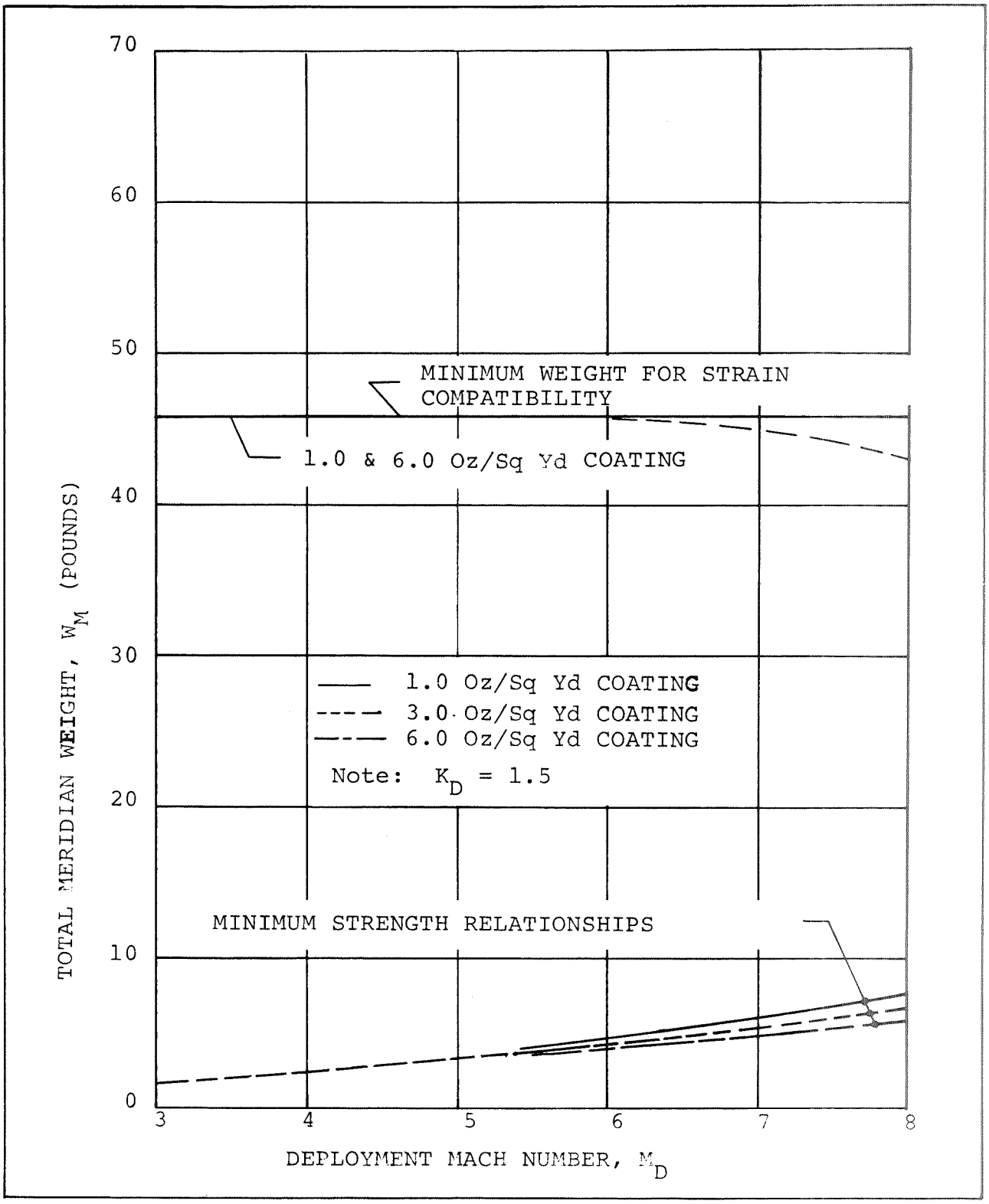

Figure 32 - Total Meridian Weight Versus Deployment Mach Number (B_E = 0.3) - Mars Atmosphere

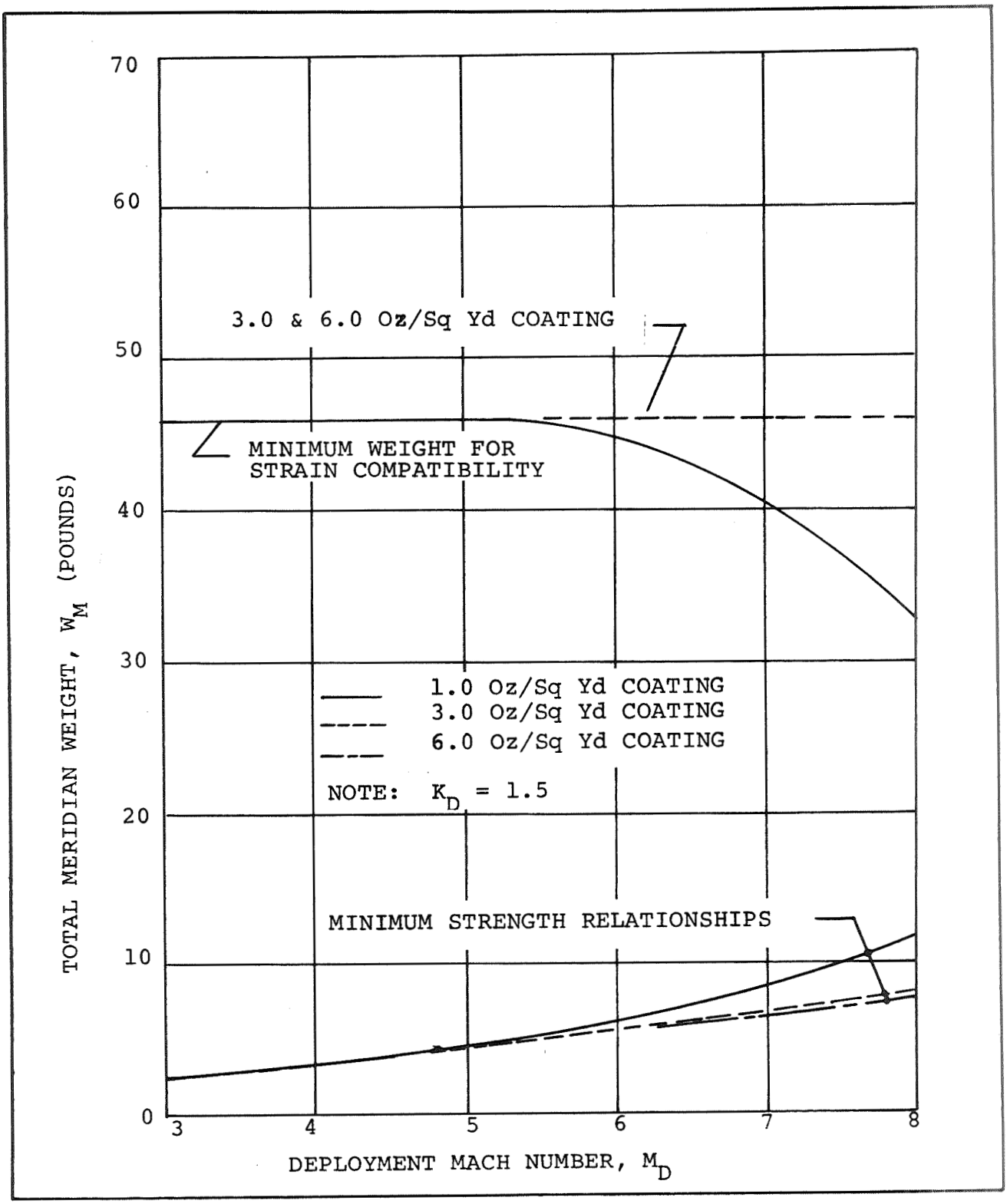

Figure 33 - Total Meridian Weight Versus Deployment Mach Number (B_E = 0.4) - Mars Atmosphere

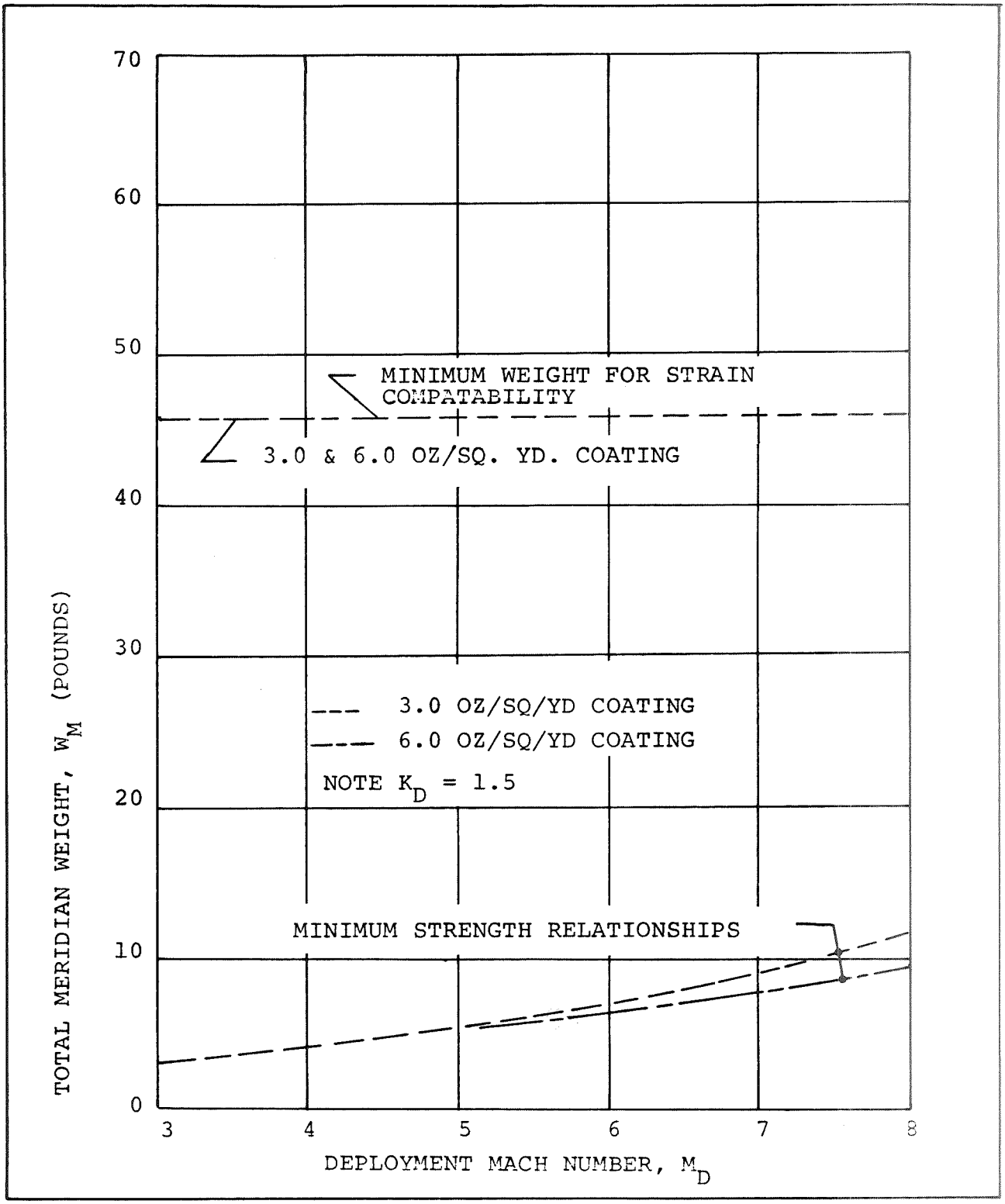

Figure 34 - Total Meridian Weight Versus Deployment Mach Number (B_E = 0.5) - Mars Atmosphere

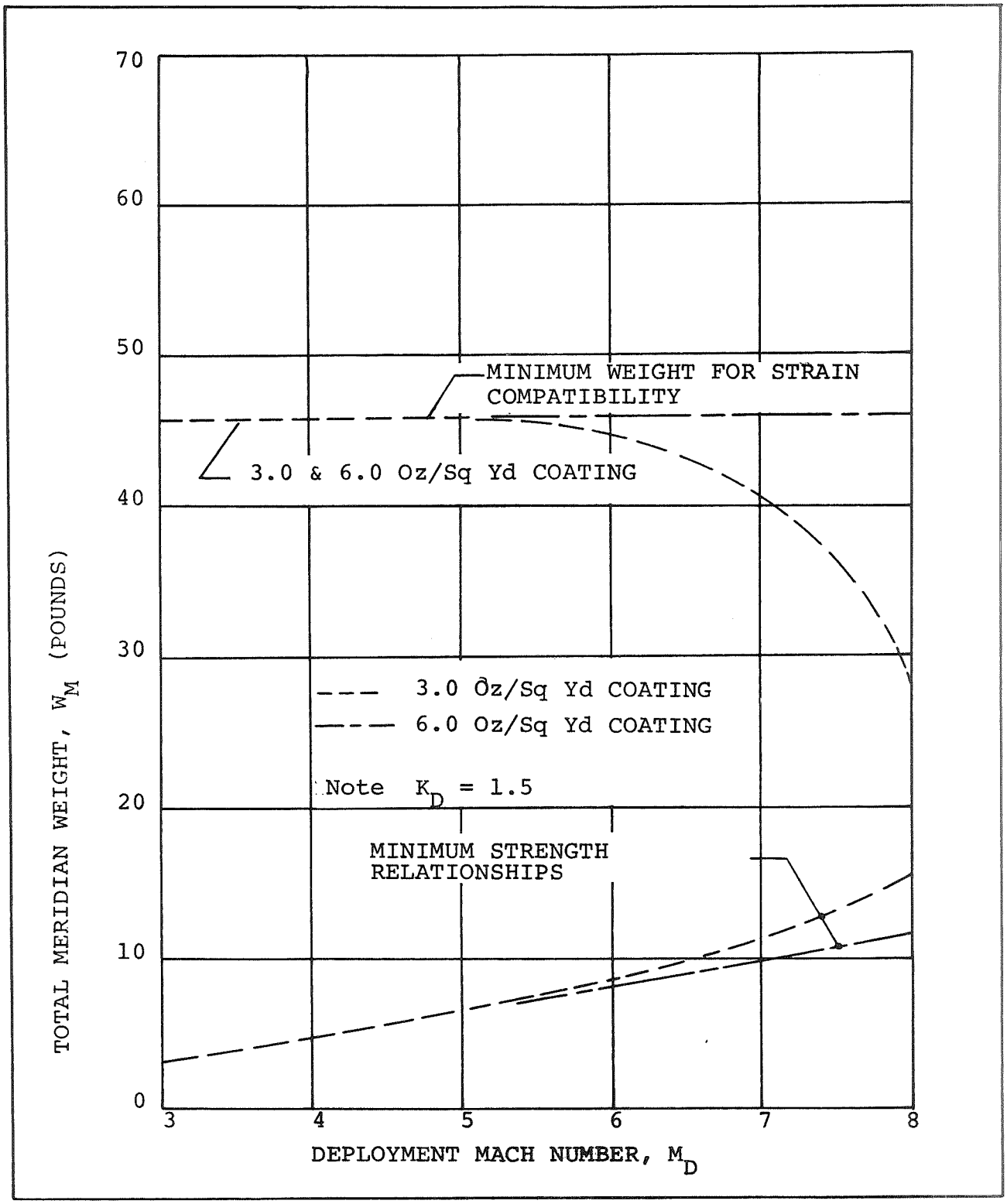

Figure 35 - Total Meridian Weight Versus Deployment Mach Number (B_E = 0.6) - Mars Atmosphere

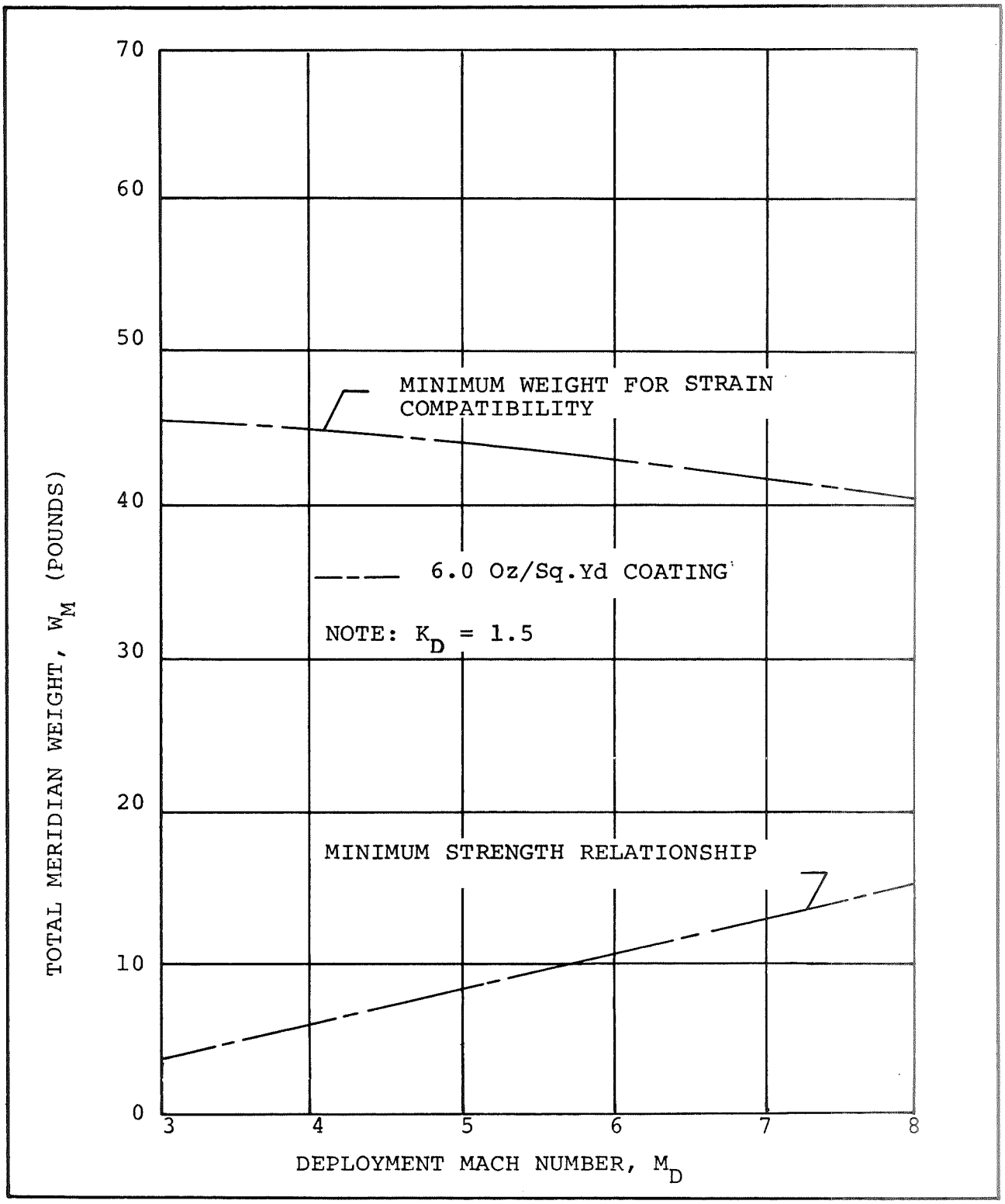

Figure 36 - Total Meridian Weight Versus Deployment Mach Number (B_E = 0.7) - Mars Atmosphere

The upper curve on the figures is the meridian weight corresponding to minimum gage fabric for which strain compatibility of the meridians and cloth is maintained. A minimum gage constraint is implicit in the isotensoid requirement of equal strain in both the fabric and meridians as noted previously. Since, this study involves Nomex fabric as well as Nomex meridians, each is assumed to have comparable load-elongation characteristics. To maintain strain compatibility with the 2.3 oz/ yd^2 Nomex the meridian strengths may be much stronger than is required from a load standpoint as is evident on Figures 35-45. However, a meridian of less strength would allow an elongation in the meridian greater than that in the fabric, resulting in a redistribution of the stresses in the meridian and cloth. The redistribution would result in a more highly stressed cloth than indicated by the isotensoid theory. The minimum AID structural weights possible, using Nomex meridians with the 2.3 oz/sq. yd. Nomex fabric are presented in Table V.

TABLE V - MINIMUM AID STRUCTURAL WEIGHTS FOR MARS ENTRY

B_E	Coating wt (oz/sq yd)	M_D	W_f (lb)	W_m (lb)	$W_f + W_m$ (lb)
0.3	1.0	3,5,8	29.7	46	75.7
0.4		3,5		46	75.7
		8		32	61.7
0.5	3.0	3,5,8	47.7	46	93.7
0.6		3,5		46	93.7
		8		28	75.7
0.7	6.0	3	74.7	46	120.7
		5		44	118.7
		8		41	115.7

IV DESIGN POINT ANALYSIS

Trajectory Analysis

Initial Deployment Condition - As noted previously, the design point analysis was conducted in order to determine the limiting state-of-the-art test point in the earth atmosphere. Two vehicle ballistic coefficients were examined for two fabric-coating combinations over the range of deployment conditions presented in Table VI.

TABLE VI - AID Deployment Points In Earth Atmosphere

Ballistic coefficient, B_E (slugs/sq ft)	Entry angle, γ (deg)	Deployment Mach number, M_D	Altitude, Z (ft)	Dynamic pressure, q_D (psf)	Entry velocity, V (fps)
0.4	-80	4.5	140,000	60	4750
0.4	-80	6.0	155,000	60	6500
0.4	-80	8.0	170,000	60	8650
0.6	-80	4.5	140,000	60	4750
0.6	-80	6.0	155,000	60	6500
0.6	-80	8.0	170,000	60	8650

The six trajectories generated from the initial conditions stated in Table VI are shown in Figures 37 through 42. The trajectory computations for each condition were terminated when a Mach number of 1.5 was reached.

Equations, Pressure Distribution, and Atmosphere - The pressure distribution and the equations used for the thermal analysis were essentially those used for analyzing the canopy in the Mars atmosphere. The exceptions are the atmosphere (which in the case was the 1962 Standard Earth atmosphere) and the viscosity equation (which was basically Sutherland's equation for air rather than carbon dioxide). The quanities used to evaluate the heat flux relations for the design point analysis are summarized in Table VII.

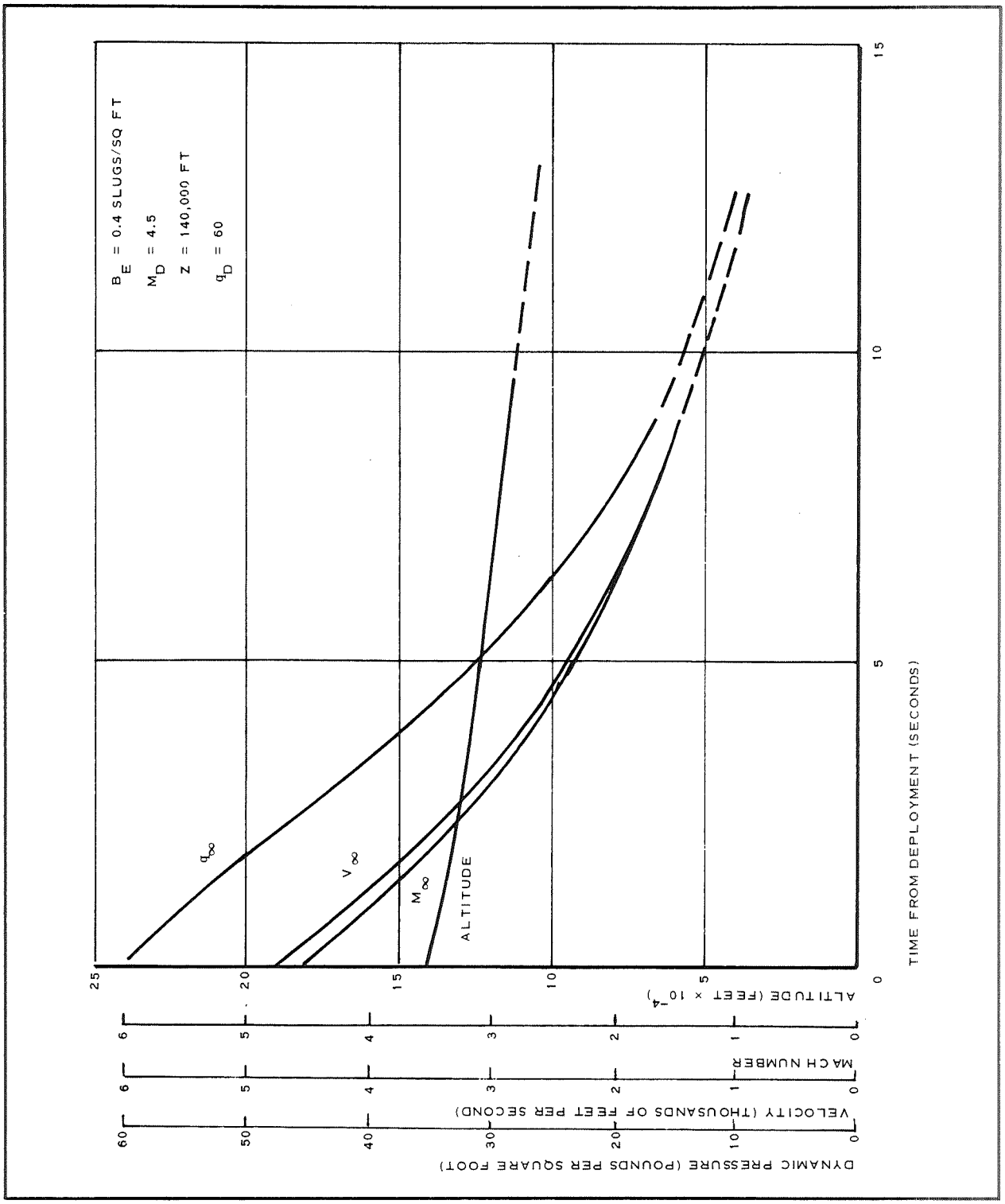

Figure 37 - Earth Trajectory Data (Condition 1)

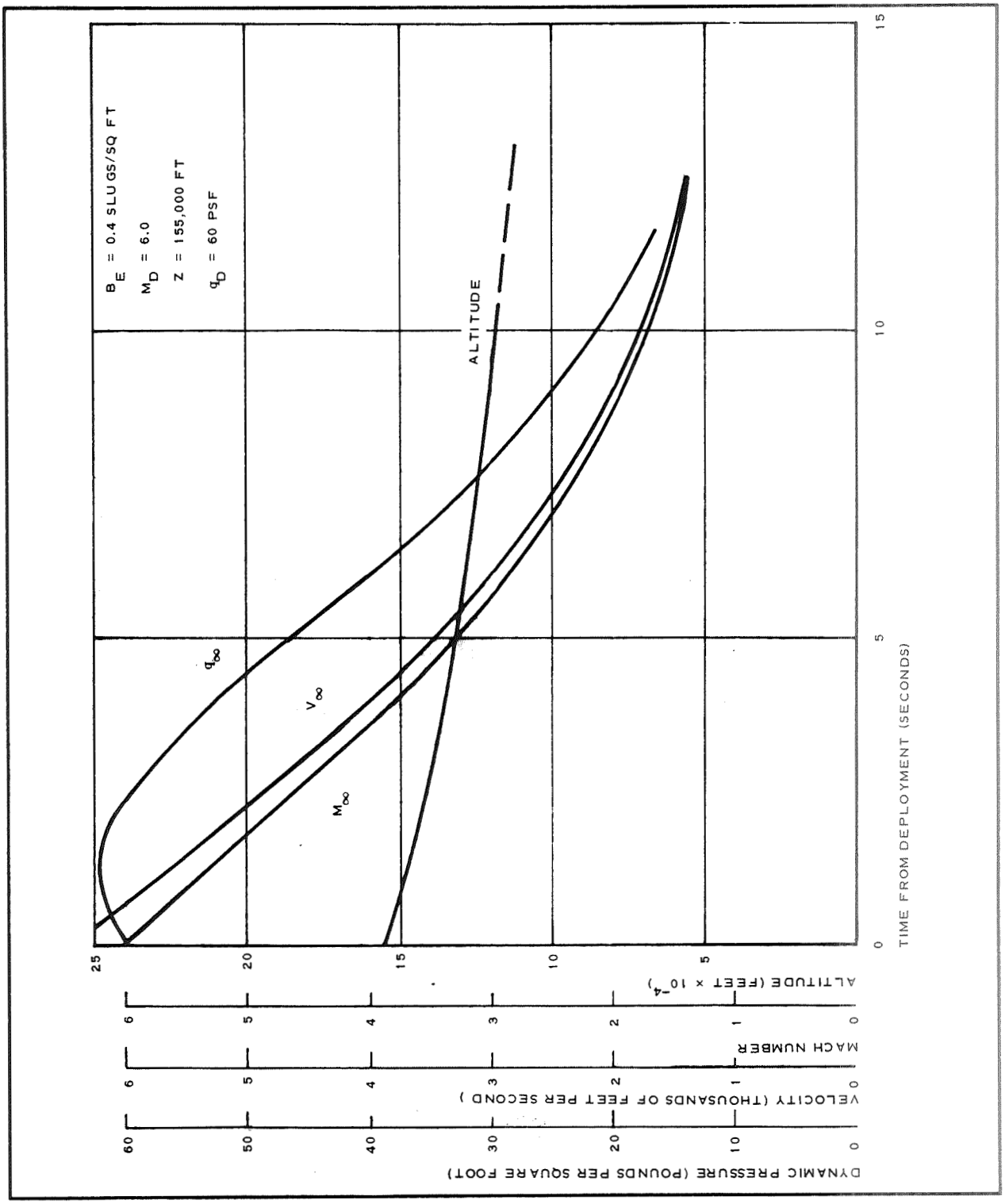

Figure 38 - Trajectory Data (Condition 2)

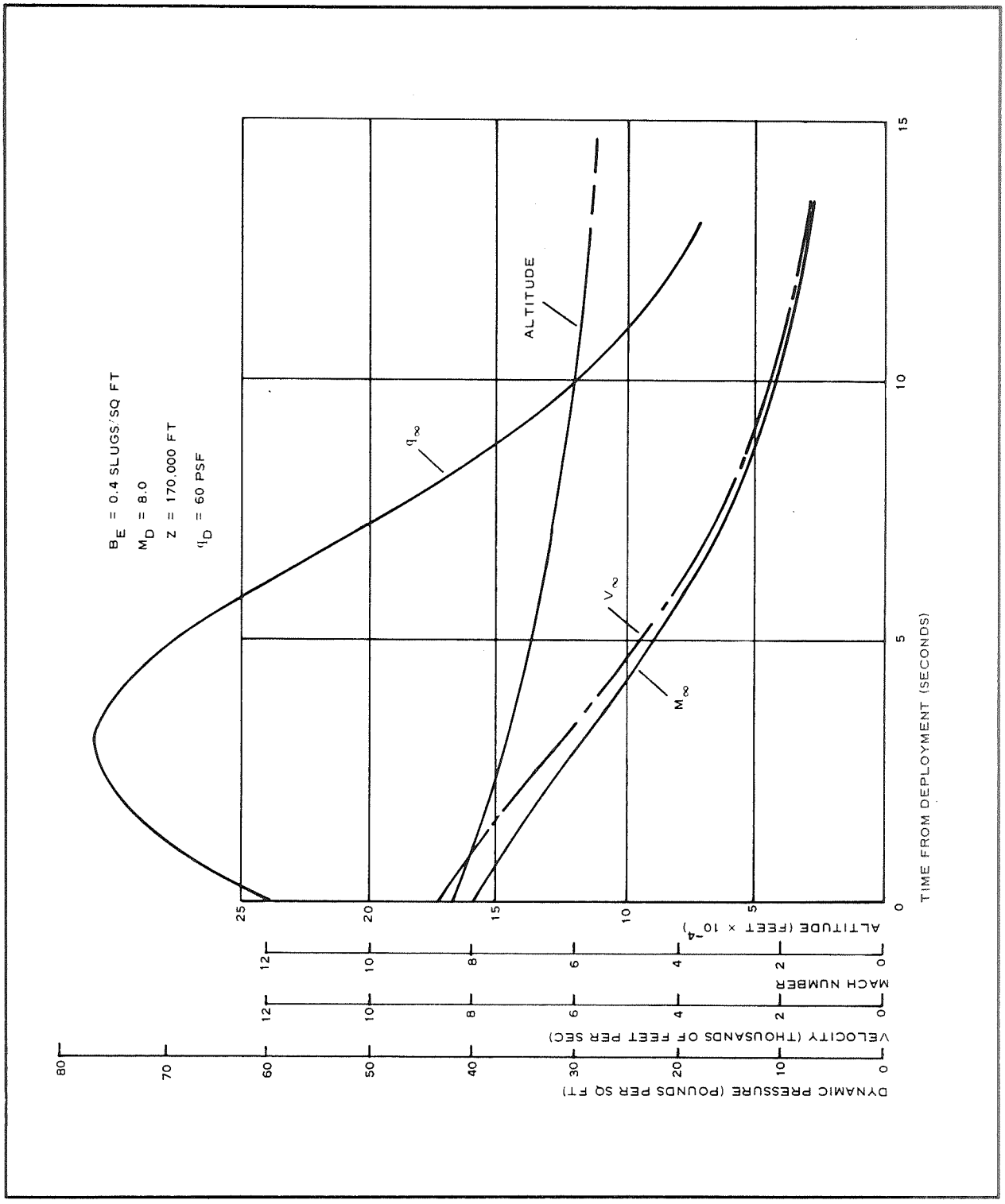

Figure 39 - Trajectory Data (Condition 3)

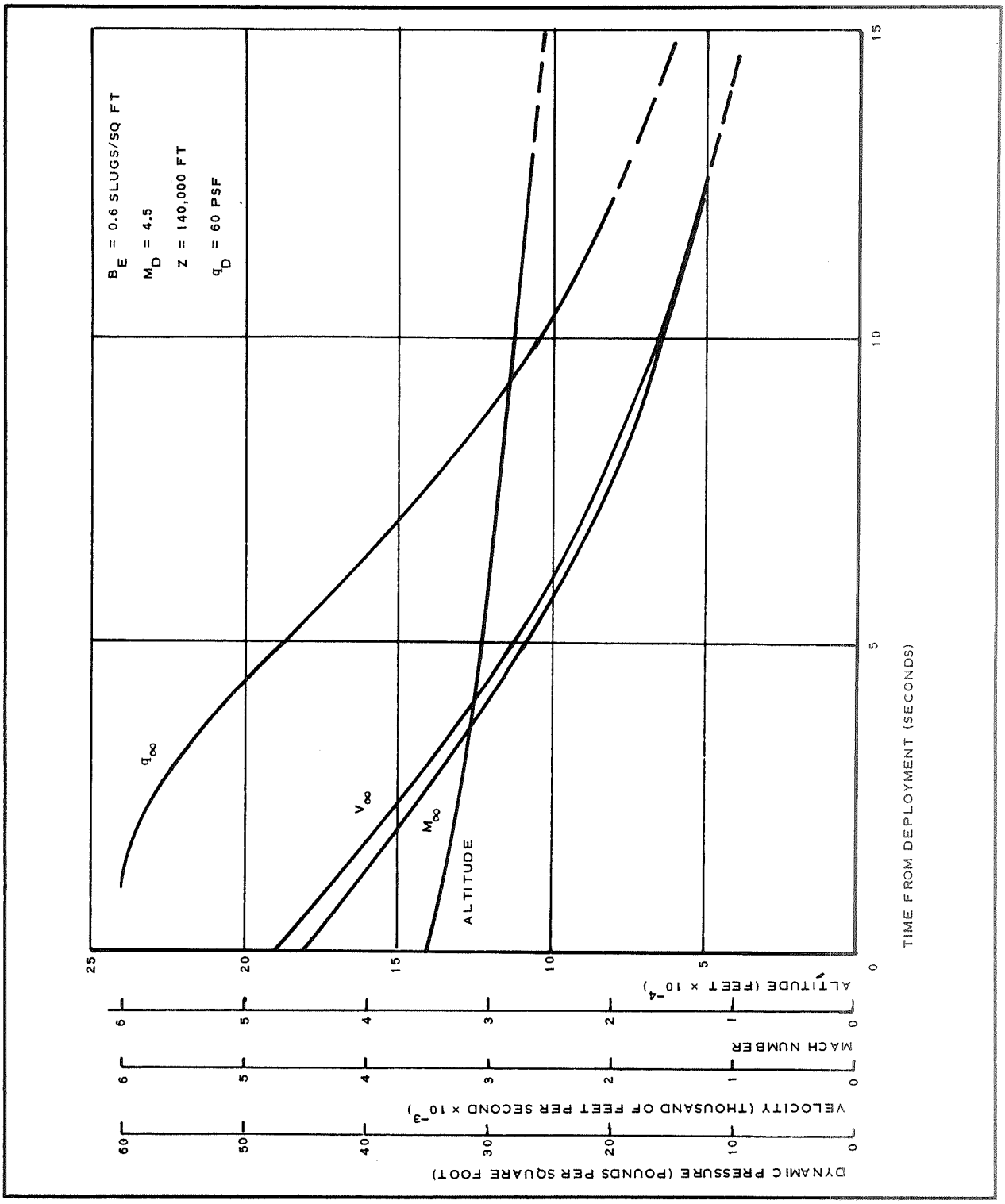

Figure 40 - Trajectory Data (Condition 4)

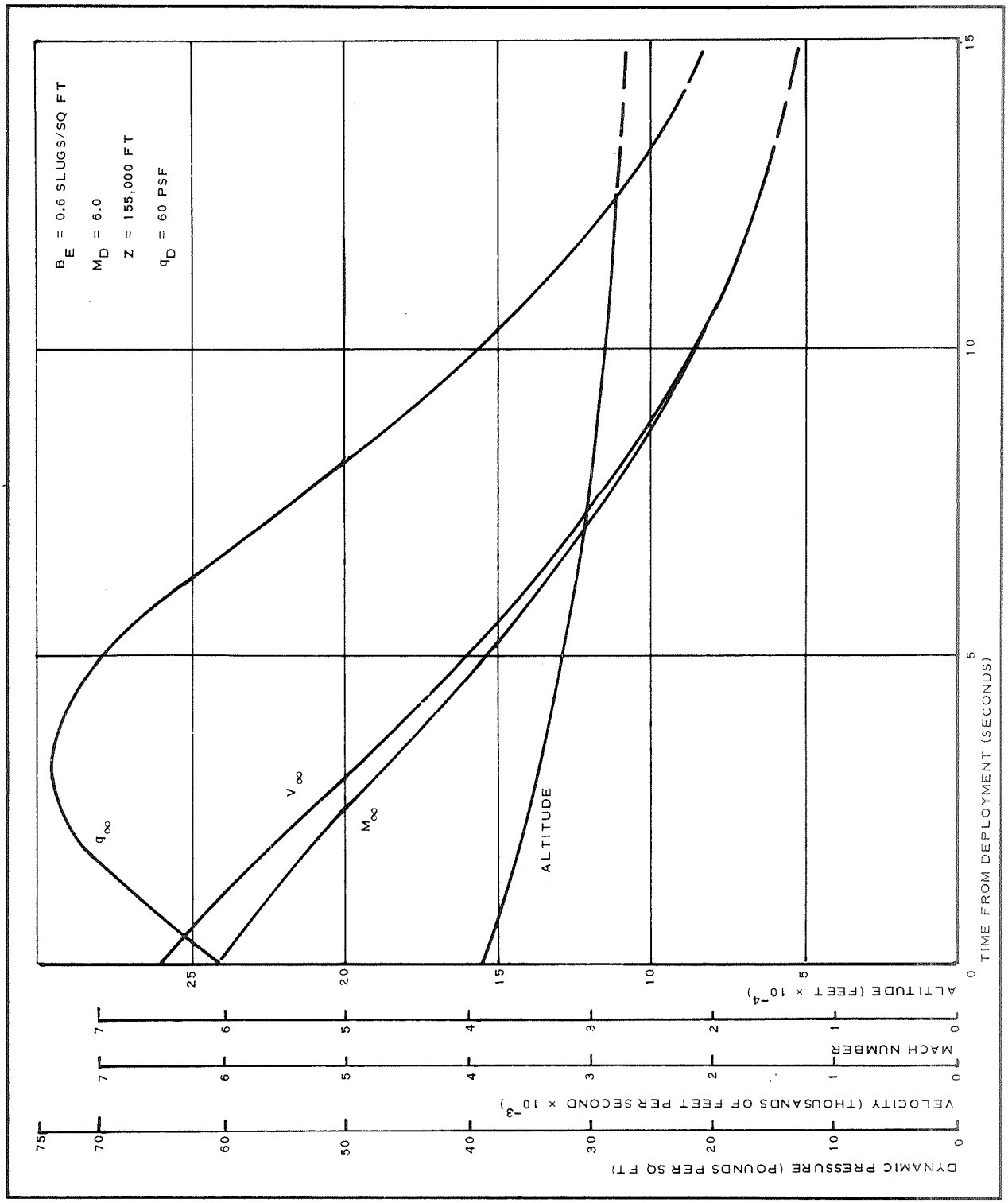

Figure 41 - Trajectory Data (Condition 5)

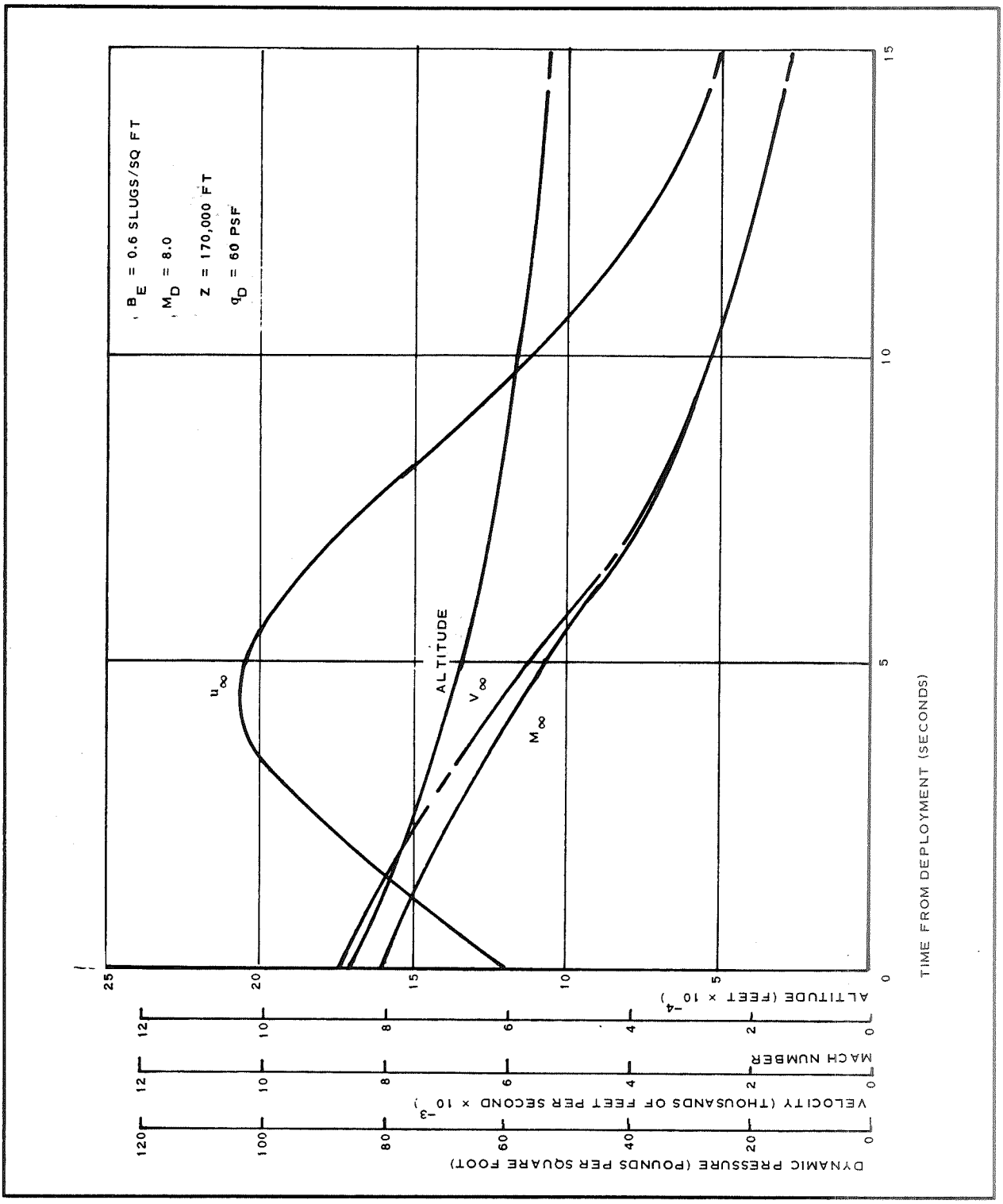

Figure 42- Trajectory Data (Condition 6)

TABLE VII - INPUT PROPERTIES TO HEAT FLUX EQUATIONS - EARTH ATMOSPHERE (DESIGN POINT STUDY)

Property	Symbol	Value
Specific heat	C_p	0.24 Btu/lb-F
Joules constant	J	778 ft-lb/Btu
Gravitational constant	g_o	32.2 ft/sec^2
Molecular weight	m	29 lb/lb-mole
Ratio of specific heats	γ	1.4
Constants for Sutherland's viscosity equation	C_1	2.27×10^{-8}
	C_2	198.6

Thermodynamic Analysis

Material Configurations - Two different material configurations were used for the canopy. The first configuration represents a minimum weight configuration, that of a Nomex weight of 2.3 oz/sq. yd. and a Viton coating weight of 1.0 oz/sq. yd. distributed equally on both sides of the Nomex cloth. The second material configuration consisted of the same Nomex cloth; however, the outside coating was increased to 4 oz/sq. yd. while the inside coating was raised to 2 oz/sq. yd.

Nomex Temperatures - Typical temperature versus time histories of the Nomex fabric are shown in Figures 43 through 45. These cases were selected for presentation because they represent the limiting cases for each set of deployment conditions considered.

The temperature history of the canopy for a deployment Mach number of 4.5, a B_E = 0.4 slugs/sq. ft., and the minimum weight fabric-coating combination is presented in Figure 43. The temperature at station S_1 is sgnificantly lower than that at S_2 and S_3 due to the existance of a laminar boundary layer at S_1.

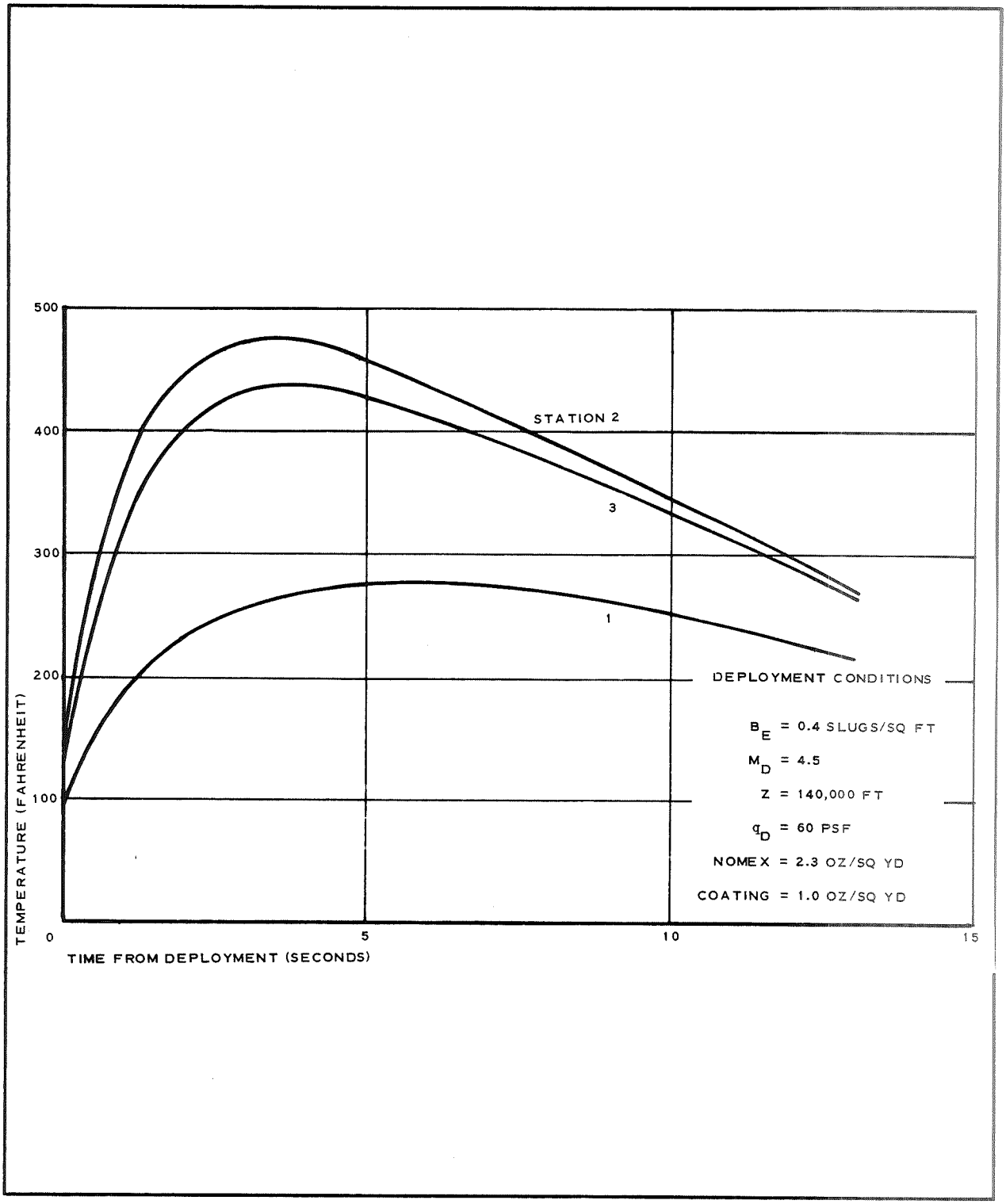

Figure 43 - Temperature versus Time from Deployment (Viton = 1 Oz/Sq Yd and B_E = 0.4 Slugs/Sq Ft)

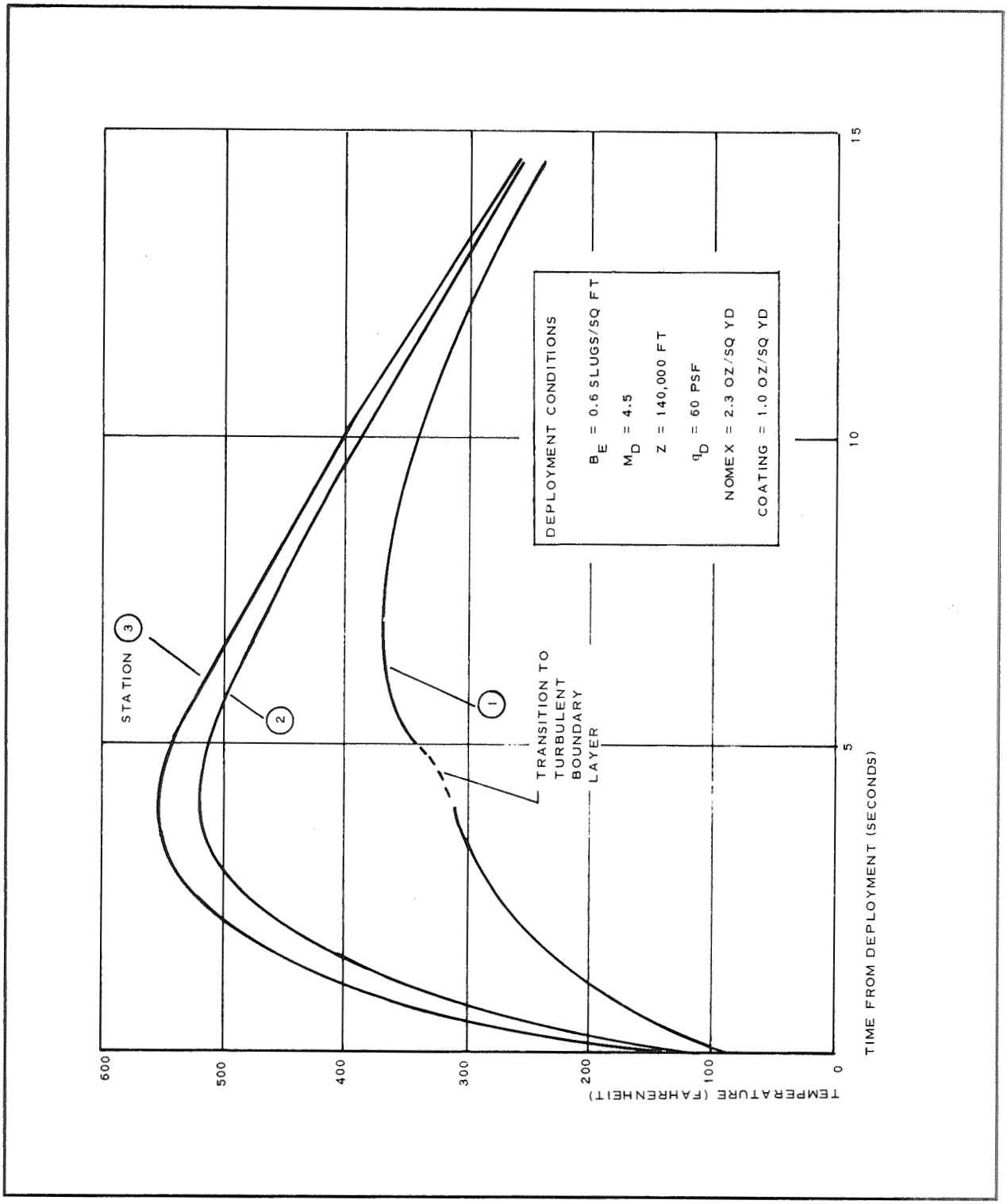

Figure 44 - Temperature versus Time from Deployment (Viton = 1 Oz/Sq Yd and B_E = 0.6 Slugs/Sq Ft)

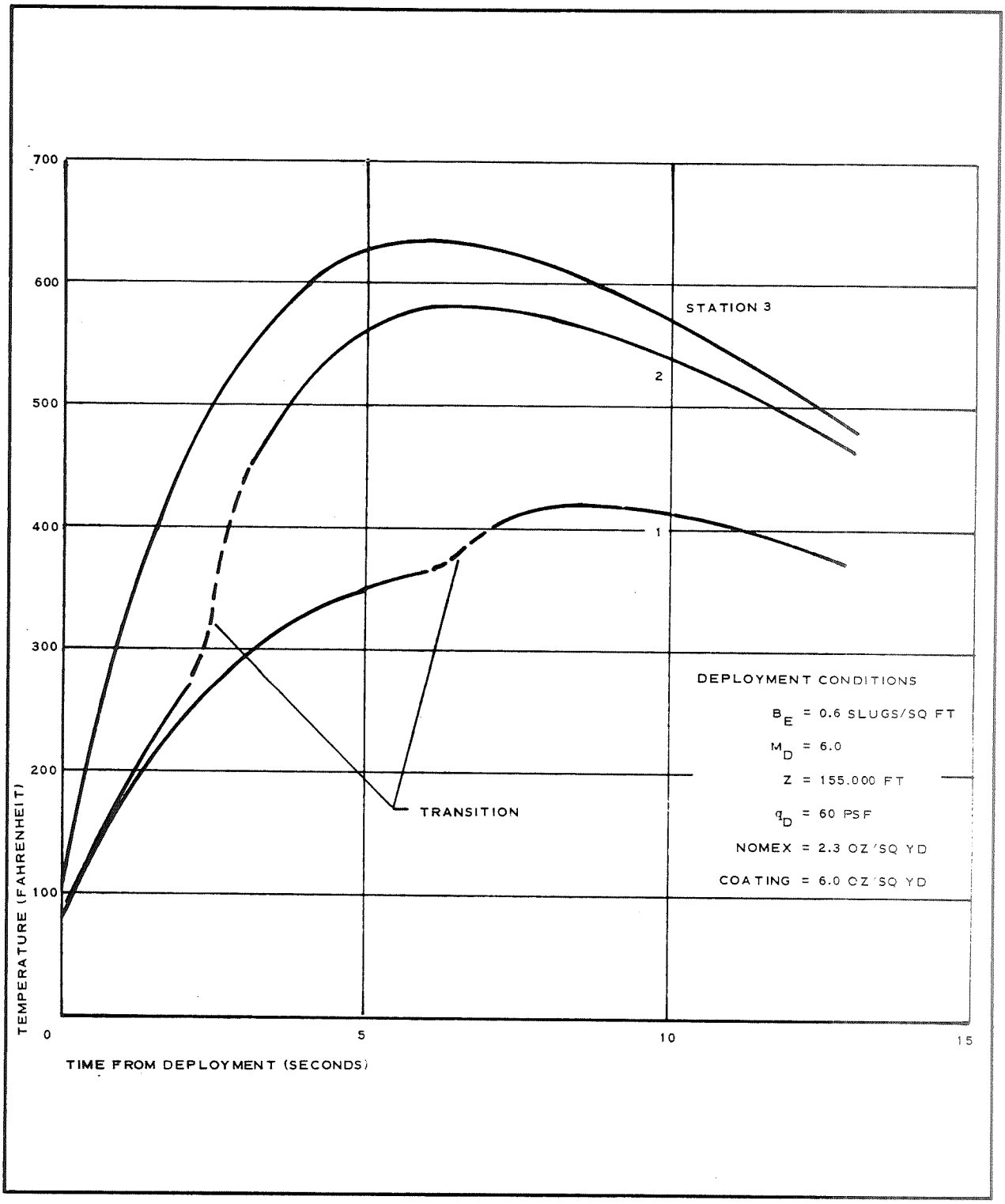

Figure 45 - Temperature versus Time from Deployment (Viton = 6 Oz/Sq Yd and B_E = 0.6 Slugs/Sq Ft)

Figure 44 indicates that for M_D = 4.5 and B = 0.6 slugs/sq. ft. the temperature is a maximum at station S_3. The temperature at station S_1 reflects initial heating rates resulting from a laminar boundary layer which after 5 seconds transitions to a turbulent layer.

A more drastic effect of boundary layer transition and the resulting heating rates on the canopy fabric is shown in Figure 45. Stations S_1 and S_2 are initially subjected to heating rates from a laminar boundary layer, which then transitions to a turbulent boundary layer.

The maximum Nomex temperatures reached for the deployment conditions of Table VI and the two material configurations are presented in Figure 46. If it is assumed that the limiting working temperature of Nomex is 600 F, then the maximum deployment Mach number is about 5.0 for a vehicle ballistic coefficient of 0.4 and a Mach number of about 4.65 for an entry vehicle ballistic coefficient of 0.6. Both of these conditions consider only the 3.3 oz/ sq. yd. canopy material. The deployment Mach number range is increased to M_D = 6.7 and M_D = 5.8 for ballistic coefficients of 0.4 and 0.6, respectively, when the coating weight is increased to 6.0 oz/sq yd.

Discussion of Alternatives - Several alternatives to increasing the coating weight are available. For example, the flight path angle can be decreased to reduce the magnitude of the heat flux rates, but the time of heating will be increased. A decrease in deployment dynamic pressure at the same deployment Mach numbers would in effect decrease the magnitude of the heating rates through an increase in the deployment altitude. Similarly, combination changes in flight path angle and dynamic pressure in the same directions discussed above would result in lowering the heating rates.

Structural Weight Determination - The structural weight equations previously derived for the parametric study apply here to the specified design point conditions. The equation for the total fabric weight that includes Nomex cloth plus Viton coating is from Equations 23 and 24:

$$w_f = 1462.3\ K_D\left(\frac{q}{k_f}\right) + W_c \qquad (30)$$

where

W_{c_1} = 8.99 lb for a unit coating weight of 1 oz/sq. yd.,

W_{c_6} = 53.97 lb for a unit coating weight of 6 oz/sq. yd

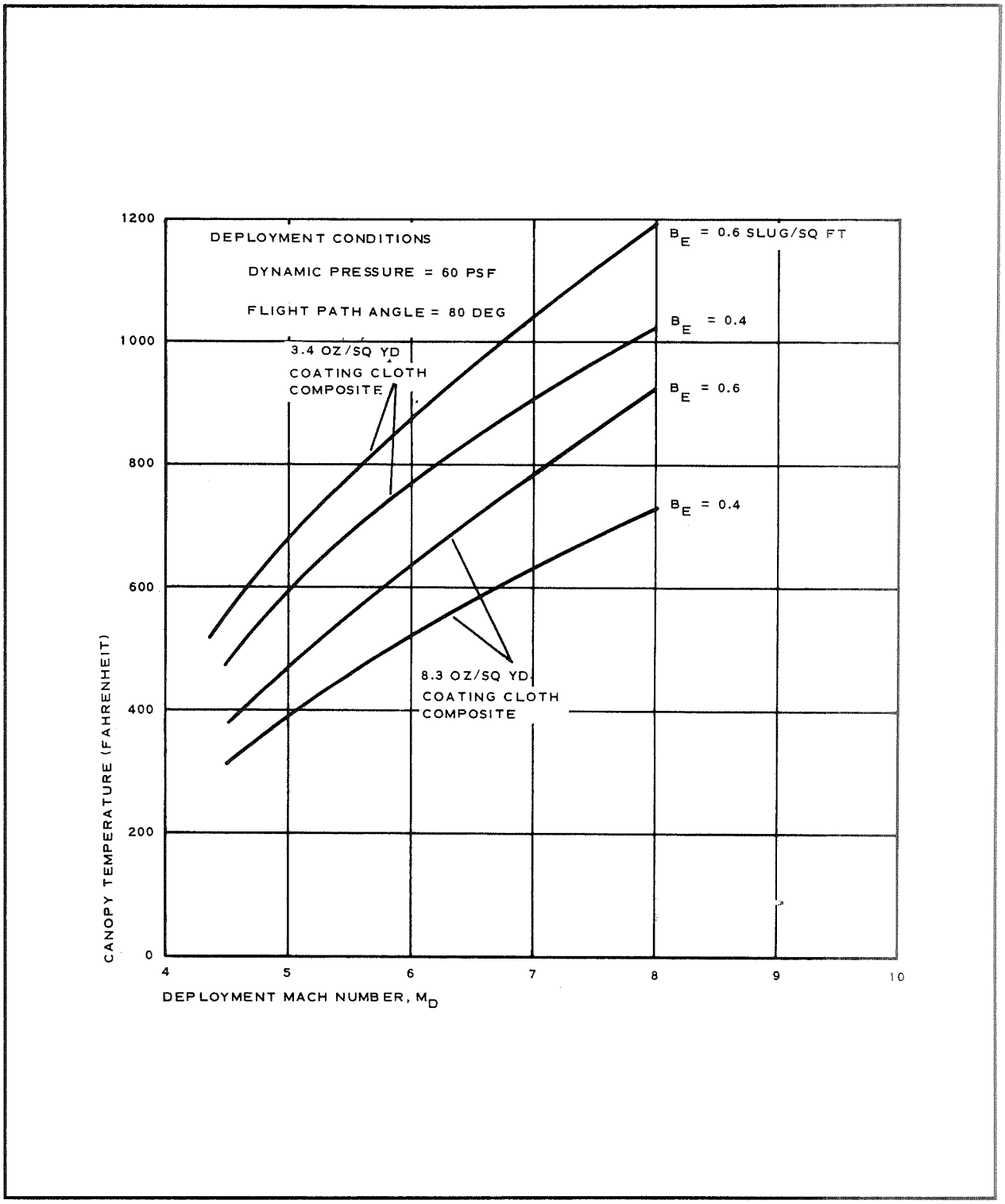

Figure 46 - Maximum Nomex Temperature versus Mach Number - Earth Atmosphere (Viton 1.C and 6.0 oz/ sq yd)

For the deployment conditions of Figure 46, for which the fabric temperature remains below 600 F, the maximum value of $(q/k_f)K_D$ for a design factors of 3.0 is less than 0.01415 psf. Therefore, the 2.3 oz/ sq. yd. Nomex provides sufficient strength for all cases resulting in temperatures below the working temperature limit.

The corresponding total fabric weights for this cloth and the above two coatings then are given by Equation 30 as,

$$W_{mf_1} = 20.69 + 8.99 = 29.7 \text{ lb (for 1 oz/sq. yd. coating)}, \quad (31)$$

and

$$W_{mf_6} = 20.69 + 53.97 = 74.7 \text{ lb (for 6 oz/sq. yd. coating)}, \quad (32)$$

The total meridian weights also have been defined for the design point conditions using the previously derived equation,

$$W_m = 5811\ K_D \left(\frac{q}{k_c}\right)_{max} \quad (33)$$

This equation was used to generate the meridian weight curves of Figures 47 and 48 over the deployment Mach number range from $M_D = 3$ to the Mach numbers for which the cutoff temperature of 600F occurred.

Also shown on each figure is the meridian weight curves for which strain compatibility of meridians and cloth is maintained. Thus, the upper curve is based on meridian stiffness requirements whereas the lower curves are based on strength requirements. Assuming strain compatibility is required, the minimum AID weights possible, using Nomex meridians and the 2.3 oz/sq. yd. Nomex fabric, for the deployment conditions of Table VI are presented in Table VIII.

TABLE VIII - MINIMUM AID STRUCTURAL WEIGHTS FOR DEPLOYMENT IN EARTH ATMOSPHERE*

B (Slugs/sq ft)	M_D	γ (deg)	Z_D (ft)	Coating Weight (oz/yd)	W_f (lb)	W_m (lb)	$W_f + W_m$ (lb)
0.4	4.5	-80	140,000	1	29.7	44	73.7
0.4	6.0	-90	155,000	6	74.7	42	116.7
0.6	4.5	-80	140,000	1	29.7	38	67.7

*Deployment dynamic pressure is 60 psf

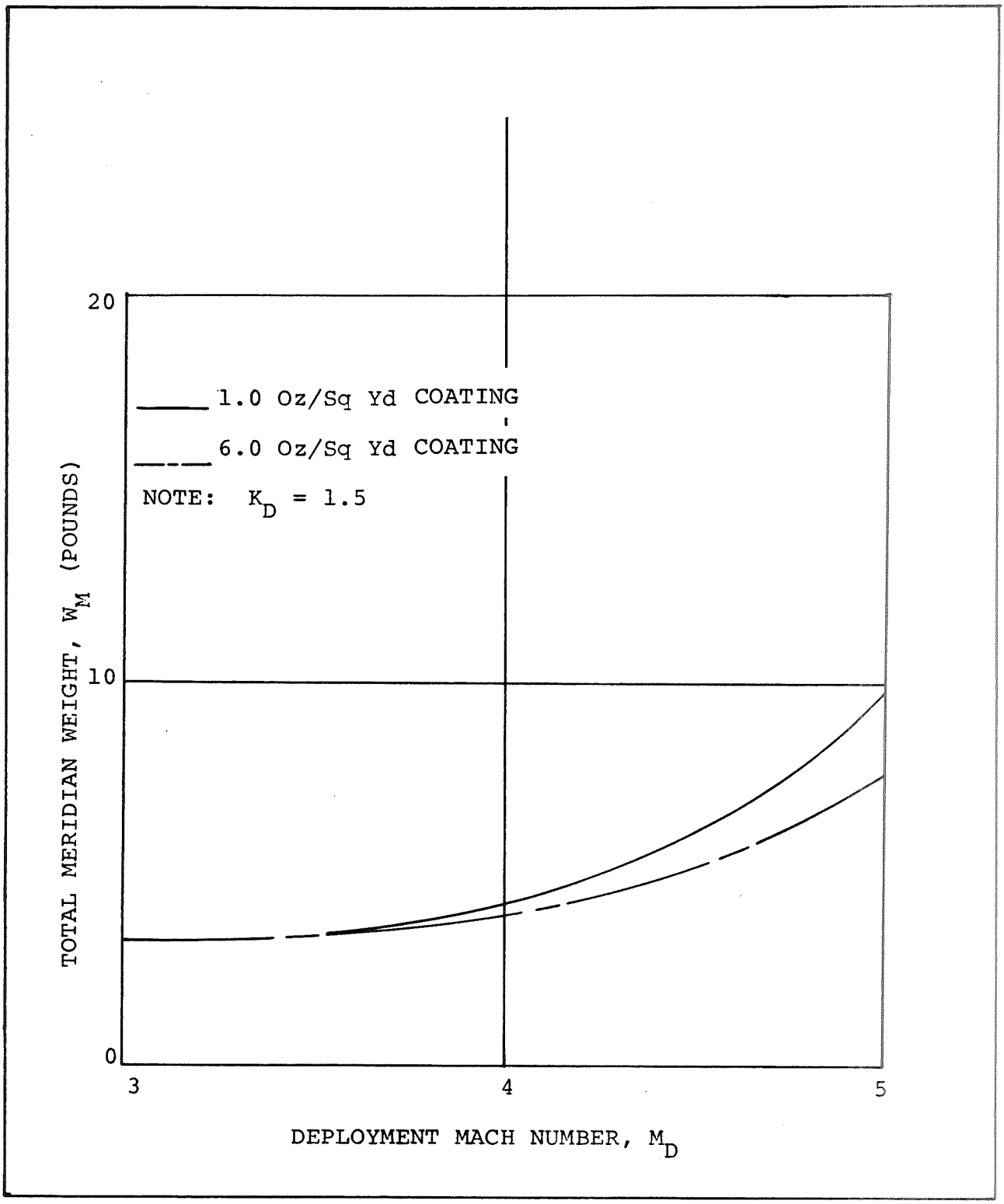

Figure 47 - Total Meridian Weight Versus Deployment Mach Number (B_E = 0.4) - Earth Atmosphere

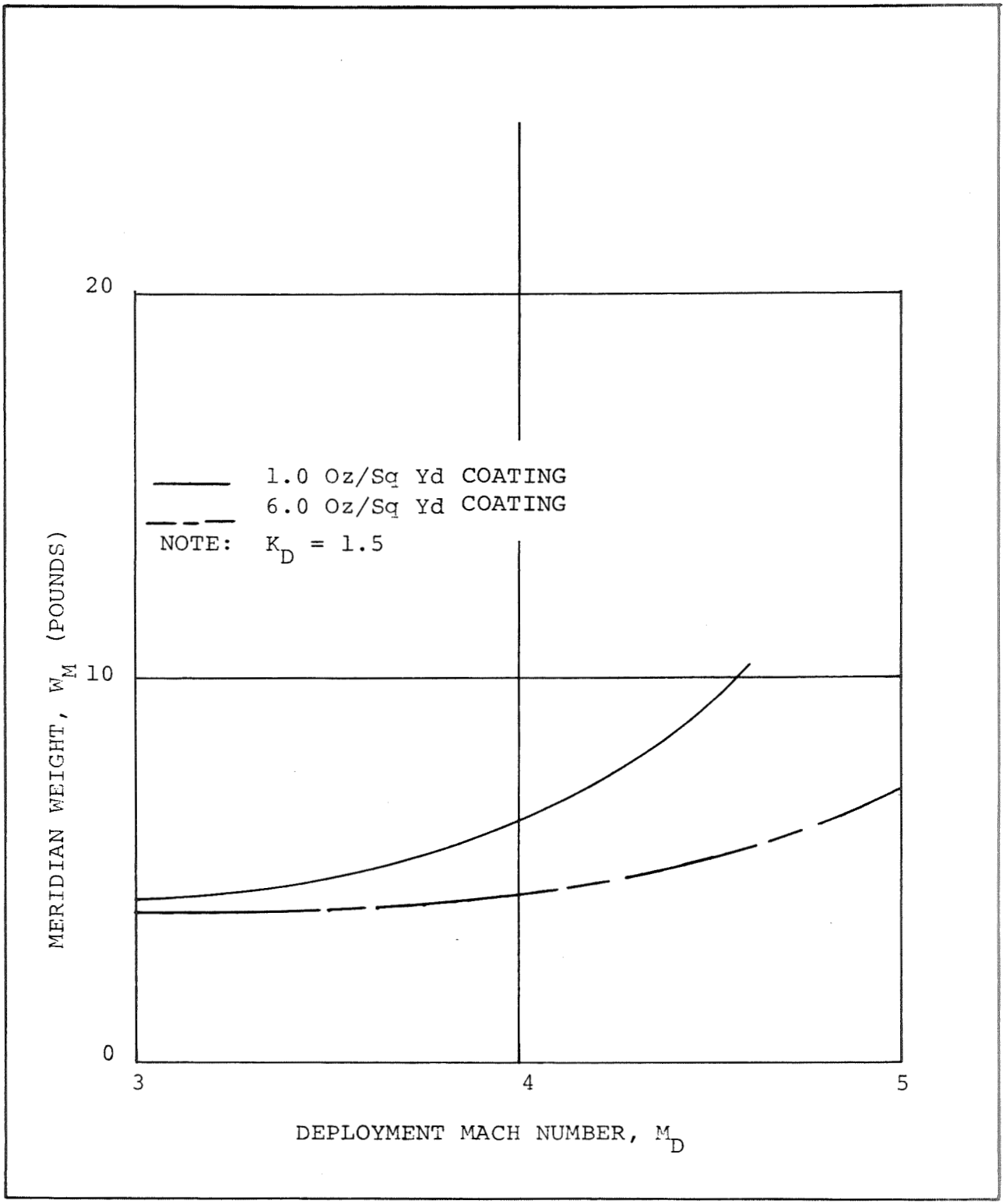

Figure 48 - Total Meridian Weight Versus Deployment Mach Number (B_E = 0.6) - Earth Atmosphere

V. CONCLUSIONS

Thermal and stress analysis have been conducted for an AID deployed in both the Mars and Earth atmospheres. The following conclusions can be drawn from these analysis:

1. Deployment of the AID in the Mars Min $H\rho_s$ atmosphere is feasible using existing technology over the range of parameters considered (i.e., $0.3 \leq B_E \leq 0.7$ slugs/sq. ft. and $3.0 \leq M_D \leq 8.0$).

2. A minimum coating weight (1.0 oz/sq. yd.) needed to provide an air tight fabric structure was shown to provide thermal protection for the fabric over the entire range of entry ballistic coefficients considered for deployment Mach numbers up to 6.7. A coating of 6.0 oz/sq. yd. was found to provide thermal protection over the entire range of parameters considered.

3. For 6 oz/yd^2 coating deployment of the AID in the Earth atmosphere is feasible for $B_E = .4$, $q_D = 60$ psf and M_D up to 6.7; and for $B_E = .6$, $q_D = 60$ psf and M_D up to 5.8.

4. The assumption of equal load-elongation characteristics of the fabric and meridians and the requirement of strain compatibility may result in meridian weights an order of magnitude heavier, for certain cases of the Mars entry study, than would be dictated on a strength basis. The actual allowable strain relationship between bias-layed fabric and meridian tapes must be determined from laboratory tests.

APPENDIX A

MINIMUM $H_{\rho,s}$ MODEL ATMOSPHERES

OF MARS

The data on the following pages for minimum scale height atmosphere were taken from Mars Engineering Model M75-125-0 (dated 13 March 1970). This model was prepared by the Viking Project Office of Langley Research Center.

ALTITUDE, KM	TEMP., DEG K	PRESSURE, MB	MASS DENSITY, GM/CC	NUMBER DENSITY, 1/CC	MOLECULAR MASS, KG/KG-MOLE	DENSITY SCALE HEIGHT, KM	PRESSURE SCALE HEIGHT, KM	SPECIFIC HEAT, C(P)/R	SPECIFIC HEAT RATIO	SOUND SPEED, M/SEC	COEFFICIENT OF VISCOSITY, KG/M SEC	THERMAL CONDUCTIVITY, J/M-SEC-DEG K
-10.0	219.6	1.08E+01	2.60E-05	3.56E+17	44.0	13.75	11.09	4.01	1.33	235	1.11E-05	1.20E-02
-9.0	215.6	9.84E+00	2.42E-05	3.31E+17	44.0	13.51	10.89	3.98	1.34	233	1.09E-05	1.17E-02
-8.0	211.7	8.97E+00	2.24E-05	3.07E+17	44.0	13.27	10.70	3.96	1.34	231	1.07E-05	1.15E-02
-7.0	207.7	8.16E+00	2.08E-05	2.85E+17	44.0	13.04	10.51	3.94	1.34	229	1.05E-05	1.12E-02
-6.0	203.7	7.42E+00	1.93E-05	2.64E+17	44.0	12.80	10.31	3.91	1.34	227	1.03E-05	1.09E-02
-5.0	199.8	6.73E+00	1.78E-05	2.44E+17	44.0	12.56	10.12	3.89	1.35	225	1.01E-05	1.07E-02
-4.0	195.8	6.09E+00	1.64E-05	2.25E+17	44.0	12.32	9.92	3.87	1.35	223	9.89E-06	1.04E-02
-3.0	191.9	5.50E+00	1.52E-05	2.08E+17	44.0	12.09	9.73	3.85	1.35	221	9.69E-06	1.01E-02
-2.0	187.9	4.96E+00	1.40E-05	1.91E+17	44.0	11.85	9.53	3.82	1.35	219	9.48E-06	9.85E-03
-1.0	184.0	4.46E+00	1.28E-05	1.76E+17	44.0	11.61	9.34	3.80	1.36	217	9.28E-06	9.59E-03
0.0	180.0	4.00E+00	1.18E-05	1.61E+17	44.0	11.37	9.14	3.78	1.36	215	9.08E-06	9.33E-03
1.0	176.0	3.58E+00	1.08E-05	1.47E+17	44.0	11.13	8.95	3.76	1.36	213	8.88E-06	9.08E-03
2.0	172.1	3.20E+00	9.84E-06	1.35E+17	44.0	10.89	8.75	3.74	1.37	211	8.67E-06	8.83E-03
3.0	168.1	2.85E+00	8.97E-06	1.23E+17	44.0	10.65	8.55	3.72	1.37	208	8.47E-06	8.58E-03
4.0	164.2	2.53E+00	8.16E-06	1.12E+17	44.0	10.40	8.36	3.70	1.37	206	8.27E-06	8.33E-03
5.0	160.2	2.24E+00	7.41E-06	1.01E+17	44.0	10.16	8.16	3.68	1.37	204	8.07E-06	8.09E-03
6.0	156.2	1.98E+00	6.71E-06	9.19E+16	44.0	9.92	7.96	3.66	1.38	202	7.86E-06	7.85E-03
7.0	152.3	1.74E+00	6.06E-06	8.30E+16	44.0	9.68	7.77	3.65	1.38	199	7.66E-06	7.62E-03
8.0	148.3	1.53E+00	5.46E-06	7.48E+16	44.0	9.43	7.57	3.63	1.38	197	7.45E-06	7.39E-03
9.0	144.4	1.34E+00	4.91E-06	6.72E+16	44.0	9.19	7.37	3.62	1.38	194	7.25E-06	7.16E-03
10.0	140.4	1.17E+00	4.40E-06	6.03E+16	44.0	8.95	7.17	3.60	1.38	192	7.05E-06	6.93E-03
11.0	136.5	1.01E+00	3.93E-06	5.38E+16	44.0	8.70	6.98	3.59	1.39	189	6.85E-06	6.71E-03
12.0	132.5	8.77E-01	3.50E-06	4.79E+16	44.0	8.46	6.78	3.58	1.39	186	6.65E-06	6.49E-03
13.0	128.5	7.55E-01	3.11E-06	4.25E+16	44.0	8.21	6.58	3.56	1.39	184	6.45E-06	6.28E-03
14.0	124.6	6.47E-01	2.75E-06	3.76E+16	44.0	7.97	6.38	3.55	1.39	181	6.24E-06	6.07E-03
15.0	120.6	5.52E-01	2.42E-06	3.31E+16	44.0	7.72	6.18	3.54	1.39	178	6.04E-06	5.86E-03
16.0	116.7	4.68E-01	2.12E-06	2.91E+16	44.0	7.47	5.98	3.54	1.39	175	5.84E-06	5.65E-03
17.0	112.7	3.95E-01	1.85E-06	2.54E+16	44.0	7.23	5.78	3.53	1.40	172	5.65E-06	5.45E-03
18.0	108.7	3.31E-01	1.61E-06	2.21E+16	44.0	6.98	5.58	3.52	1.40	169	5.45E-06	5.25E-03
19.0	104.8	2.76E-01	1.39E-06	1.91E+16	44.0	6.73	5.38	3.52	1.40	166	5.25E-06	5.06E-03
20.0	100.8	2.28E-01	1.20E-06	1.64E+16	44.0	6.48	5.18	3.51	1.40	163	5.06E-06	4.87E-03
21.0	96.9	1.88E-01	1.02E-06	1.40E+16	44.0	6.23	4.98	3.51	1.40	160	4.87E-06	4.68E-03
22.0	92.9	1.53E-01	8.70E-07	1.19E+16	44.0	5.98	4.78	3.51	1.40	157	4.68E-06	4.49E-03
23.0	89.0	1.23E-01	7.34E-07	1.01E+16	44.0	5.73	4.58	3.51	1.40	153	4.49E-06	4.31E-03
24.0	85.0	9.87E-02	6.15E-07	8.41E+15	44.0	4.86	4.38	3.50	1.40	150	4.30E-06	4.12E-03
25.0	85.0	7.86E-02	4.89E-07	6.70E+15	44.0	4.37	4.38	3.50	1.40	150	4.30E-06	4.12E-03
26.0	85.0	6.25E-02	3.89E-07	5.33E+15	44.0	4.37	4.38	3.50	1.40	150	4.30E-06	4.12E-03
27.0	85.0	4.98E-02	3.10E-07	4.24E+15	44.0	4.38	4.39	3.50	1.40	150	4.30E-06	4.12E-03
28.0	85.0	3.96E-02	2.47E-07	3.38E+15	44.0	4.38	4.39	3.50	1.40	150	4.30E-06	4.12E-03
29.0	85.0	3.16E-02	1.96E-07	2.69E+15	44.0	4.38	4.39	3.50	1.40	150	4.30E-06	4.12E-03
30.0	85.0	2.51E-02	1.56E-07	2.14E+15	44.0	4.38	4.39	3.50	1.40	150	4.30E-06	4.12E-03

ALTITUDE, KM	TEMP., DEG K	PRESSURE, MB	MASS DENSITY, GM/CC	NUMBER DENSITY, 1/CC	MOLECULAR MASS, KG/KG-MOLE	DENSITY SCALE HEIGHT, KM	PRESSURE SCALE HEIGHT, KM	SPECIFIC HEAT, C(P)/R	SPECIFIC HEAT RATIO	SOUND SPEED, M/SEC	COEFFICIENT OF VISCOSITY, KG/M SEC	THERMAL CONDUCTIVITY, J/M-SEC-DEG K
31.0	85.0	2.00E-02	1.25E-07	1.71E+15	44.0	4.39	4.40	3.50	1.40	150	4.30E-06	4.12E-03
32.0	85.0	1.59E-02	9.93E-08	1.36E+15	44.0	4.39	4.40	3.50	1.40	150	4.30E-06	4.12E-03
33.0	85.0	1.27E-02	7.91E-08	1.08E+15	44.0	4.39	4.40	3.50	1.40	150	4.30E-06	4.12E-03
34.0	85.0	1.01E-02	6.30E-08	8.63E+14	44.0	4.39	4.40	3.50	1.40	150	4.30E-06	4.12E-03
35.0	85.0	8.07E-03	5.02E-08	6.88E+14	44.0	4.40	4.41	3.50	1.40	150	4.30E-06	4.12E-03
36.0	85.0	6.43E-03	4.00E-08	5.48E+14	44.0	4.40	4.41	3.50	1.40	150	4.30E-06	4.12E-03
37.0	85.0	5.13E-03	3.19E-08	4.37E+14	44.0	4.40	4.41	3.50	1.40	150	4.30E-06	4.12E-03
38.0	85.0	4.09E-03	2.54E-08	3.48E+14	44.0	4.40	4.41	3.50	1.40	150	4.30E-06	4.12E-03
39.0	85.0	3.26E-03	2.03E-08	2.78E+14	44.0	4.41	4.42	3.50	1.40	150	4.30E-06	4.12E-03
40.0	85.0	2.60E-03	1.62E-08	2.22E+14	44.0	4.41	4.42	3.50	1.40	150	4.30E-06	4.12E-03
41.0	85.0	2.07E-03	1.29E-08	1.77E+14	44.0	4.41	4.42	3.50	1.40	150	4.30E-06	4.12E-03
42.0	85.0	1.65E-03	1.03E-08	1.41E+14	44.0	4.41	4.43	3.50	1.40	150	4.30E-06	4.12E-03
43.0	85.0	1.32E-03	8.21E-09	1.12E+14	44.0	4.42	4.43	3.50	1.40	150	4.30E-06	4.12E-03
44.0	85.0	1.05E-03	6.55E-09	8.97E+13	44.0	4.42	4.43	3.50	1.40	150	4.30E-06	4.12E-03
45.0	85.0	8.40E-04	5.23E-09	7.16E+13	44.0	4.42	4.43	3.50	1.40	150	4.30E-06	4.12E-03
46.0	85.0	6.70E-04	4.17E-09	5.71E+13	44.0	4.42	4.44	3.50	1.40	150	4.30E-06	4.12E-03
47.0	85.0	5.35E-04	3.33E-09	4.56E+13	44.0	4.43	4.44	3.50	1.40	150	4.30E-06	4.12E-03
48.0	85.0	4.27E-04	2.66E-09	3.64E+13	44.0	4.43	4.44	3.50	1.40	150	4.30E-06	4.12E-03
49.0	85.0	3.41E-04	2.12E-09	2.91E+13	44.0	4.43	4.44	3.50	1.40	150	4.30E-06	4.12E-03
50.0	85.0	2.72E-04	1.70E-09	2.32E+13	44.0	4.43	4.45	3.50	1.40	150	4.30E-06	4.12E-03
51.0	85.0	2.17E-04	1.35E-09	1.85E+13	44.0	4.44	4.45	3.50	1.40	150	4.30E-06	4.12E-03
52.0	85.0	1.74E-04	1.08E-09	1.48E+13	44.0	4.44	4.45	3.50	1.40	150	4.30E-06	4.12E-03
53.0	85.0	1.39E-04	8.64E-10	1.18E+13	44.0	4.44	4.45	3.50	1.40	150	4.30E-06	4.12E-03
54.0	85.0	1.11E-04	6.90E-10	9.45E+12	44.0	4.44	4.46	3.50	1.40	150	4.30E-06	4.12E-03
55.0	85.0	8.86E-05	5.52E-10	7.55E+12	44.0	4.45	4.46	3.50	1.40	150	4.30E-06	4.12E-03
56.0	85.0	7.08E-05	4.41E-10	6.03E+12	44.0	4.45	4.46	3.50	1.40	150	4.30E-06	4.12E-03
57.0	85.0	5.66E-05	3.52E-10	4.82E+12	44.0	4.45	4.46	3.50	1.40	150	4.30E-06	4.12E-03
58.0	85.0	4.52E-05	2.82E-10	3.86E+12	44.0	4.45	4.47	3.50	1.40	150	4.30E-06	4.12E-03
59.0	85.0	3.62E-05	2.25E-10	3.08E+12	44.0	4.46	4.47	3.50	1.40	150	4.30E-06	4.12E-03
60.0	85.0	2.89E-05	1.80E-10	2.46E+12	44.0	4.46	4.47	3.50	1.40	150	4.30E-06	4.12E-03
61.0	85.0	2.31E-05	1.44E-10	1.97E+12	44.0	4.46	4.47	3.50	1.40	150	4.30E-06	4.12E-03
62.0	85.0	1.85E-05	1.15E-10	1.58E+12	44.0	4.47	4.48	3.50	1.40	150	4.30E-06	4.12E-03
63.0	85.0	1.48E-05	9.21E-11	1.26E+12	44.0	4.47	4.48	3.50	1.40	150	4.30E-06	4.12E-03
64.0	85.0	1.18E-05	7.37E-11	1.01E+12	44.0	4.47	4.48	3.50	1.40	150	4.30E-06	4.12E-03
65.0	85.0	9.46E-06	5.89E-11	8.07E+11	44.0	4.47	4.48	3.50	1.40	150	4.30E-06	4.12E-03
66.0	85.0	7.57E-06	4.72E-11	6.46E+11	44.0	4.48	4.49	3.50	1.40	150	4.30E-06	4.12E-03
67.0	85.0	6.06E-06	3.77E-11	5.17E+11	44.0	4.48	4.49	3.50	1.40	150	4.30E-06	4.12E-03
68.0	85.0	4.85E-06	3.02E-11	4.14E+11	44.0	4.48	4.49	3.50	1.40	150	4.30E-06	4.12E-03
69.0	85.0	3.88E-06	2.42E-11	3.31E+11	44.0	4.48	4.49	3.50	1.40	150	4.30E-06	4.12E-03
70.0	85.0	3.11E-06	1.94E-11	2.65E+11	44.0	4.49	4.50	3.50	1.40	150	4.30E-06	4.12E-03

ALTITUDE, KM	TEMP., DEG K	PRESSURE, MB	MASS DENSITY, GM/CC	NUMBER DENSITY, 1/CC	MOLECULAR MASS, KG/KG-MOLE	DENSITY SCALE HEIGHT, KM	PRESSURE SCALE HEIGHT, KM	SPECIFIC HEAT, C(P)/R	SPECIFIC HEAT RATIO	SOUND SPEED, M/SEC	COEFFICIENT OF VISCOSITY, KG/M SEC	THERMAL CONDUCTIVITY, J/M-SEC DEG K
71.0	85.0	2.49E-06	1.55E-11	2.12E+11	44.0	4.49	4.50	3.50	1.40	150	4.30E-06	4.12E-03
72.0	85.0	1.99E-06	1.24E-11	1.70E+11	44.0	4.49	4.50	3.50	1.40	150	4.30E-06	4.12E-03
73.0	85.0	1.60E-06	9.94E-12	1.36E+11	44.0	4.49	4.51	3.50	1.40	150	4.30E-06	4.12E-03
74.0	85.0	1.28E-06	7.96E-12	1.09E+11	44.0	4.50	4.51	3.50	1.40	150	4.30E-06	4.12E-03
75.0	85.0	1.02E-06	6.38E-12	8.73E+10	44.0	4.50	4.51	3.50	1.40	150	4.30E-06	4.12E-03
76.0	85.0	8.21E-07	5.11E-12	7.00E+10	44.0	4.50	4.51	3.50	1.40	150	4.30E-06	4.12E-03
77.0	85.0	6.58E-07	4.09E-12	5.61E+10	44.0	4.50	4.52	3.50	1.40	150	4.30E-06	4.12E-03
78.0	85.0	5.27E-07	3.28E-12	4.49E+10	44.0	4.51	4.52	3.50	1.40	150	4.30E-06	4.12E-03
79.0	85.0	4.22E-07	2.63E-12	3.60E+10	44.0	4.51	4.52	3.50	1.40	150	4.30E-06	4.12E-03
80.0	85.0	3.39E-07	2.11E-12	2.89E+10	44.0	4.51	4.52	3.50	1.40	150	4.30E-06	4.12E-03
81.0	85.0	2.71E-07	1.69E-12	2.31E+10	44.0	4.51	4.53	3.50	1.40	150	4.30E-06	4.12E-03
82.0	85.0	2.18E-07	1.36E-12	1.86E+10	44.0	4.52	4.53	3.50	1.40	150	4.30E-06	4.12E-03
83.0	85.0	1.75E-07	1.09E-12	1.49E+10	44.0	4.52	4.53	3.50	1.40	150	4.30E-06	4.12E-03
84.0	85.0	1.40E-07	8.72E-13	1.19E+10	44.0	4.52	4.53	3.50	1.40	150	4.30E-06	4.12E-03
85.0	85.0	1.12E-07	6.99E-13	9.57E+09	44.0	4.52	4.54	3.50	1.40	150	4.30E-06	4.12E-03
86.0	85.0	9.01E-08	5.61E-13	7.69E+09	44.0	4.53	4.54	3.50	1.40	150	4.30E-06	4.12E-03
87.0	85.0	7.23E-08	4.50E-13	6.16E+09	44.0	4.53	4.54	3.50	1.40	150	4.30E-06	4.12E-03
88.0	85.0	5.80E-08	3.61E-13	4.94E+09	44.0	4.53	4.54	3.50	1.40	150	4.30E-06	4.12E-03
89.0	85.0	4.65E-08	2.90E-13	3.97E+09	44.0	4.54	4.55	3.50	1.40	150	4.30E-06	4.12E-03
90.0	85.0	3.74E-08	2.33E-13	3.18E+09	44.0	4.52	4.55	3.50	1.40	150	4.30E-06	4.12E-03
91.0	85.0	3.00E-08	1.86E-13	2.56E+09	43.9	4.52	4.56	3.50	1.40	150	4.30E-06	4.14E-03
92.0	85.0	2.41E-08	1.50E-13	2.05E+09	43.9	4.53	4.57	3.50	1.40	150	4.31E-06	4.15E-03
93.0	85.0	1.94E-08	1.20E-13	1.65E+09	43.8	4.53	4.58	3.50	1.40	150	4.31E-06	4.16E-03
94.0	85.0	1.56E-08	9.63E-14	1.33E+09	43.7	4.54	4.59	3.50	1.40	150	4.31E-06	4.17E-03
95.0	85.0	1.25E-08	7.74E-14	1.07E+09	43.7	4.55	4.60	3.50	1.40	151	4.32E-06	4.18E-03
96.0	85.0	1.01E-08	6.22E-14	8.59E+08	43.6	4.56	4.61	3.50	1.40	151	4.32E-06	4.20E-03
97.0	85.0	8.11E-09	5.00E-14	6.91E+08	43.5	4.57	4.62	3.50	1.40	151	4.32E-06	4.21E-03
98.0	85.0	6.53E-09	4.02E-14	5.57E+08	43.5	4.58	4.63	3.50	1.40	151	4.33E-06	4.22E-03
99.0	85.0	5.26E-09	3.23E-14	4.49E+08	43.4	4.59	4.64	3.49	1.40	151	4.33E-06	4.23E-03
100.0	85.0	4.24E-09	2.60E-14	3.62E+08	43.3	4.25	4.65	3.49	1.40	151	4.33E-06	4.25E-03
101.0	87.9	3.44E-09	2.03E-14	2.83E+08	43.2	4.10	4.82	3.49	1.40	154	4.48E-06	4.41E-03
102.0	90.8	2.80E-09	1.60E-14	2.24E+08	43.1	4.25	5.00	3.49	1.40	157	4.63E-06	4.57E-03
103.0	93.7	2.30E-09	1.27E-14	1.78E+08	43.0	4.39	5.17	3.49	1.40	159	4.77E-06	4.73E-03
104.0	96.7	1.90E-09	1.02E-14	1.43E+08	42.9	4.54	5.35	3.49	1.40	162	4.92E-06	4.90E-03
105.0	99.6	1.58E-09	8.18E-15	1.15E+08	42.8	4.69	5.53	3.49	1.40	165	5.07E-06	5.07E-03
106.0	102.5	1.33E-09	6.64E-15	9.37E+07	42.7	4.84	5.71	3.49	1.40	167	5.22E-06	5.24E-03
107.0	105.4	1.12E-09	5.42E-15	7.67E+07	42.6	4.98	5.89	3.49	1.40	170	5.38E-06	5.42E-03
108.0	108.3	9.44E-10	4.45E-15	6.31E+07	42.4	5.13	6.07	3.50	1.40	172	5.53E-06	5.60E-03
109.0	111.2	8.02E-10	3.67E-15	5.23E+07	42.3	5.28	6.26	3.50	1.40	175	5.68E-06	5.78E-03
110.0	114.2	6.86E-10	3.05E-15	4.35E+07	42.2	5.43	6.44	3.50	1.40	177	5.84E-06	5.96E-03

ALTITUDE, KM	TEMP., DEG K	PRESSURE, MB	MASS DENSITY, GM/CC	NUMBER DENSITY, 1/CC	MOLECULAR MASS, KG/KG-MOLE	DENSITY SCALE HEIGHT, KM	PRESSURE SCALE HEIGHT, KM	SPECIFIC HEAT, C(P)/R	SPECIFIC HEAT RATIO	SOUND SPEED, M/SEC	COEFFICIENT OF VISCOSITY, KG/M SEC	THERMAL CONDUCTIVITY, J/M-SEC-DEG K
111.0	117.1	5.88E-10	2.54E-15	3.64E+07	42.1	5.57	6.63	3.50	1.40	180	6.00E-06	6.16E-03
112.0	120.0	5.07E-10	2.13E-15	3.06E+07	42.0	5.72	6.82	3.50	1.40	182	6.16E-06	6.36E-03
113.0	122.9	4.39E-10	1.80E-15	2.59E+07	41.8	5.88	7.01	3.51	1.40	185	6.32E-06	6.56E-03
114.0	125.8	3.81E-10	1.52E-15	2.20E+07	41.7	6.03	7.21	3.51	1.40	187	6.48E-06	6.76E-03
115.0	128.7	3.32E-10	1.29E-15	1.87E+07	41.5	6.19	7.40	3.51	1.40	190	6.64E-06	6.97E-03
116.0	131.7	2.91E-10	1.10E-15	1.60E+07	41.4	6.35	7.60	3.52	1.40	192	6.80E-06	7.18E-03
117.0	134.6	2.56E-10	9.43E-16	1.38E+07	41.3	6.50	7.80	3.52	1.40	195	6.97E-06	7.40E-03
118.0	137.5	2.25E-10	8.10E-16	1.19E+07	41.1	6.66	8.00	3.53	1.40	197	7.13E-06	7.61E-03
119.0	140.4	1.99E-10	6.99E-16	1.03E+07	41.0	6.82	8.20	3.53	1.39	199	7.30E-06	7.84E-03
120.0	143.3	1.76E-10	6.05E-16	8.92E+06	40.9	6.96	8.40	3.54	1.39	202	7.46E-06	8.06E-03
121.0	146.2	1.57E-10	5.25E-16	7.77E+06	40.7	7.11	8.61	3.54	1.39	204	7.63E-06	8.30E-03
122.0	149.2	1.40E-10	4.57E-16	6.79E+06	40.5	7.27	8.83	3.55	1.39	206	7.80E-06	8.54E-03
123.0	152.1	1.25E-10	3.99E-16	5.96E+06	40.4	7.44	9.04	3.55	1.39	209	7.97E-06	8.79E-03
124.0	155.0	1.12E-10	3.50E-16	5.24E+06	40.2	7.60	9.26	3.56	1.39	211	8.14E-06	9.04E-03
125.0	157.9	1.01E-10	3.07E-16	4.62E+06	40.0	7.77	9.48	3.56	1.39	213	8.31E-06	9.29E-03
126.0	160.8	9.08E-11	2.71E-16	4.09E+06	39.9	7.94	9.70	3.57	1.39	216	8.48E-06	9.55E-03
127.0	163.7	8.20E-11	2.39E-16	3.63E+06	39.7	8.11	9.92	3.58	1.39	218	8.65E-06	9.81E-03
128.0	166.7	7.42E-11	2.12E-16	3.23E+06	39.5	8.27	10.15	3.58	1.39	221	8.82E-06	1.01E-02
129.0	169.6	6.73E-11	1.88E-16	2.88E+06	39.4	8.45	10.37	3.59	1.39	223	9.00E-06	1.03E-02
130.0	172.5	6.12E-11	1.67E-16	2.57E+06	39.2	8.59	10.60	3.59	1.39	225	9.17E-06	1.06E-02
131.0	175.4	5.57E-11	1.49E-16	2.30E+06	39.0	8.73	10.84	3.60	1.38	228	9.34E-06	1.09E-02
132.0	178.3	5.09E-11	1.33E-16	2.07E+06	38.8	8.91	11.08	3.60	1.38	230	9.52E-06	1.12E-02
133.0	181.2	4.65E-11	1.19E-16	1.86E+06	38.6	9.09	11.33	3.61	1.38	232	9.70E-06	1.15E-02
134.0	184.2	4.26E-11	1.07E-16	1.68E+06	38.4	9.27	11.58	3.61	1.38	235	9.87E-06	1.18E-02
135.0	187.1	3.91E-11	9.62E-17	1.52E+06	38.2	9.45	11.83	3.62	1.38	237	1.01E-05	1.21E-02
136.0	190.0	3.60E-11	8.67E-17	1.37E+06	38.0	9.63	12.08	3.62	1.38	240	1.02E-05	1.24E-02
137.0	192.9	3.32E-11	7.82E-17	1.25E+06	37.8	9.81	12.34	3.63	1.38	242	1.04E-05	1.27E-02
138.0	195.8	3.06E-11	7.08E-17	1.13E+06	37.6	9.99	12.60	3.63	1.38	244	1.06E-05	1.30E-02
139.0	198.7	2.83E-11	6.41E-17	1.03E+06	37.4	10.18	12.86	3.63	1.38	247	1.08E-05	1.33E-02
140.0	201.7	2.62E-11	5.82E-17	9.42E+05	37.2	10.31	13.13	3.64	1.38	249	1.09E-05	1.36E-02
141.0	204.6	2.43E-11	5.29E-17	8.61E+05	37.0	10.45	13.41	3.64	1.38	252	1.11E-05	1.40E-02
142.0	207.5	2.26E-11	4.81E-17	7.88E+05	36.8	10.64	13.69	3.64	1.38	254	1.13E-05	1.43E-02
143.0	210.4	2.10E-11	4.39E-17	7.23E+05	36.5	10.83	13.98	3.64	1.38	257	1.15E-05	1.47E-02
144.0	213.3	1.96E-11	4.00E-17	6.65E+05	36.3	11.02	14.28	3.64	1.38	260	1.17E-05	1.50E-02
145.0	216.2	1.83E-11	3.66E-17	6.12E+05	36.1	11.22	14.57	3.64	1.38	262	1.19E-05	1.54E-02
146.0	219.2	1.71E-11	3.35E-17	5.64E+05	35.8	11.41	14.88	3.65	1.38	265	1.21E-05	1.57E-02
147.0	222.1	1.60E-11	3.08E-17	5.21E+05	35.6	11.61	15.18	3.65	1.38	267	1.22E-05	1.61E-02
148.0	225.0	1.50E-11	2.83E-17	4.82E+05	35.4	11.81	15.49	3.64	1.38	270	1.24E-05	1.65E-02
149.0	227.9	1.40E-11	2.60E-17	4.46E+05	35.1	12.01	15.80	3.64	1.38	273	1.26E-05	1.68E-02
150.0	230.8	1.32E-11	2.40E-17	4.14E+05	34.9	12.16	16.12	3.64	1.38	275	1.28E-05	1.72E-02

ALTITUDE, KM	TEMP., DEG K	PRESSURE, MB	MASS DENSITY, GM/CC	NUMBER DENSITY, 1/CC	MOLECULAR MASS, KG/KG-MOLE	DENSITY SCALE HEIGHT, KM	PRESSURE SCALE HEIGHT, KM	SPECIFIC HEAT, C(P)/R	SPECIFIC HEAT RATIO	SOUND SPEED, M/SEC	COEFFICIENT OF VISCOSITY, KG/M SEC	THERMAL CONDUCTIVITY, J/M-SEC-DEG K
151.0	233.7	1.24E-11	2.21E-17	3.84E+05	34.6	12.32	16.46	3.64	1.38	278	1.30E-05	1.76E-02
152.0	236.7	1.17E-11	2.04E-17	3.57E+05	34.4	12.53	16.80	3.64	1.38	281	1.32E-05	1.80E-02
153.0	239.6	1.10E-11	1.88E-17	3.33E+05	34.1	12.73	17.14	3.64	1.38	284	1.34E-05	1.84E-02
154.0	242.5	1.04E-11	1.74E-17	3.10E+05	33.9	12.94	17.49	3.63	1.38	287	1.36E-05	1.88E-02
155.0	245.4	9.81E-12	1.62E-17	2.90E+05	33.6	13.14	17.84	3.63	1.38	289	1.38E-05	1.92E-02
156.0	248.3	9.28E-12	1.50E-17	2.71E+05	33.4	13.35	18.20	3.62	1.38	292	1.40E-05	1.96E-02
157.0	251.2	8.79E-12	1.39E-17	2.54E+05	33.1	13.56	18.57	3.62	1.38	295	1.41E-05	2.00E-02
158.0	254.2	8.33E-12	1.30E-17	2.38E+05	32.9	13.78	18.94	3.61	1.38	298	1.43E-05	2.04E-02
159.0	257.1	7.91E-12	1.21E-17	2.23E+05	32.6	13.99	19.32	3.61	1.38	301	1.45E-05	2.08E-02
160.0	260.0	7.51E-12	1.12E-17	2.09E+05	32.3	15.30	19.70	3.60	1.38	304	1.47E-05	2.12E-02
161.0	260.0	7.14E-12	1.06E-17	1.99E+05	32.0	16.67	19.89	3.59	1.39	306	1.48E-05	2.14E-02
162.0	260.0	6.80E-12	9.98E-18	1.89E+05	31.8	16.79	20.09	3.57	1.39	307	1.48E-05	2.16E-02
163.0	260.0	6.47E-12	9.41E-18	1.80E+05	31.5	16.90	20.29	3.55	1.39	309	1.49E-05	2.18E-02
164.0	260.0	6.16E-12	8.88E-18	1.72E+05	31.2	17.02	20.49	3.54	1.39	311	1.49E-05	2.20E-02
165.0	260.0	5.87E-12	8.38E-18	1.63E+05	30.9	17.13	20.70	3.52	1.40	313	1.50E-05	2.22E-02
166.0	260.0	5.59E-12	7.91E-18	1.56E+05	30.6	17.25	20.91	3.51	1.40	314	1.50E-05	2.24E-02
167.0	260.0	5.33E-12	7.47E-18	1.49E+05	30.3	17.37	21.12	3.49	1.40	316	1.51E-05	2.27E-02
168.0	260.0	5.09E-12	7.06E-18	1.42E+05	30.0	17.48	21.34	3.47	1.40	318	1.52E-05	2.29E-02
169.0	260.0	4.85E-12	6.67E-18	1.35E+05	29.7	17.60	21.56	3.46	1.41	320	1.52E-05	2.31E-02
170.0	260.0	4.63E-12	6.31E-18	1.29E+05	29.4	17.64	21.79	3.44	1.41	322	1.53E-05	2.33E-02
171.0	260.0	4.43E-12	5.96E-18	1.23E+05	29.1	17.67	22.03	3.42	1.41	324	1.53E-05	2.35E-02
172.0	260.0	4.23E-12	5.64E-18	1.18E+05	28.8	17.80	22.28	3.40	1.42	326	1.54E-05	2.38E-02
173.0	260.0	4.05E-12	5.33E-18	1.13E+05	28.5	17.92	22.53	3.39	1.42	328	1.55E-05	2.40E-02
174.0	260.0	3.87E-12	5.05E-18	1.08E+05	28.2	18.05	22.79	3.37	1.42	330	1.55E-05	2.43E-02
175.0	260.0	3.71E-12	4.78E-18	1.03E+05	27.9	18.17	23.06	3.35	1.43	333	1.56E-05	2.45E-02
176.0	260.0	3.55E-12	4.53E-18	9.90E+04	27.6	18.30	23.33	3.33	1.43	335	1.56E-05	2.48E-02
177.0	260.0	3.40E-12	4.29E-18	9.49E+04	27.2	18.43	23.61	3.32	1.43	337	1.57E-05	2.50E-02
178.0	260.0	3.26E-12	4.07E-18	9.09E+04	26.9	18.56	23.89	3.30	1.43	339	1.58E-05	2.53E-02
179.0	260.0	3.13E-12	3.86E-18	8.72E+04	26.6	18.68	24.19	3.28	1.44	342	1.59E-05	2.55E-02
180.0	260.0	3.00E-12	3.66E-18	8.37E+04	26.3	18.73	24.48	3.26	1.44	344	1.59E-05	2.58E-02
181.0	260.0	2.88E-12	3.47E-18	8.04E+04	26.0	18.78	24.80	3.25	1.45	347	1.60E-05	2.61E-02
182.0	260.0	2.77E-12	3.29E-18	7.72E+04	25.7	18.92	25.12	3.23	1.45	349	1.61E-05	2.63E-02
183.0	260.0	2.66E-12	3.12E-18	7.42E+04	25.4	19.05	25.46	3.21	1.45	352	1.61E-05	2.66E-02
184.0	260.0	2.56E-12	2.97E-18	7.14E+04	25.0	19.18	25.80	3.19	1.46	355	1.62E-05	2.69E-02
185.0	260.0	2.47E-12	2.82E-18	6.87E+04	24.7	19.31	26.15	3.17	1.46	357	1.63E-05	2.72E-02
186.0	260.0	2.37E-12	2.68E-18	6.61E+04	24.4	19.44	26.51	3.16	1.46	360	1.64E-05	2.75E-02
187.0	260.0	2.29E-12	2.55E-18	6.37E+04	24.1	19.57	26.87	3.14	1.47	363	1.65E-05	2.78E-02
188.0	260.0	2.20E-12	2.42E-18	6.14E+04	23.8	19.70	27.25	3.12	1.47	366	1.65E-05	2.81E-02
189.0	260.0	2.12E-12	2.30E-18	5.92E+04	23.4	19.82	27.64	3.10	1.48	369	1.66E-05	2.84E-02
190.0	260.0	2.05E-12	2.19E-18	5.71E+04	23.1	19.98	28.04	3.08	1.48	372	1.67E-05	2.87E-02

ALTITUDE, KM	TEMP., DEG K	PRESSURE, MB	MASS DENSITY, GM/CC	NUMBER DENSITY, 1/CC	MOLECULAR MASS, KG/KG-MOLE	DENSITY SCALE HEIGHT, KM	PRESSURE SCALE HEIGHT, KM	SPECIFIC HEAT, C(P)/R	SPECIFIC HEAT RATIO	SOUND SPEED, M/SEC	COEFFICIENT OF VISCOSITY, KG/M SEC	THERMAL CONDUCTIVITY, J/M-SEC-DEG K
191.0	260.0	1.98E-12	2.09E-18	5.51E+04	22.8	20.13	28.45	3.06	1.48	375	1.68E-05	2.90E-02
192.0	260.0	1.91E-12	1.99E-18	5.32E+04	22.5	20.26	28.87	3.05	1.49	378	1.69E-05	2.94E-02
193.0	260.0	1.85E-12	1.89E-18	5.14E+04	22.2	20.39	29.30	3.03	1.49	382	1.70E-05	2.97E-02
194.0	260.0	1.78E-12	1.80E-18	4.97E+04	21.8	20.51	29.74	3.01	1.50	385	1.70E-05	3.00E-02
195.0	260.0	1.73E-12	1.72E-18	4.81E+04	21.5	20.64	30.20	2.99	1.50	388	1.71E-05	3.03E-02
196.0	260.0	1.67E-12	1.64E-18	4.65E+04	21.2	20.76	30.67	2.97	1.51	392	1.72E-05	3.07E-02
197.0	260.0	1.62E-12	1.56E-18	4.51E+04	20.9	20.88	31.15	2.96	1.51	396	1.73E-05	3.10E-02
198.0	260.0	1.57E-12	1.49E-18	4.36E+04	20.6	21.00	31.65	2.94	1.52	399	1.74E-05	3.14E-02
199.0	260.0	1.52E-12	1.42E-18	4.23E+04	20.2	21.12	32.17	2.92	1.52	403	1.75E-05	3.17E-02
200.0	260.0	1.47E-12	1.36E-18	4.10E+04	19.9	24.12	32.70	2.90	1.53	407	1.76E-05	3.21E-02
201.0	260.0	1.43E-12	1.31E-18	3.98E+04	19.8	27.86	32.88	2.90	1.53	408	1.76E-05	3.22E-02
202.0	260.0	1.38E-12	1.26E-18	3.86E+04	19.7	27.97	33.06	2.89	1.53	409	1.77E-05	3.23E-02
203.0	260.0	1.34E-12	1.22E-18	3.74E+04	19.6	28.08	33.24	2.88	1.53	410	1.77E-05	3.24E-02
204.0	260.0	1.30E-12	1.18E-18	3.63E+04	19.5	28.19	33.43	2.88	1.53	412	1.77E-05	3.25E-02
205.0	260.0	1.27E-12	1.14E-18	3.53E+04	19.4	28.31	33.61	2.87	1.53	413	1.78E-05	3.26E-02
206.0	260.0	1.23E-12	1.10E-18	3.42E+04	19.3	28.42	33.80	2.87	1.54	414	1.78E-05	3.27E-02
207.0	260.0	1.19E-12	1.06E-18	3.32E+04	19.2	28.53	33.99	2.86	1.54	416	1.78E-05	3.29E-02
208.0	260.0	1.16E-12	1.03E-18	3.23E+04	19.1	28.65	34.18	2.86	1.54	417	1.79E-05	3.30E-02
209.0	260.0	1.13E-12	9.91E-19	3.14E+04	19.0	28.76	34.38	2.85	1.54	418	1.79E-05	3.31E-02
210.0	260.0	1.09E-12	9.58E-19	3.05E+04	19.0	29.51	34.57	2.84	1.54	419	1.79E-05	3.32E-02
211.0	260.0	1.06E-12	9.27E-19	2.96E+04	18.9	30.25	34.72	2.84	1.54	420	1.79E-05	3.33E-02
212.0	260.0	1.03E-12	8.98E-19	2.88E+04	18.8	30.35	34.87	2.84	1.54	421	1.80E-05	3.34E-02
213.0	260.0	1.00E-12	8.69E-19	2.79E+04	18.7	30.45	35.02	2.83	1.55	422	1.80E-05	3.34E-02
214.0	260.0	9.74E-13	8.42E-19	2.72E+04	18.7	30.55	35.17	2.83	1.55	423	1.80E-05	3.35E-02
215.0	260.0	9.47E-13	8.15E-19	2.64E+04	18.6	30.65	35.32	2.82	1.55	424	1.80E-05	3.36E-02
216.0	260.0	9.21E-13	7.89E-19	2.57E+04	18.5	30.76	35.47	2.82	1.55	425	1.81E-05	3.37E-02
217.0	260.0	8.95E-13	7.65E-19	2.50E+04	18.5	30.86	35.63	2.82	1.55	426	1.81E-05	3.38E-02
218.0	260.0	8.71E-13	7.41E-19	2.43E+04	18.4	30.96	35.78	2.81	1.55	427	1.81E-05	3.39E-02
219.0	260.0	8.47E-13	7.18E-19	2.36E+04	18.3	31.06	35.94	2.81	1.55	428	1.81E-05	3.40E-02
220.0	260.0	8.23E-13	6.95E-19	2.29E+04	18.3	31.33	36.10	2.80	1.55	429	1.81E-05	3.40E-02
221.0	260.0	8.01E-13	6.74E-19	2.23E+04	18.2	31.59	36.24	2.80	1.56	430	1.82E-05	3.41E-02
222.0	260.0	7.79E-13	6.53E-19	2.17E+04	18.1	31.69	36.39	2.80	1.56	431	1.82E-05	3.42E-02
223.0	260.0	7.58E-13	6.33E-19	2.11E+04	18.1	31.79	36.54	2.79	1.56	432	1.82E-05	3.43E-02
224.0	260.0	7.38E-13	6.14E-19	2.06E+04	18.0	31.89	36.69	2.79	1.56	433	1.82E-05	3.43E-02
225.0	260.0	7.18E-13	5.96E-19	2.00E+04	17.9	31.99	36.84	2.78	1.56	434	1.83E-05	3.44E-02
226.0	260.0	6.99E-13	5.78E-19	1.95E+04	17.9	32.09	36.99	2.78	1.56	435	1.83E-05	3.45E-02
227.0	260.0	6.80E-13	5.60E-19	1.90E+04	17.8	32.20	37.15	2.78	1.56	436	1.83E-05	3.46E-02
228.0	260.0	6.62E-13	5.43E-19	1.85E+04	17.7	32.30	37.30	2.77	1.56	437	1.83E-05	3.47E-02
229.0	260.0	6.45E-13	5.27E-19	1.80E+04	17.7	32.40	37.46	2.77	1.57	437	1.83E-05	3.47E-02
230.0	260.0	6.28E-13	5.11E-19	1.75E+04	17.6	32.49	37.61	2.77	1.57	438	1.84E-05	3.48E-02

ALTITUDE, KM	TEMP., DEG K	PRESSURE, MB	MASS DENSITY, GM/CC	NUMBER DENSITY, 1/CC	MOLECULAR MASS, KG/KG-MOLE	DENSITY SCALE HEIGHT, KM	PRESSURE SCALE HEIGHT, KM	SPECIFIC HEAT, C(P)/R	SPECIFIC HEAT RATIO	SOUND SPEED, M/SEC	COEFFICIENT OF VISCOSITY, KG/M SEC	THERMAL CONDUCTIVITY, J/M-SEC-DEG K
231.0	260.0	6.11E-13	4.96E-19	1.70E+04	17.6	32.58	37.77	2.76	1.57	439	1.84E-05	3.49E-02
232.0	260.0	5.95E-13	4.82E-19	1.65E+04	17.5	32.69	37.93	2.76	1.57	440	1.84E-05	3.50E-02
233.0	260.0	5.80E-13	4.67E-19	1.62E+04	17.4	32.79	38.09	2.75	1.57	441	1.84E-05	3.51E-02
234.0	260.0	5.65E-13	4.54E-19	1.57E+04	17.4	32.90	38.26	2.75	1.57	442	1.85E-05	3.51E-02
235.0	260.0	5.50E-13	4.40E-19	1.53E+04	17.3	33.00	38.42	2.75	1.57	443	1.85E-05	3.52E-02
236.0	260.0	5.36E-13	4.27E-19	1.49E+04	17.2	33.11	38.58	2.74	1.57	444	1.85E-05	3.53E-02
237.0	260.0	5.23E-13	4.15E-19	1.46E+04	17.2	33.22	38.75	2.74	1.58	445	1.85E-05	3.54E-02
238.0	260.0	5.09E-13	4.03E-19	1.42E+04	17.1	33.32	38.92	2.73	1.58	446	1.85E-05	3.55E-02
239.0	260.0	4.96E-13	3.91E-19	1.38E+04	17.0	33.43	39.09	2.73	1.58	447	1.86E-05	3.56E-02
240.0	260.0	4.84E-13	3.80E-19	1.35E+04	17.0	33.69	39.26	2.73	1.58	448	1.86E-05	3.56E-02
241.0	260.0	4.72E-13	3.69E-19	1.31E+04	16.9	33.95	39.42	2.72	1.58	449	1.86E-05	3.57E-02
242.0	260.0	4.60E-13	3.59E-19	1.28E+04	16.9	34.05	39.58	2.72	1.58	450	1.86E-05	3.58E-02
243.0	260.0	4.48E-13	3.48E-19	1.25E+04	16.8	34.16	39.74	2.72	1.58	451	1.87E-05	3.59E-02
244.0	260.0	4.37E-13	3.38E-19	1.22E+04	16.7	34.27	39.90	2.71	1.58	452	1.87E-05	3.59E-02
245.0	260.0	4.27E-13	3.29E-19	1.19E+04	16.7	34.37	40.07	2.71	1.59	453	1.87E-05	3.60E-02
246.0	260.0	4.16E-13	3.20E-19	1.16E+04	16.6	34.48	40.24	2.71	1.59	454	1.87E-05	3.61E-02
247.0	260.0	4.06E-13	3.11E-19	1.13E+04	16.6	34.59	40.40	2.70	1.59	455	1.87E-05	3.62E-02
248.0	260.0	3.96E-13	3.02E-19	1.10E+04	16.5	34.70	40.57	2.70	1.59	456	1.88E-05	3.63E-02
249.0	260.0	3.86E-13	2.94E-19	1.08E+04	16.4	34.80	40.74	2.69	1.59	457	1.88E-05	3.63E-02
250.0	260.0	3.77E-13	2.86E-19	1.05E+04	16.4	35.78	40.91	2.69	1.59	458	1.88E-05	3.64E-02
251.0	260.0	3.68E-13	2.76E-19	1.03E+04	16.3	36.76	41.03	2.69	1.59	459	1.88E-05	3.65E-02
252.0	260.0	3.59E-13	2.71E-19	1.00E+04	16.3	36.84	41.15	2.69	1.59	460	1.88E-05	3.65E-02
253.0	260.0	3.50E-13	2.64E-19	9.77E+03	16.3	36.93	41.26	2.68	1.59	460	1.88E-05	3.66E-02
254.0	260.0	3.42E-13	2.57E-19	9.53E+03	16.2	37.02	41.38	2.68	1.59	461	1.89E-05	3.66E-02
255.0	260.0	3.34E-13	2.50E-19	9.31E+03	16.2	37.10	41.50	2.68	1.60	462	1.89E-05	3.67E-02
256.0	260.0	3.26E-13	2.44E-19	9.08E+03	16.1	37.19	41.62	2.68	1.60	462	1.89E-05	3.67E-02
257.0	260.0	3.18E-13	2.37E-19	8.87E+03	16.1	37.28	41.74	2.67	1.60	463	1.89E-05	3.68E-02
258.0	260.0	3.11E-13	2.31E-19	8.66E+03	16.1	37.37	41.86	2.67	1.60	464	1.89E-05	3.68E-02
259.0	260.0	3.03E-13	2.25E-19	8.45E+03	16.0	37.46	41.98	2.67	1.60	464	1.89E-05	3.69E-02
260.0	260.0	2.96E-13	2.19E-19	8.26E+03	16.0	39.27	42.10	2.67	1.60	465	1.89E-05	3.69E-02
261.0	260.0	2.89E-13	2.14E-19	8.06E+03	16.0	41.17	42.12	2.67	1.60	465	1.89E-05	3.69E-02
262.0	260.0	2.82E-13	2.09E-19	7.87E+03	16.0	41.19	42.14	2.67	1.60	465	1.89E-05	3.69E-02
263.0	260.0	2.76E-13	2.04E-19	7.69E+03	16.0	41.22	42.17	2.67	1.60	465	1.89E-05	3.69E-02
264.0	260.0	2.69E-13	1.99E-19	7.51E+03	16.0	41.24	42.19	2.67	1.60	465	1.89E-05	3.69E-02
265.0	260.0	2.63E-13	1.95E-19	7.33E+03	16.0	41.26	42.21	2.67	1.60	465	1.89E-05	3.69E-02
266.0	260.0	2.57E-13	1.90E-19	7.16E+03	16.0	41.28	42.24	2.67	1.60	465	1.89E-05	3.69E-02
267.0	260.0	2.51E-13	1.86E-19	6.99E+03	16.0	41.30	42.26	2.67	1.60	465	1.89E-05	3.69E-02
268.0	260.0	2.45E-13	1.81E-19	6.83E+03	16.0	41.33	42.28	2.67	1.60	465	1.89E-05	3.69E-02
269.0	260.0	2.39E-13	1.77E-19	6.67E+03	16.0	41.35	42.30	2.67	1.60	465	1.89E-05	3.69E-02
270.0	260.0	2.34E-13	1.73E-19	6.51E+03	16.0	41.37	42.33	2.67	1.60	465	1.89E-05	3.69E-02

ALTITUDE, KM	TEMP., DEG K	PRESSURE, MB	MASS DENSITY, GM/CC	NUMBER DENSITY, 1/CC	MOLECULAR MASS, KG/KG-MOLE	DENSITY SCALE HEIGHT, KM	PRESSURE SCALE HEIGHT, KM	SPECIFIC HEAT, C(P)/R	SPECIFIC HEAT RATIO	SOUND SPEED, M/SEC	COEFFICIENT OF VISCOSITY, KG/M SEC	THERMAL CONDUCTIVITY, J/M-SEC-DEG K
271.0	260.0	2.28E-13	1.69E-19	6.36E+03	16.0	41.39	42.35	2.67	1.60	465	1.89E-05	3.69E-02
272.0	260.0	2.23E-13	1.65E-19	6.21E+03	16.0	41.42	42.37	2.67	1.60	465	1.89E-05	3.69E-02
273.0	260.0	2.18E-13	1.61E-19	6.07E+03	16.0	41.44	42.40	2.67	1.60	465	1.89E-05	3.69E-02
274.0	260.0	2.13E-13	1.57E-19	5.93E+03	16.0	41.46	42.42	2.67	1.60	465	1.89E-05	3.69E-02
275.0	260.0	2.08E-13	1.54E-19	5.79E+03	16.0	41.48	42.44	2.67	1.60	465	1.89E-05	3.69E-02
276.0	260.0	2.03E-13	1.50E-19	5.66E+03	16.0	41.51	42.47	2.67	1.60	465	1.89E-05	3.69E-02
277.0	260.0	1.98E-13	1.47E-19	5.52E+03	16.0	41.53	42.49	2.67	1.60	465	1.89E-05	3.69E-02
278.0	260.0	1.94E-13	1.43E-19	5.40E+03	16.0	41.55	42.51	2.67	1.60	465	1.89E-05	3.69E-02
279.0	260.0	1.89E-13	1.40E-19	5.27E+03	16.0	41.57	42.54	2.67	1.60	465	1.89E-05	3.69E-02
280.0	260.0	1.85E-13	1.37E-19	5.15E+03	16.0	41.60	42.56	2.67	1.60	465	1.89E-05	3.69E-02
281.0	260.0	1.80E-13	1.34E-19	5.03E+03	16.0	41.62	42.58	2.67	1.60	465	1.89E-05	3.69E-02
282.0	260.0	1.76E-13	1.30E-19	4.91E+03	16.0	41.64	42.61	2.67	1.60	465	1.89E-05	3.69E-02
283.0	260.0	1.72E-13	1.27E-19	4.80E+03	16.0	41.66	42.63	2.67	1.60	465	1.89E-05	3.69E-02
284.0	260.0	1.68E-13	1.24E-19	4.69E+03	16.0	41.68	42.65	2.67	1.60	465	1.89E-05	3.69E-02
285.0	260.0	1.64E-13	1.22E-19	4.58E+03	16.0	41.71	42.68	2.67	1.60	465	1.89E-05	3.69E-02
286.0	260.0	1.60E-13	1.19E-19	4.47E+03	16.0	41.73	42.70	2.67	1.60	465	1.89E-05	3.69E-02
287.0	260.0	1.57E-13	1.16E-19	4.37E+03	16.0	41.75	42.72	2.67	1.60	465	1.89E-05	3.69E-02
288.0	260.0	1.53E-13	1.13E-19	4.27E+03	16.0	41.77	42.74	2.67	1.60	465	1.89E-05	3.69E-02
289.0	260.0	1.50E-13	1.11E-19	4.17E+03	16.0	41.80	42.77	2.67	1.60	465	1.89E-05	3.69E-02
290.0	260.0	1.46E-13	1.08E-19	4.07E+03	16.0	41.82	42.79	2.67	1.60	465	1.89E-05	3.69E-02
291.0	260.0	1.43E-13	1.06E-19	3.98E+03	16.0	41.84	42.81	2.67	1.60	465	1.89E-05	3.69E-02
292.0	260.0	1.39E-13	1.03E-19	3.89E+03	16.0	41.86	42.84	2.67	1.60	465	1.89E-05	3.69E-02
293.0	260.0	1.36E-13	1.01E-19	3.80E+03	16.0	41.89	42.86	2.67	1.60	465	1.89E-05	3.69E-02
294.0	260.0	1.33E-13	9.85E-20	3.71E+03	16.0	41.91	42.88	2.67	1.60	465	1.89E-05	3.69E-02
295.0	260.0	1.30E-13	9.62E-20	3.62E+03	16.0	41.93	42.91	2.67	1.60	465	1.89E-05	3.69E-02
296.0	260.0	1.27E-13	9.40E-20	3.54E+03	16.0	41.95	42.93	2.67	1.60	465	1.89E-05	3.69E-02
297.0	260.0	1.24E-13	9.19E-20	3.46E+03	16.0	41.98	42.95	2.67	1.60	465	1.89E-05	3.69E-02
298.0	260.0	1.21E-13	8.97E-20	3.38E+03	16.0	42.00	42.98	2.67	1.60	465	1.89E-05	3.69E-02
299.0	260.0	1.18E-13	8.77E-20	3.30E+03	16.0	42.02	43.00	2.67	1.60	465	1.89E-05	3.69E-02
300.0	260.0	1.16E-13	8.57E-20	3.23E+03	16.0	42.04	43.02	2.67	1.60	465	1.89E-05	3.69E-02

APPENDIX B

DEVELOPMENT OF ISOTENSOID AND MERIT FUNCTION RELATIONSHIPS

Determination of Isotensoid Shape - Of the two major categories of inflatable drag devices, parachutes and Ballutes, the AID is a type of tucked-back Ballute. The profile of the rear surface of the AID does not intersect the axis of rotational symmetry, but is terminated at specified radial and longitudinal boundaries. Similarly, the forward profile may be terminated at desired attachment locations on the payload. Reference 7 presents the original derivation of the basic isotensoid equations that define the aerodynamic shapes of Ballutes. Typical AID profile curves are shown in Figures 49 and 50. By joining rear profile curves from Figure 49 to the corresponding forward profile curves that are similar to those of Figure 50 (with the juncture at the equator, that is, $X/R' = 1$), a complete AID profile can be obtained. This task has been accomplished, and the results are shown in Reference 9, Figure 4.

The shapes in Reference 9 were calculated by a computer program based on the shape equations of Reference 7. The computer program provides an expedient means of iterating between the aerodynamic loading and isotensoid shape. The program utilizes a theoretical aerodynamic pressure distribution to calculate an initial isotensoid shape. The initial shape can then be used to refine (either by theory or experiment) the initial pressure distribution for use in an iteration to a second isotensoid shape. The iteration process is repeated until satisfactory correlation is obtained.

The term isotensoid was coined by Schuerch (Reference 25), and U.S. Patent 3,121,451 concerning isotensoid structure has been issued to him.

Isotenoid construction is readily applied to pressure vessels wherein the principal membrane stresses are given by the well-known equilibrium membrane equation (Reference 26). Isotensoid construction as usually applied to internal pressure vessels implies a filament wound structure in which a continuous filament is everywhere loaded by internal pressure to an identical stress level. The construction is possible because according to Reference 27, the principle membrane stresses, N_{ϕ} and N_{θ}, which are at right angles to each other at any point always can be replaced by two equal stresses, f, not at right angles as shown in Figure 51.

The required bias angle, β, for equilibrium can be derived from Figure 51 as follows:

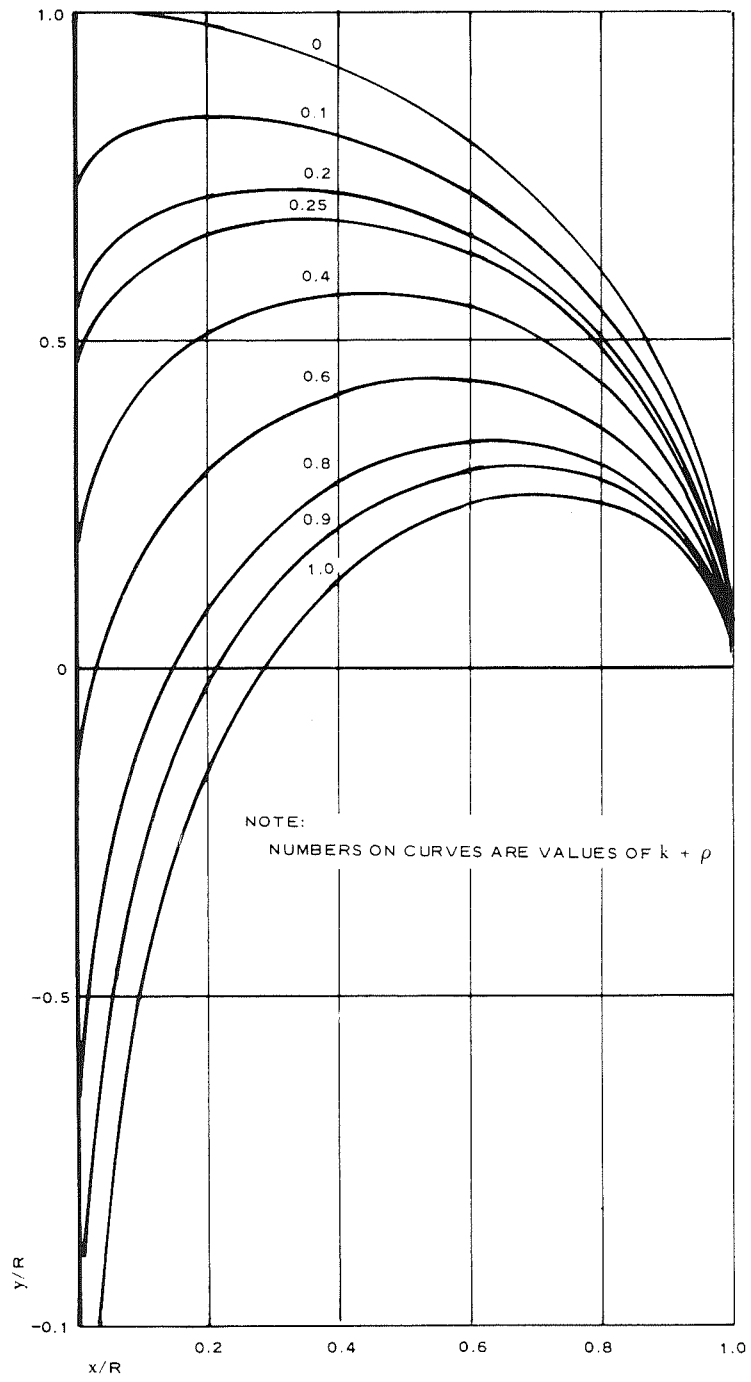

Figure 49 - Profile Curves for $\rho/k = 1$ and Various Values of $k + \rho$ (Rear Profile)

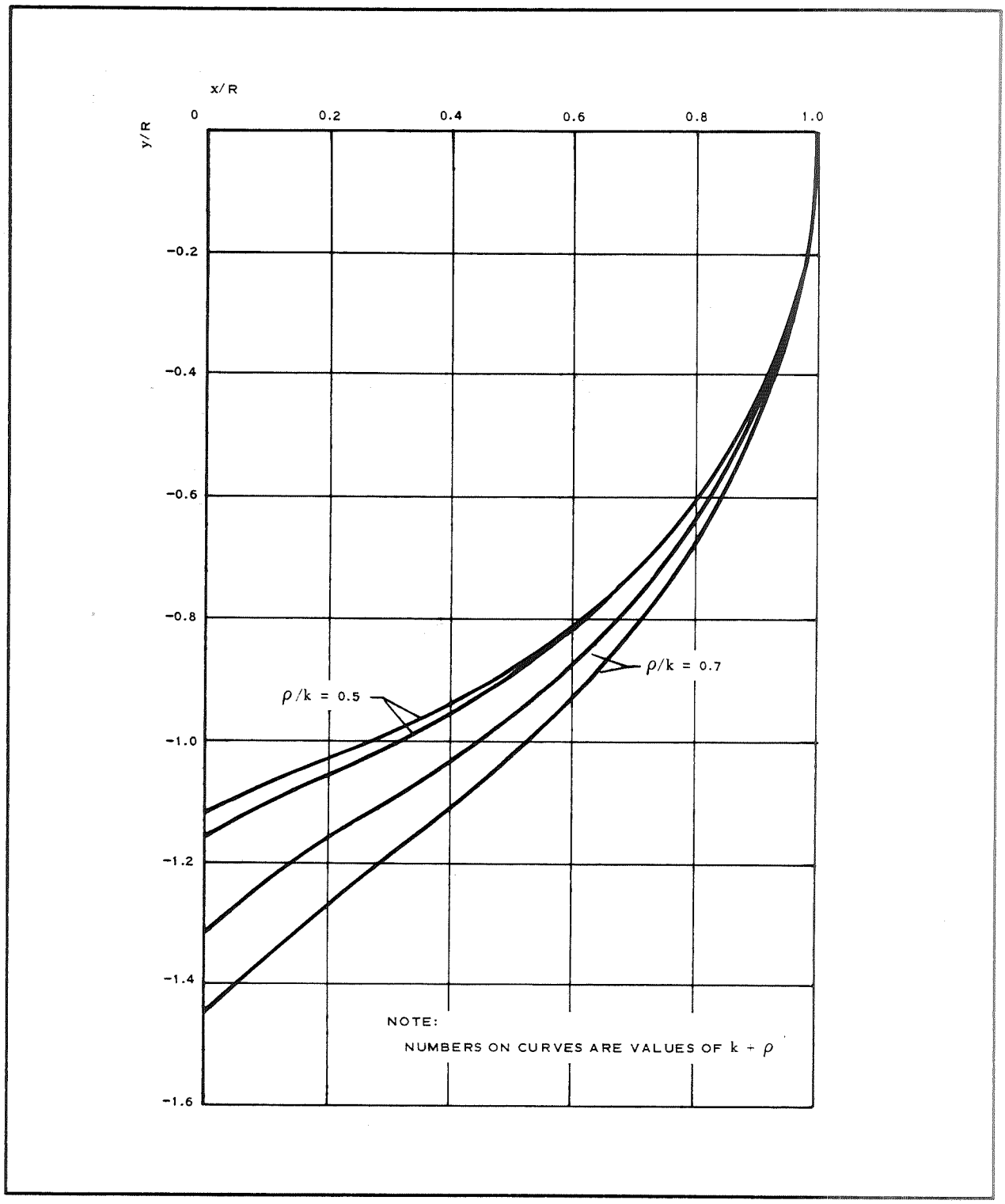

Figure 50 - Profile Curves for $\rho/k = 0.5$ and $\rho/k = -0.7$ and Various Values of $k + \rho$ (Forward Profile)

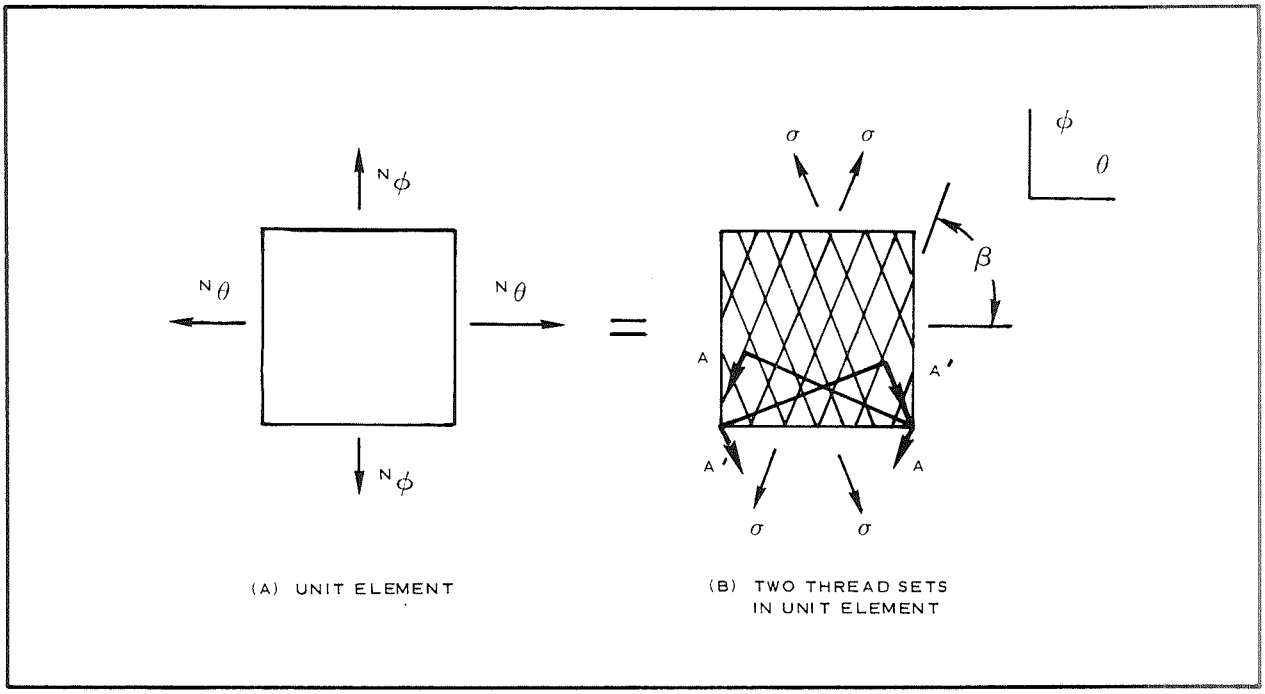

Figure 51 - Orthogonal Stresses N_ϕ and N_θ Equivalent to Nonorthogonal Sets, σ, at Angle β

By summing forces in the principal ϕ direction, the stress, f, in one thread set acts on the cut length AA of Figure A-3, which is simply sin β, Since the other thread set is identical and acts on the length A'A' that is also sin β, equilibrium in the ϕ direction is simply,

$$2f\sin^2\beta = N_\phi. \tag{34}$$

Similarly, by summing forces in the principal θ direction,

$$2f\cos^2\beta = N_\theta. \tag{35}$$

Then by dividing Equation 34 by Equation 35, the result is

$$\tan^2\beta = \frac{N_\phi}{N_\theta} \text{ (see Reference 27).} \tag{36}$$

Schuerch (Reference 25) and others (Reference 28 and 29) have shown that there are pressure vessels with a geometry of the structural surfaces that may be formed by winding a single filament in such a way that Equation 36 is satisfied at each point on the surface. For example, three shapes that can be constructed ideally by filament winding are the cylinder, the geodesic ovalid, and a toroid that is not circular in cross section.

The AID described in this report is a pressure vessel and a toroid of noncicular cross section. However, the basic equations (Reference 7) for determination of its shape involve two variations on the above discussed filament winding concept.

Unlike a pressure vessel that is subjected to a uniform internal pressure, the aerodynamic external pressure distribution acting on the forward decelerator surface varies along the meridian. Hence, the gage pressure (that is, the constant internal pressure minus the variable external pressure) is a function of geometry and must be treated as such during the integration of the membrane equilibrium equations.

Although the addition of a burble fence (see Reference 9) was not originally considered in Reference 7, it has since been incorporated for subsonic stability as previously noted. The aerodynamic drag load on the burble fence is considered as a tangential, concentrated line load acting at the maximum decelerator diameter.

The underlying concept that allows the decelerator to be fabricated of a woven cloth rather than being filament wound with a varying warp angle and still satisfy Equation 36 is the addition of an overlying layer of closely spaced cords oriented parallel to the principal meridian stress direction. By considering these cords as a third set of threads oriented at 45 degrees with the two thread sets of the woven cloth, a variable principal stress ratio can be considered by taking a 1:1 ratio in the woven cloth layer to satisfy Equation 35 and then allowing the remaining part of the meridional principal stress to be carried by the meridian cords. This is illustrated by static equilibrium of the three-thread set element shown in Figure 52.

Applying Equation 35 to Figure 52b gives,

$$f = N_\theta \tag{37}$$

Let f_s denote the stress in the meridional thread set. Then, with reference to Figure 52c,

$$f_s = N_\phi - N_\theta \tag{38}$$

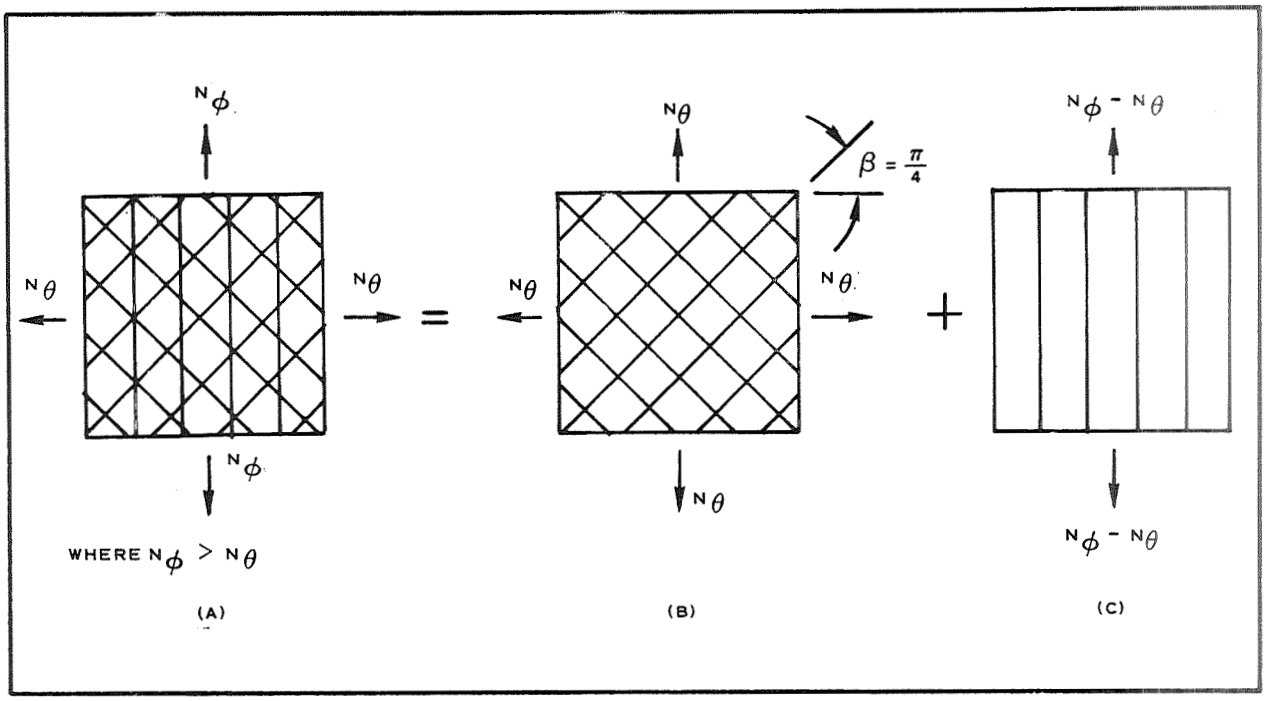

Figure 52- Forces on Three-Thread Set Element

Adding Equation 37 and 38 gives

$$N_{\phi} = f + f_s \ . \tag{39}$$

To actually achieve the above imposed stress relations between the bias threads and the meridian threads, the deformations of each of these two elements must be equal. First, consider the growth in the bias unit element in Figure 52. Since by Equation 37, $f = N_\theta$, and strains, E, are also equal in all directions, then

$$E = E_{\phi} = E_{\theta} \ . \tag{40}$$

The meridian unit element of Figure 52 is free to deform in the θ direction, and there is no problem in matching the E_θ of the bias element. However, the E_ϕ of this element must be equal to that of the bias element. In other words, as seen from Equation 40, the unit elongation of a meridian thread must be equal to that of a bias thread. During the design of an AID, this necessary condition must be checked when selecting materials for the bias cloth and the meridian cords.

Unlike the uniformly spaced threads in the woven cloth, the meridian thread set appears in the form of cords that vary in spacing with the location on the surface of revolution. To maintain a constant stress level in the meridian cords, the tension in each cord, T_m, must be considered. Let x be the radial location of the element of interest and n be the total number of meridian cords around any great circle cut by a plane normal to the axis of revolution. Then, f_s in Equation 39 may be replaced by,

$$f_s = \frac{n T_m}{2 \pi x} . \tag{41}$$

Finally, the two basic isotensoid stress relationships used for development of decelerator shapes are given by Equations 37, 39, and 41.

$$N_\theta = f , \tag{42}$$

and

$$N_\phi = f + \frac{n T_m}{2 \pi x} \tag{43}$$

The equations for shape determination then are given by simply substituting the above principal stress relations into the well-known membrane equilibrium equations (Reference 26) that then define the required principal radii of curvature at any point and can in turn be integrated to ultimately define the coordinates of the meridional profile. These derivations may be readily followed in References 7 and 9. Both of these derivations nondimensionalize the fabric stress and the cord tension with respect to a reference pressure, p, and the maximum radius of the decelerator surface, R' (see Figure 53). The nondimensional fabric stress and the nondimensional cord tension are defined as:

$$\bar{f} = \frac{2f}{pR} , \tag{44}$$

and

$$\bar{T} = \frac{n T_m}{p \pi R'^2} \tag{45}$$

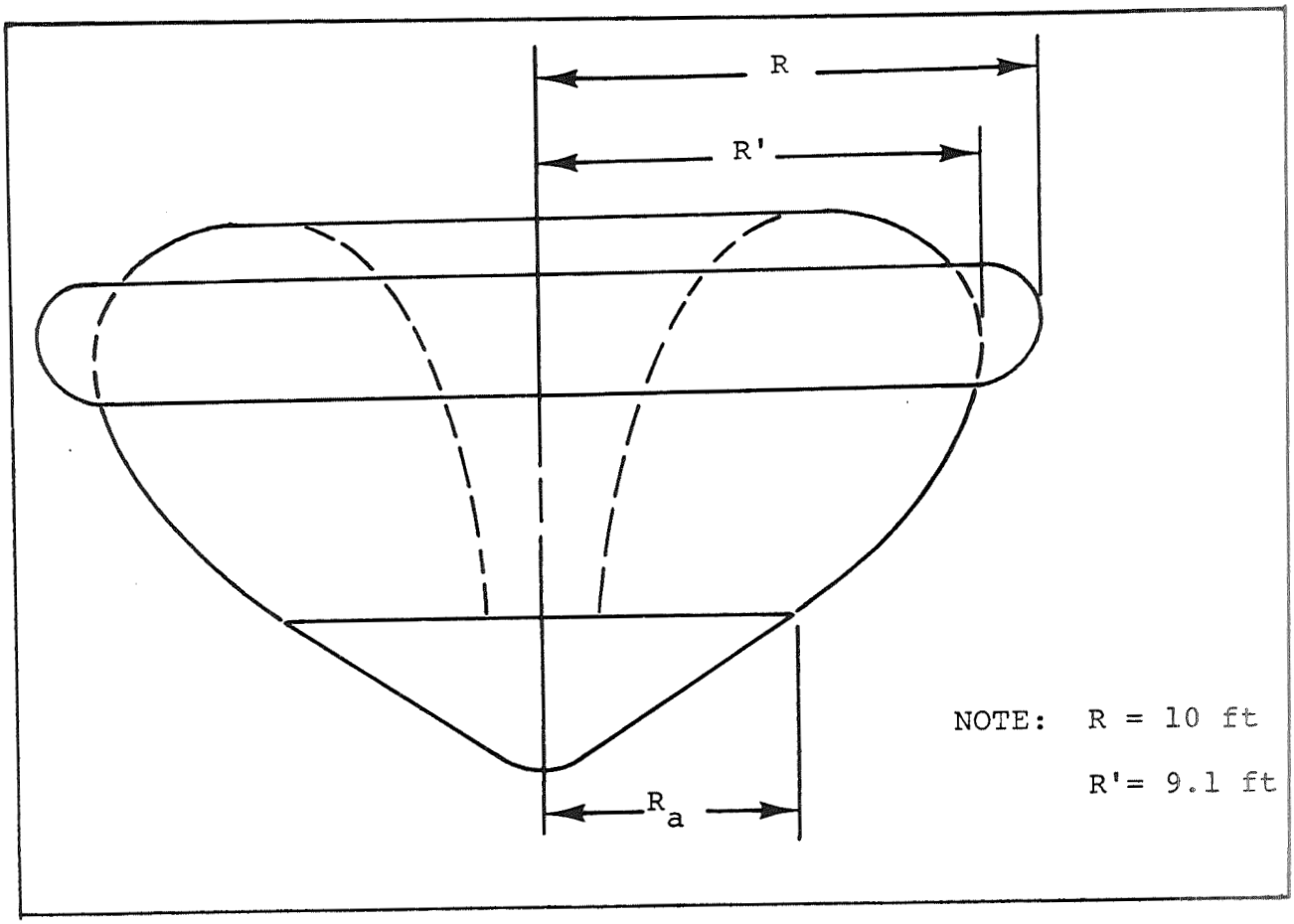

Figure 53 - Cross-Section of AID

The above reference pressure is defined as equal to the internal pressure minus the external aerodynamic pressure over the rear surface of the decelerator that is considered to be uniform; that is,

$$p = p_i - p_b \cdot \tag{46}$$

Derivation of a Merit Function - Various configurations may be considered during the design of an AID. The range of AID profile shapes results from the isotensoid approach wherein arbitrary stress ratios may be imposed and corresponding envelope shapes that are compatible with the aerodynamic loadings then may be determined.

A simple example of the freedom in specifying a stress ratio is seen by applying Equations 42 and 43 to the rear surface of a plainback (dome) Ballute. By substituting the nondimensional quantities of Equations 44 and 45 into 42 and 43, and then dividing, the following relation is obtained:

$$\frac{N_\theta}{N_\phi} = \frac{1}{1 + \left(\frac{\bar{T}}{\bar{f}}\right)\left(\frac{R'}{x}\right)} \tag{47}$$

An infinite number of dome shapes results simply by setting any stress ratio between the limits $0 \leqq N_\theta/N_\phi \leqq 1$. The lower limit yields the well-known Tayler dome (Reference 30) that originally was derived for the shape of parachute canopies. As seen in Equation 47, the fabric stress, $\bar{f}$, for the lower limit must be zero for $N_\theta = 0$ and the meridian cords carry the entire meridional load so that $\bar{T} = 2 \times N_\phi/pR'^2$. Also, since $\bar{T}$ is constant for the isotensoid Taylor dome, equilibrium at the equator ($x = R'$) gives, $N_\phi = pR'/2$ so that, $\bar{T} = 1$. Similarly, the upper limit of $N_\theta/N_\phi = 1$ yields a hemispherical dome where $\bar{T} = 0$ and $\bar{f} = 1$.

The freedom of specifying $\bar{f}$ and $\bar{T}$ between the limits of 0 and 1 leads to the need to have some convenient means of comparing the structural efficiency of various resulting AID shapes. Such a means is provided by considering the structural ballistic coefficient (See Reference 31). Since the primary function of the AID is to provide deceleration, a high aerodynamic drag is desired. The drag capability is commonly referenced to a drag coefficient multiplied by some reference area, i.e., C_DA. The structural ballistic coefficient becomes simply W_S/C_DA, where W_S is the AID structural weight only and is to be minimized with respect to the drag area to obtain an efficient design. Substitution of the equation for the structural weight based on the isotensoid analysis along with the drag coefficient that is compatible with the isotensoid shape gives an expression for the structural ballistic coefficient.

The structural weight of an AID type decelerator, wherein an isotensoid analysis is employed to determine the aerodynamic shape, may be expressed as follows:

$$W_S = d_m n l_m + d_f (A_f + A_b) K_c , \tag{48}$$

where K_c is introduced to account for additional fabric.

The unit weights of the cloth (d_f) and of the meridian cords (d_m) are simply equal to their required ultimate strengths divided by the strength-to-weight ratios of the materials employed. In the event that these unit weights are less than can be obtained due to minimum gage, that is, manufacturing considerations, the latter minimum gage unit weights must be used. This study assumes that only the cloth weight may be dictated by minimum gage with the meridian cord weight being that required for strength considerations. The required unit cloth and meridian cord weights are then, respectively,

$$d_f = \frac{K_D f}{k_f} \quad , \tag{49}$$

and

$$d_m = \frac{K_D T}{k_c} \tag{50}$$

Where K_D is a design factor that converts both the limit cloth stress and the limit meridian cord tension to the required utlimate strengths.

In this study, K_D is actually equivalent to a factor of safety since strength reduction due to elevated temperature will be accounted for in the strength-to-weight ratios of Figure 30. Also, seam efficiency for the cloth is obtained by using the seam curve of Figure 30. Splice efficiency of the meridian cords is taken as 100 percent. Any other strength reductions incurred for a particular application, for example, due to sterilization, calendering of cloth, abrasion, etc., are not considered.

From equation 44,

$$f = \frac{pR'\bar{f}}{2} \tag{51}$$

Letting the parameter $\eta =$ R-R'/2R', the following relation can be obtained:

$$R' = \frac{R}{1 + 2\eta} \quad . \tag{52}$$

Substituting Equation 52 into 51 yields,

$$f = \frac{\bar{f}}{1 + 2\eta} \frac{pR}{2} \tag{53}$$

Substituting Equation 53 into 49 yields:

$$d_f = \frac{K_D}{k_f} \frac{\bar{f}}{(1 + 2\eta)} \frac{pR}{2} \quad . \tag{54}$$

Following a similar procedure to that above, d_m is

$$d_m = \frac{K_D}{k_c} \frac{\bar{T}}{(1 + 2\ )}^2 \frac{p\pi R^2}{\eta} . \qquad (55)$$

The burble fence is considered to introduce a concentrated line load around the equator (at x = R') of the AID that causes higher fabric stresses and meridian cord tensions in the forward surface than in the aft surface. Let the subscripts f and r denote the forward and the aft surfaces, respectively. The nondimensional stress and load parameters then take on two values each. In this study the following relationship is considered:

$$\frac{\bar{f}_f}{\bar{T}_f} = \frac{\bar{f}_r}{\bar{T}_r}$$

(See Reference 9)

where

$$\bar{T}_f > \bar{T}_r \text{ and } \bar{f}_f > \bar{f}_r .$$

The larger of the values for T and f will be used in conjunction with the entire surface area and entire meridian length to simplify the calculation procedure.

The burble fence is constructed of fabric only, the unit weight of which is conservatively assumed to be equal to the unit envelope weight, d_f. Although the cross section of the burble fence is tailored to be a portion of a toroid, its surface area is based upon a complete torus. This shape is considered to be a close approximation. The surface area, A_b, then is

$$A_b = 2\pi \frac{R + R'}{2} \pi (R - R') = \pi^2 (R^2 - R'^2);$$

or, by substituting the parameter, η , gives,

$$A_b = 4 \pi^2 \eta (1 + \eta) R'^2 \qquad (56)$$

The structural weight is given by substituting Equations 55 and 56 into Equation 48,

$$W_s = d_c n l_m + d_f (A_f + A_b) K_c$$

$$= \frac{K_D}{k_c} \frac{\bar{T}}{(1+2\eta)^2} p \pi R^2 l_m + d_f \left[A_f + 4\pi^2 \eta (1+\eta) R'^2 \right] K_c. \quad (57)$$

Referring to Figure 55, the drag on the AID can be expressed as,

$$\begin{aligned} D &= q C_D \left[A - A_a \right] \\ &= q C_D \pi \left[R^2 - R_a^2 \right] \\ &= q C_D \pi \left[1 - \xi^2 \right] R^2 \end{aligned} \quad (58)$$

where $\xi = R_a/R$.

It is of interest to consider the relationship of the AID's drag coefficient as defined above to the aeroshell's drag coefficient C_{D_a}, and the total drag coefficient, C_{D_T}, that is based on the total frontal area, A_T. Then,

$$q C_{D_a} \pi \xi^2 R^2 + D = q C_{D_T} A_T = q C_{D_T} R^2. \quad (59)$$

Substituting Equation 58 into Equation 59 and solving for C_D yields,

$$C_D = \frac{C_{D_T} - \xi^2 C_{D_a}}{1 - \xi^2} \quad (60)$$

Mutliplying the right side of Equation 57 by $\sqrt{C_D A}/\sqrt{C_D A}$ and dividing both sides by Equation 58.

$$\frac{W_s}{q C_D A} = \frac{\sqrt{C_D A}}{\sqrt{C_D \pi (1-\xi^2) R^2}} \frac{1}{q C_D \pi (1-\xi^2) R^2} \left\{ \frac{K_D}{K_c} \frac{\bar{T}}{1+2\eta}^2 p \pi R^2 l_m + \right.$$

$$\left. d_f \left[A_f + 4\pi^2 \eta (1+\eta) R'^2 \right] K_C \right\} \quad (61)$$

Reducing and rearranging Equation 61

$$\frac{W_s}{C_D A} = \frac{K_D}{(C_D \pi)^{1/2} k_c (1-\xi^2)^{3/2}} \left[\frac{p/q}{C_D} \frac{l_m}{R'} \frac{\bar{T}}{(1+2\eta)^2} \right] q \sqrt{C_D A}$$

$$+ \frac{K_C d_f}{C_D (1-\xi^2)} \left[\frac{A_f}{\pi R^2} + 4\pi\eta (1+\eta) \left(\frac{R'}{R} \right)^2 \right] \quad (62)$$

From Equation 52,

$$R = (1 + 2\eta)\, R'$$

Substituting the above relation into Equation 62 gives

$$\frac{W_s}{C_D A} = \frac{K_D}{\left(C_D \pi\right)^{1/2} k_c \left(1-\xi^2\right)^{3/2}} \left[\frac{p/q}{C_D} \quad \frac{1}{R'}\frac{m}{} \quad \frac{\bar{T}}{\left(1+2\eta\right)^3}\right] q \quad \sqrt{C_D A} \tag{63}$$

$$+ \frac{K_C \; d_f}{C_D \left(1-\xi^2\right)\left(1+2\eta\right)^2} \left[\frac{A_f}{\pi R'^2} + 4\pi\eta\left(1+\eta\right)\right]$$

Equation 63 is the same expression presented in Equation 8 of Reference 31 since there is no tow line in the case of the AID; that is, $l_t = 0$ in Equation 8 of Reference 31.

The basic expression for d_f was given in Equation 54. For use in Equation 63, Equation 54 is multiplied and divided by q and the square root of the AID drag area. Also, because of lobing, the actual fabric stress is higher than is reflected in Equation 54. Hence, the factor, β , is introduced. Therefore,

$$d_f = \left[\frac{K_D \beta \bar{f}}{2\left(1 - \xi^2\right)^{1/2}(1 + 2\eta) k_f \sqrt{C_D \pi}} \left(\frac{p}{q}\right) q \sqrt{C_D A}\right]. \tag{64}$$

Evaluation of some merit function parameters - As previously noted, the AID-vehicle profile considered herein is essentially the same as that developed in Reference 14 (with the exception of the forward and aft termination points). Therefore, certain of the quanities needed to evaluate the above merit function have been previously derived and are summarized in Table X, with an appropriate reference noted. The remaining quanities needed to evaluate the merit function are determined below.

Table IX - AID Configurational Properties

$\bar{T}$	=	0.52 (from Reference 14)
$\bar{f}$	=	0.10 (from Reference 14)
l_t	=	0 (there is no towline)
η	=	$\frac{R - R'}{2R'}$ = 0.05 (from geometry of Figure 15 of this report)
ζ	=	$\frac{0.44}{1.1}$ = 0.40 (from geometry of Figure 15 of this report)
$\frac{p}{q}$	=	1.92 (from Reference 2, Figure 16)
C_{D_a}	=	1.5 (from Reference 2, Figure 15)
C_{D_T}	=	1.14 (from Reference 2, Figure 17)

The profile developed in Reference 14 is presented in Figure 54 along with its line section properties that are needed in the following calculations. It should be noted that while the coordinate system used in Reference 14 has been used in Figure 54 for convenience, its use does not affect the resulting values needed in the evaluation of the merit function. Points 1 and 2 of Figure 54 denote the termination points of X/R' = 0.44 and X/R' = 0.15, respectively, for the current profile. The corresponding meridian length and surface area are very closely obtained by simply substituting the proper values based on the curved lengths between the abscissa and these points from the above values.

The forward subtracted meridian length and area are:

$$\frac{l_f}{R'} = \sqrt{(0.44 - 0.385)^2 + \overline{0.025}^2}$$

$$= 0.0604 \ ,$$

and

$$\frac{A_f}{R'^2} = \pi \ (0.44 + 0.385) \ (0.0604)$$

$$= 0.1565 \ .$$

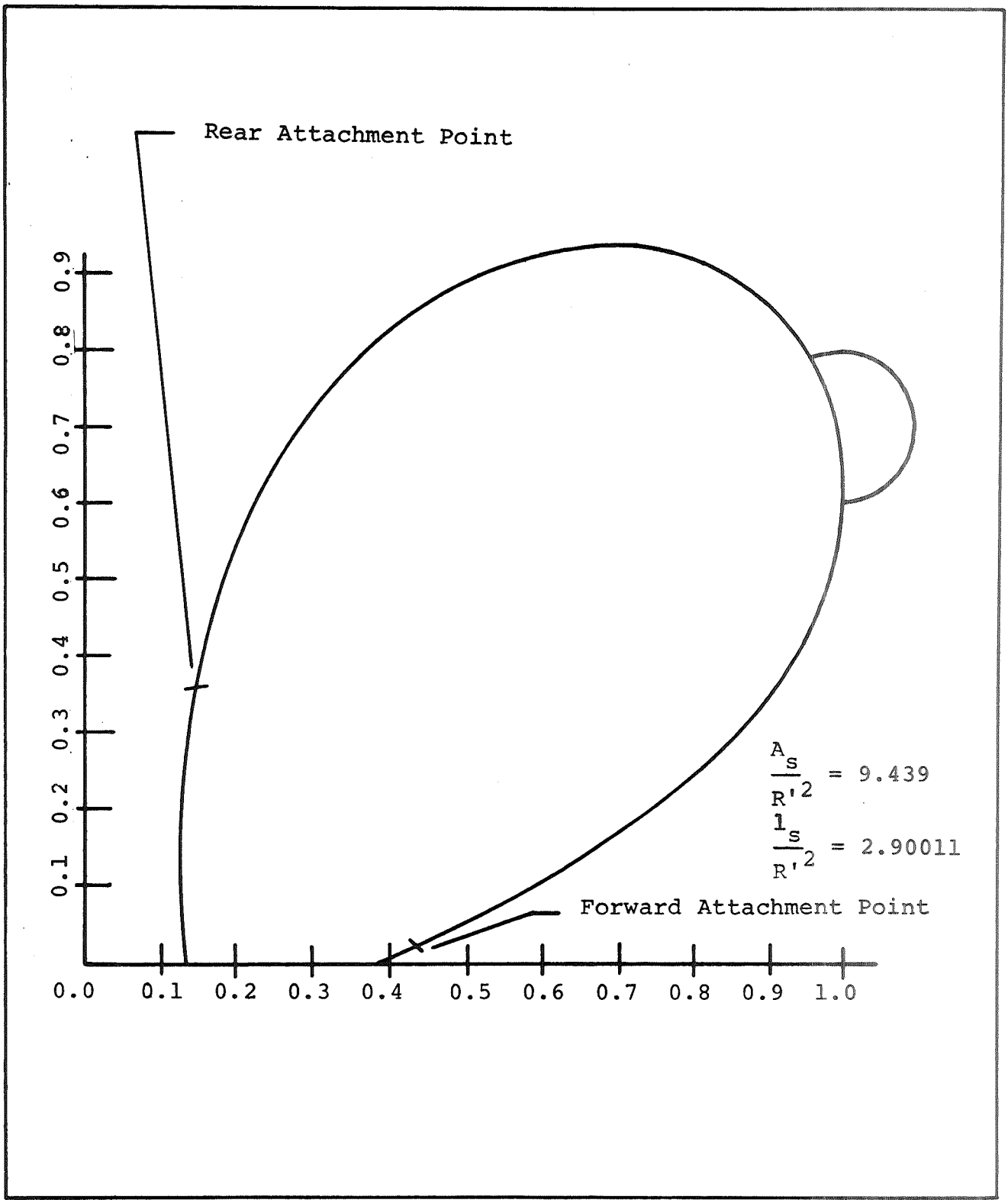

Figure 54 - AID Geometric Section Properties

The aft subtracted length and area are: $l_r/R' = 0.36$, and $A_r/R'^2 = \pi(0.13 + 0.15)(0.36) = 0.1583$. Therefore, the meridian length and surface area of the current profile are: $l_m/R' = 2.90011 - 0.0604 - 0.36 = 2.479$, and $A_f/\pi R'^2 = 1/\pi(9.439 - 0.1565 - 0.1583) = 2.904$,

and

$$\frac{A_f}{\pi R'^2} = \frac{1}{\pi}(9.439 - 0.1565 - 0.1583)$$

$$= 2.904$$

Next consider the parameter β that allows for an increase in fabric stress over the theoretical value of f due to lobing. The maximum stress due to lobing is discussed in detail in Reference 14 where its nondimensional value is equal to 0.1294. Since the same shape applies here, this value may be used and for $\bar{f} = \sqrt{0.10}$,

$$\beta = \frac{0.1294}{0.10} = 1.294$$

Next consider the construction factor, K_c, that accounts for the additional fabric required for lobing and seams along with sewing threads. The additional fabric is determined by comparing the areas of the gore patterns with those of the isotensoid body of revolution. From Reference 14 the following geometric properties are obtained from the five-foot diameter AID wind tunnel models:

$$R = 30 \text{ in.},$$
$$R' = 27.2 \text{ in.},$$
$$\eta = 0.05147;$$

and

$$A_f = 6180 \text{ sq. in.},$$
$$A_b = 4\pi^2\eta(1 + \eta)R'^2$$
$$= 2.136\ R'^2$$
$$= 1580 \text{ sq. in.},$$
$$A_f + A_b = 7760 \text{ sq. in.},$$

This value for the area compares to the actual gore pattern area of;

$$\text{Envelope gores} = 7457 \text{ sq. in.},$$
$$\text{Burble fence gores} = 2027 \text{ sq. in., and}$$
$$\text{Reinforcements} = 874 \text{ sq. in.}$$
$$\Sigma = 10{,}358 \text{ sq. in.}$$

Hence the construction factor becomes,

$$K_c = \frac{10,358}{7,760} = 1.33$$

Assume five percent to account for sewing threads; then

$$K_c = (1.05)\ (1.33) = 1.4 \quad .$$

From Equation 60,

$$C_D = \frac{C_{D_T} - \xi^2 C_{D_a}}{1 - \xi^2}$$

$$= \frac{1.14 - (0.16)(1.5)}{1 - 0.16}$$

$$= 1.07$$

Finally, the total projected area of the AID is.

$$A = \pi (1 - \xi^2) R^2$$

$$= 0.84\ \pi R^2$$

REFERENCES

1. Guy, L. D.: Structural Design Options for Mars Entry. J. Spacecraft Rockets, Vol. 6, No. 1, Jan. 1969, pp 44-49.

2. Bohon, H. L.; and Miserentino, R.: Attached Inflatable Decelerator Performance Evaluation and Mission-Application Study. AIAA Paper No. 70-1163, AIAA Aerodynamic Deceleration Systems Conference (Dayton, Ohio), September 1970.

3. Odom, R. R.: Automated Mars Surface Sample Return Mission/ System Study, Final Report. NASA CR-66587, February 1970.

4. Gillis, C. L.: Aerodynamic Deceleration Systems for Space Missions. AIAA Paper No. 86-1081, AIAA Fifth Annual Meeting (Philadelphia, Pa.), October 1968.

5. Bohon, H. L.; and Miserentino, R.: Deployment and Performance Characteristics of 5-Foot-Diameter (1.5m) Attached Inflatable Decelerators From Mach Number 2.2 to 4.4. NASA TN D-5840, August 1970.

6. Lau, R. A.; and Hussong, J. C.: The Viking Mars Lander Decelerator System. AIAA Paper No. 70-1162, AIAA Aerodynamic Deceleration Systems Conference (Dayton, Ohio), September 1970.

7. Houtz, N.: Optimization of Inflatable Drag Devices by Isotensoid Design. AIAA Paper No. 64-437, First Annual AIAA Meeting (Washington, D.C.), 29 June through 2 July 1964.

8. Reichenau, David E. A.: Investigation of an Attached Inflatable Decelerator System for Drag Augmentation of the Voyager Entry Capsule at Supersonic Speeds. AEDC-TR-68-71, U. S. Air Force, April 1968.

9. Mikulas, M. M., Jr.; and Bohon, H. L.: Development Status of Attached Inflatable Decelerators. J. Spacecraft Rockets, Vol 6, No. 6, June 1969, pp 654-660.

10. Baker, D. C.: Investigation of an Inflatable Decelerator Attached to a 120-Deg Conical Entry Capsule at Mach Numbers from 2.55 to 4.40. AEDC-TR-68-227, U. S. Air Force, October 1968.

11. Baker, D. C.: Investigation of an Attached Inflatable Decelerator with Mechanically Deployed Inlets at Mach Numbers from 2.25 to 4.75. AEDC-TR-69-132, U.S. Air Force, June 1969.

12. Deveikis, W. D.; and Sawyer, J. W.: Static Aerodynamic Characteristics, Pressure Distributions, and Ram-Air Inflation of Attached Inflatable Decelerator Models at Mach 3.0. NASA TN D-5816, May 1970.

13. Baker, D. C.: Performance Evaluation of Attached Inflatable Decelerator with Mechanically Deployed Inlets at M = 2.6 to 4.4 AEDC TR-254, November 1970.

14. Barton, R. R.: Development of Attached Inflatable Decelerators for Supersonic Application. NASA CR-66613, 1968.

15. Usry, J. W.: Performance of a Towed, 48-Inch-Diameter (121.92-Cm) Ballute Decelerator Tested in Free Flight at Mach Numbers from 5.2 to 0.4. NASA TN D-4943.

16. Marco, D. M.; and Mehring, R. D.: Design and Fabrication of Units for Project ALARR. Final Report Air Force Contract AF291(601)-7132).

17. Bloetscher, F.: Aerodynamic Deployable Decelerator Performance - Evaluation Program Phase II Technical Report AFFDL-TR-67-25, Akron, Ohio, Goodyear Aerospace Corporation, April, 1967.

18. Lees, L.: Laminar Heat Transfer Over Blunt Bodies at Hypersonic Flight Speeds. Jet Propulsion, Vol. 26, No. 4, April 1956, pp 259-269.

19. Rose, P. H.; Probstein, R. F.; and Adams, M. C.: Turbulent Heat Transfer Through a Highly Cooled, Partially Dissociated Boundary Layer. J. Aerospace Sci., Vol. 25, No. 12, 1958, pp. 751-760.

20. Deveikis, W. D.; and Sawyer, J. W.: Flow Patterns and Pressure Distribution Around a Bluff Afterbody in the Wake of a 120° Cone for Various Separation Distance at Mach 3.0. NASA TN-D-6281.

21. Stallings, R. L.; and Tudor, D. H.: Experimental Pressure Distribution on a 120° Cone at Mach Numbers from 2.96 to 4.63 and Angles of Attack from 0° to 20°. NASA TN-D5054, 1969.

22. Campbell, J. F.; and Tudor, D. H.: Pressure Distribution on 140°, 160°, and 180° Cones at Mach Numbers from 2.30 to 4.63 and Angles of Attack from 0° to 20°. NASA TN-D5204, 1969.

23. ASD-TDR-62-810: Thermal Transport and Radiative Properties of Fibrous Structural Materials. General American Transportation Corp., November 1962.

24. Nissel, R. E.: Strength to Weight Values for Nomex Cloth and Webbing of Ambient and Elevated Temperatures. ARD-10, 574, Goodyear Aerospace Corporation 24 April 1967.

25. Schuerch, H.: Space Structure Design with Composite Materials. American Rocket Society Paper 1096-60, presented at Structural Design of Space Vehicle Conference, 6-8 April 1960.

26. Timoshenko, S.; and Woinowsky-Krieger, S.: Theory of Plates and Shells 2nd Edition, McGraw-Hill Book Company, Inc., 1959.

27. Haas, R.; and Dietzius, A.: Stretching of the Fabric and Deformation of the Envelope in Non-Rigid Balloons. NACA Report No. 16, 3rd Annual Report, pp. 144-171, 1917 (K. K. Darrow, trans.; originally published by Springer-Verlag, Berlin, 1912).

28. Foerster, A. E.: End Closures of Filament-Wound Motor Cases. GER-10353, Goodyear Aerospace Corporation, 9 June 1961.

29. Marketos, J. D.: Optimum Toroidal Pressure Vessel Filament-Wound Along Geodesic Lines. AIAA Preprint 216-63, presented at Launch and Space Vehicle Shell Structures Conference, 1-3 April 1963.

30. Jones, R.: On the Aerodynamic Characteristics of Parachutes. R & M. No. 862, Aeronautical Research Committee, His Majesty's Stationery Office, June 1923.

31. Anderson, M. S.; Bohon, H. L.; and Mikulas, M. M.: A Structural Merit Function for Aerodynamic Decelerators. NASA TN D-5535, November 1969.